学位論文（要約）

Studies of Electronic Properties of Nanocarbon Materials by Transport Measurement

（ナノカーボン物質系の電子状態の輸送測定による研究）

平成28年12月博士（理学）申請

東京大学大学院理学系研究科
物理学専攻
中山　和貴

Abstract

Nanocarbon is low dimensional allotropes of carbon and each material is interesting from the viewpoint of both fundamental physics and application. Among them, one dimensional (1D) form of carbon: carbon nanotube (CNT) and two dimensional (2D) form of carbon: graphene are of central interest due to the peculiarity of their electronic properties. In this thesis, we have made transport measurements of CNT and graphene paying special attention on differences in monolayer and bilayer systems. More specifically, we have made transport measurements on three dimensional (3D) random networks of CNTs to seek for electronic 1D character of CNT and on exfoliated graphene samples to study effects of O_2 adsorption on the electronic properties.

An 1/3 fraction of as-synthesized CNT is normally of metallic tubes, and Another 2/3 is of semiconducting. So far, mass production of CNTs consisting only of metallic or semiconducting type has been difficult. However, the recent progress in sorting technique of CNTs enables collecting large amount of single electronic type tubes. In this thesis, detailed transport properties of pure metallic CNT networks are experimentally investigated. Networks of metallic single-walled carbon nanotubes (SWCNTs) showed 3D variable range hopping (VRH) behaviors, which is consistent with the previous reports for unsorted samples. On the other hand, networks of metallic double-walled carbon nanotubes (DWCNTs) showed a power-law temperature dependence of resistivity which is consistent with the prediction from the Tomonaga-Luttinger Liquid (TLL) theory for interacting 1D fermion systems. The previous experiments on an individual CNT or CNT rope of 1 μm long or less showed similar power-law behaviors [1, 2, 3]. However, results in this type of experiment generally differ sample to sample due to the lead contact effect, i.e., bulk or end contacted [1], and the mesoscopic effect such as the Coulomb blockade [1]. Results of the present work on the metallic DWCNT network show the power-law dependence with a reproducible and universal power ($= -0.233 \pm 0.009$) which is in very good agreement with the theoretical prediction ($= -0.24$) for bulk-contacted TLL [4, 5, 6, 7]. This shows that DWCNTs have better connectivity at CNT-CNT junctions (or rope-rope junctions) than SWCNTs.

It was recently reported that sulfur atoms introduced inside CNT form stable 1D chain which becomes metallic due to the effective high pressure environment confined in such a nano space [8]. In this thesis, transport properties of purely metallic SWCNT and DWCNT networks with sulfur chains were investigated. In SWCNT, a significant increase of conductivity due to the sulfur chain formation was confirmed, while no change was observed in DWCNT. And neither SWCNT nor DWCNT showed any change in the conduction mechanism such as the VRH or TLL mechanism. This result can be explained as follows. At least some parts of the sulfur chains are indeed metallic, but their lengths are not long enough to improve drastically the junction conductance. In the case of DWCNT, the metallicity

of sulfur chains is masked probably by the insufficient conductivity of the inner wall. It might be expected that the sulfur chains become superconducting at low temperatures as bulk sulfur which becomes superconducting below T = 10-17 K at very high pressures above 90 GPa [9]. Our transport measurements down to 0.27 K, however, showed no sign of superconductivity.

Since conduction characteristics of graphene can be changed largely by gas molecules adsorption [10, 11, 12, 13, 14, 15], possible application to gas sensors have extensively been conducted [16, 17, 18, 19, 20]. As graphene with higher crystallinity is usually obtained by exfoliation in the air, it is important to know the effect of oxygen and nitrogen gas adsorption. So far, it is known that bilayer (BL) graphene can be hole-doped by exposure to oxygen gas [12, 14] and that time evolution of the doping follows the power-law rather than the Langmuirian (exponential) behavior. In monolayer (ML) graphene, a similar hole-doping has also been observed but in a much shorter time scale [21]. In this thesis, we measured time evolutions of the gate voltage ($V_{\rm g}$) vs. resistance data for exfoliated BL and ML graphene samples after O_2 exposure. In this experiment, we constructed a homemade indium microsoldering apparatus, with which we can fabricate four-terminal microelectrodes on an exfoliated graphene sample of 10 μm long without contaminating its surface unlike the conventional lithography method. For BL graphene, our data are in good agreement with the previous report [12]. However, they can be fitted much better to a double-exponential function in time (t) (or single-exponential plus t-linear dependence) rather than the simple power-law claimed by the previous workers [12]. We found that the ML graphene shows nearly the same feature as BL one. However, most importantly, the amount of hole-doping is much less in ML than BL by an order of magnitude. This is possibly because of higher reactivity with oxygen molecules at defect sites especially near the edges in BL than ML. The two-stage behavior of resistance change suggests the existence of multiple processes of chemisorption.

We also examined the effect of oxygen adsorption at lower temperatures down to 1.6 K. Both before and after the oxygen adsorption the graphene samples showed a 2D VRH behavior. The characteristic temperature T_0 in the VRH theory increases by oxygen adsorption, indicating that the hole-doping by the adsorption strengthens electron localization.

Since pristine graphene has no band gap, controlled creation of the band gap is very important for device application. It is theoretically predicted that when atoms or molecules are adsorbed on graphene with periodicity of $(n\sqrt{3} \times n\sqrt{3})R30^\circ$ graphene acquires the gap due to symmetry breaking of the honeycomb lattice [22]. In this work, we tried to confirm this by Kr adsorption. Kr was selected as adsorbent as it is the largest (heaviest) noble gas atom which is capable of forming the $(\sqrt{3} \times \sqrt{3})R30^\circ$ structure on a graphite surface. Exfoliated graphite with a large surface area was used as a buffer to control the areal density of adsorbent precisely. However, a result of Kr adsorption experiment on a suspended graphene sample was unsuccessful to detect measurable change in transport property. This is presumably indicative of a too small effect on the hopping integral of electrons in graphene produced by the Kr physisorption.

[1] M. Bockrath, D. H. Cobden, J. Lu, A. G. Rinzler, R. E. Smalley, L. Balents, and P. L. McEuen, *Luttinger-liquid behaviour in carbon nanotubes*, Nature **397**, 598–601 (1999).

[2] E. Graugnard, P. De Pablo, B. Walsh, A. Ghosh, S. Datta, and R. Reifenberger, *Temperature dependence of the conductance of multiwalled carbon nanotubes*, Physical Review B **64**, 125407 (2001).

[3] J. Park, G. Kim, J. Park, H. Yu, G. McIntosh, V. Krstic, S. Jhang, B. Kim, S. Lee, S. Lee *et al.*, *Quantum transport in low-dimensional organic nanostructures*, Thin Solid Films **393**, 161–167 (2001).

[4] C. Kane, L. Balents, and M. P. Fisher, *Coulomb interactions and mesoscopic effects in carbon nanotubes*, Physical Review Letters **79**, 5086 (1997).

[5] R. Egger and A. O. Gogolin, *Effective low-energy theory for correlated carbon nanotubes*, Physical Review Letters **79**, 5082 (1997).

[6] M. Bockrath, D. H. Cobden, P. L. McEuen, N. G. Chopra, A. Zettl, A. Thess, and R. E. Smalley, *Single-electron transport in ropes of carbon nanotubes*, Science **275**, 1922–1925 (1997).

[7] S. J. Tans, M. H. Devoret, H. Dai, A. Thess, R. E. Smalley, L. Geerligs, and C. Dekker, *Individual single-wall carbon nanotubes as quantum wires*, Nature **386**, 474–477 (1997).

[8] T. Fujimori, A. Morelos-Gómez, Z. Zhu, H. Muramatsu, R. Futamura, K. Urita, M. Terrones, T. Hayashi, M. Endo, S. Young Hong *et al.*, *Conducting linear chains of sulphur inside carbon nanotubes*, Nature Communications **4**, 2162 (2013).

[9] V. V. Struzhkin, R. J. Hemley, H.-k. Mao, and Y. A. Timofeev, *Superconductivity at 10–17 K in compressed sulphur*, Nature **390**, 382–384 (1997).

[10] F. Schedin, A. Geim, S. Morozov, E. Hill, P. Blake, M. Katsnelson, and K. Novoselov, *Detection of individual gas molecules adsorbed on graphene*, Nature Materials **6**, 652–655 (2007).

[11] H. Romero, P. Joshi, A. Gupta, H. Gutierrez, M. Cole, S. Tadigadapa, and P. Eklund, *Adsorption of ammonia on graphene*, Nanotechnology **20**, 245501 (2009).

[12] Y. Sato, K. Takai, and T. Enoki, *Electrically Controlled Adsorption of Oxygen in Bilayer Graphene Devices*, Nano Letters **11**, 3468–3475 (2011).

[13] Y. Yang and R. Murali, *Binding mechanisms of molecular oxygen and moisture to graphene*, Applied Physics Letters **98**, 093116–093116 (2011).

[14] I. Silvestre, E. A. de Morais, A. O. Melo, L. C. Campos, A.-M. B. Goncalves, A. R. Cadore, A. S. Ferlauto, H. Chacham, M. S. Mazzoni, and R. G. Lacerda, *Asymmetric effect of oxygen adsorption on electron and hole mobilities in bilayer graphene: long- and short-range scattering mechanisms*, ACS Nano **7**, 6597–6604 (2013).

[15] J. Sun, M. Muruganathan, and H. Mizuta, *Room temperature detection of individual molecular physisorption using suspended bilayer graphene*, Science Advances **2**, e1501518 (2016).

[16] Y. Dan, Y. Lu, N. Kybert, Z. Luo, and A. Johnson, *Intrinsic response of graphene vapor sensors*, Nano Letters **9**, 1472–1475 (2009).

[17] R. Arsat, M. Breedon, M. Shafiei, P. Spizziri, S. Gilje, R. Kaner, K. Kalantar-zadeh, and W. Wlodarski, *Graphene-like nano-sheets for surface acoustic wave gas sensor applications*, Chemical Physics Letters **467**, 344–347 (2009).

[18] F. Yavari, Z. Chen, A. V. Thomas, W. Ren, H.-M. Cheng, and N. Koratkar, *High Sensitivity Gas Detection Using a Macroscopic Three-Dimensional Graphene Foam Network*, Scientific Reports **1**, 166 (2011).

[19] C. Chen, S. Hung, M. Yang, C. Yeh, C. Wu, G. Chi, F. Ren, and S. Pearton, *Oxygen sensors made by monolayer graphene under room temperature*, Applied Physics Letters **99**, 243502–243502 (2011).

[20] M. Nakamura, Y. Kanai, Y. Ohno, K. Maehashi, K. Inoue, and K. Matsumoto, *Graphene-FET-based gas sensor properties depending on substrate surface conditions*, Japanese Journal of Applied Physics **54**, 06FF11 (2015).

[21] R. Jaaniso, T. Kahro, J. Kozlova, J. Aarik, L. Aarik, H. Alles, A. Floren, A. Gerst, A. Kasikov, A. Niilisk *et al.*, *Temperature induced inversion of oxygen response in CVD graphene on SiO 2*, Sensors and Actuators B: Chemical **190**, 1006–1013 (2014).

[22] M. Farjam and H. Rafii-Tabar, *Energy gap opening in submonolayer lithium on graphene: Local density functional and tight-binding calculations*, Physical Review B **79**, 045417 (2009).

Contents

1. Introduction

1.1. Carbon nanotube

Carbon nanotube (CNT) is a tube of nanometer size diameter made of carbon atoms, and often referred to as one-dimensional isomer of carbon. CNTs are mechanically strong in axial direction [1] and are already applied to fiber material. Extensive researches are ongoing towards applications utilizing mechanical and electronic properties of CNTs. Nowadays, CNT is so common that even people not familiar with science know its name.

Transmission electron microscope (TEM) images of possible CNTs have been reported as early as 1952, as "hollow graphitic carbon fibers" [2]. They were first regarded as an unnecessary by-product of coal and steel industry processing [3]. In 1991, Sumio Iijima synthesized multi-walled CNTs and identified their atomic structure by electron diffraction method [4], which is now recognized as the discovery of CNT. It is noted that in 1976 Morinobu Endo and his group [5] were able to reveal the successful synthesis of single-walled carbon nanotube (SW-CNT) by TEM imaging.

A CNT is interpreted as rolled graphene. CNTs are classified by how they are rolled. The way of rolling graphene is characterized by a vector on the honeycomb lattice of graphene (Fig. 1). Merging two carbon atoms at the starting point and the ending point of the vector makes a CNT. The vector is called a chiral vector and can be represented as linear combination of primitive vectors of the honeycomb lattice of graphene. The set of two coefficients for the primitive vectors (n, m) is called chiral index, which can be used to specify the structure of CNT. The diameter d of the CNT is calculated as follows:

$$d = \frac{a\sqrt{m^2 + mn + n^2}}{\pi} \tag{1}$$

where $a = 0.246$ nm is lattice constant of graphene. Particularly, CNT with $n = m$ is called armchair type as the cut edge of it becomes armchair edge, and similarly CNT with $m = 0$ is called zigzag type. Other CNTs are called chiral type.

Electronic properties of CNT is drastically changed depending on the chiral index. Electronically, a CNT is seen as graphene with periodic boundary condition in the first place. Whether $\mathbf{k}$ vector satisfies the periodic boundary condition changes the situation. $\mathbf{k}$ vector is represented as $(2\mathbf{b}_1 + \mathbf{b}_2)/3$ using reciprocal primitive vectors $\mathbf{b}_1$, $\mathbf{b}_2$. Therefore, the

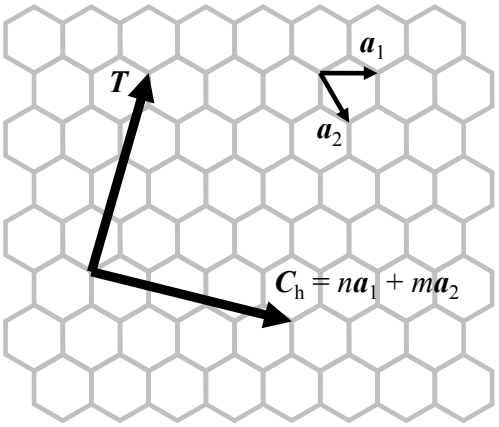

Fig. 1 Lattice vectors on a honeycomb lattice to classify CNTs. $\mathbf{C}_\mathrm{h}$ is the chiral vector and n and m are chiral indices. $\mathbf{T}$ is the tube axis of the resulting CNT. $|\mathbf{a}_1| = |\mathbf{a}_2| = 0.246$ nm.

condition is written as

$$\mathbf{C}_\mathrm{h} \cdot \mathbf{k} = (n\mathbf{a}_1 + m\mathbf{a}_2) \cdot \left(\frac{2\mathbf{b}_1 + \mathbf{b}_2}{3}\right) = \frac{4\pi n + 2\pi m}{3} = 2\pi l \tag{2}$$

$$\Leftrightarrow \quad 2n + m = 3l \tag{3}$$

$$\Leftrightarrow \quad m - n = 3l'. \tag{4}$$

with integers l, l'. If this condition is satisfied (i.e., $m - n = 3l'$), the CNT is metallic type. If not ($m - n = 3l' \pm 1$), there is finite gap between the conduction band and valence band and the CNT is semiconducting type. One can make a kind of periodic table for CNTs based on chiral index (Fig. 2). As CNTs are one-dimensional, they have spike-like Van Hove

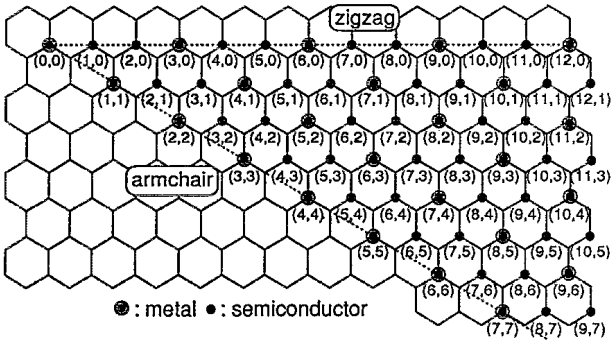

Fig. 2 "Periodic table" for CNTs (Ref. [6]). $(0, 0)$ is the starting point of the chiral vector. The chiral indices are assigned for each ending point. Resulting CNTs are either metallic or semiconducting type.

singularities in the density of states [7]. They have mirror-image spikes around the Fermi energy. A plot of energy separation between corresponding Van Hove singularities against tube diameter is called Kataura plot [8] (Fig. 3), which can be used to obtain chirality information from measured optical property. CNTs that have almost the same diameters may have different chiral index, therefore different electronic properties.

Arc discharge method was used when Iijima synthesized CNTs in 1991 [4]. During the DC arc-discharge with carbon electrodes, the carbon is evaporated and CNTs are grown

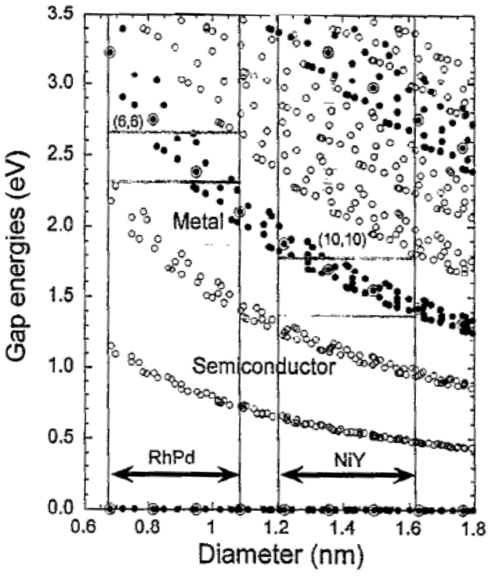

Fig. 3 Kataura plot (Ref. [8]). Calculated energy separation (gap) between corresponding Van Hove singularities are plotted as a function of tube diameter. The solid symbols are for metallic CNTs and the open ones for semiconducting. The double circles are for armchair CNTs. The arrows show the diameter distribution span caused by use of catalyst.

on the negative electrode. While the method uses higher temperature above 1700°C and the yield is lower, obtained CNTs have fewer structural defects than other methods [9]. Single-walled carbon nanotubes (SWCNTs) can also be obtained in this method by using graphite electrodes including catalytic metals [10, 11].

Chemical vapor deposition (CVD) method [12] is now common synthesis method of CNT. It uses metal particles as catalyst. The catalyst particles are embedded in support material with large surface area to achieve higher yield. Catalyst particles are then heated up to approximately 700°C in the reactor and gas phase substance containing carbon atoms is supplied. CNTs are therefore grown on the catalyst particles. Diameter of obtained CNTs depend on that of the catalyst particles. Addition of water into the reactor improves the efficiency of the growth of CNTs, which is known as super-growth [13]. The metal particles stay on the CNTs have to be removed afterwards by acid treatment, annealing [14] or centrifugation [15].

Double-walled carbon nanotubes (DWCNTs) can be synthesized by above methods by tuning the conditions [16, 17]. Peapod method is another way of synthesizing DWCNTs, which uses predefined SWCNTs and fullerene (C_{60}) molecules. SWCNT with C_{60} molecules inside ($(C_{60})_n$@SWCNT) is called peapod [18, 19]. Efficient way of synthesizing peapods is heating C_{60} molecules with SWCNTs at 400°C [20]. The structure is unchanged up to 800°C, but the C_{60} molecules start to coalesce above 800°C and most of them turn into DWCNTs at 1200°C [21].

Thanks to the van der Waals force, CNTs attract each other. The CNT-CNT potential in parallel configuration has a minimum at certain distance, which depends on the tube radius (Fig. 4) [22]. The binding energy calculated for two parallel CNTs [23] gets higher for larger tube radius (Fig. 5), and larger number of walls, in case of multi-walled CNT (Fig. 6). Also, the hydrophobic nature of CNTs helps them to aggregate in solution. Therefore, CNTs tend to form bundles or ropes consisting of 50-100 individual CNTs. To obtain individual CNTs out of bundles, surfactants such as sodium dodecyl sulfate, sodium

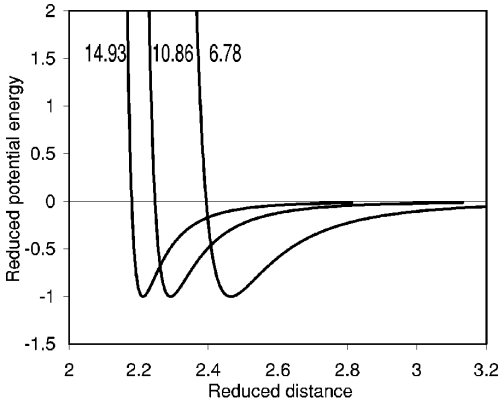

Fig. 4 Calculated tube-tube interaction potential energies as a function of tube-tube distance in parallel configuration (Ref. [22]). The energy is normalized by the well depth, and the distance by the tube radius. The numbers are the tube radii in Å.

インターネット公表に対する著作権者からの許諾を得ていないため非公表

Fig. 5 Radius dependence of the binding energy of two parallel (closed square) or crossing (closed triangle) CNTs (Ref. [23]). Results of molecular dynamics simulation are denoted by MD. β is the crossing angle.

インターネット公表に対する著作権者からの許諾を得ていないため非公表

Fig. 6 Wall number dependence of the binding energy of two parallel (square) or crossing (circle) CNTs (Ref. [23]). β is the crossing angle.

dodecyl benzene sulfonate, or sodium carboxymethyl cellulose are used. Alternatively, as-grown individual CNTs can also be used.

Especially for electronic applications, separation of metallic and semiconducting CNTs is important. Not only the physical size, chemical reactivity of a CNT is also affected by its chirality, as the density of states at Fermi energy is modified. Density gradient ultracentrifugation (centrifugation with acceleration $10^5 \sim 10^6$ g) with optimum surfactant enables the sorting of CNTs by diameter, bandgap and electronic type (Fig. 7) [24], or even by chirality [25]. Separation by electronic type with normal speed centrifugation ($\sim 10^4$ g), combined with selective trap by agarose gel, is also reported [26]. Sorting is also possible with chromatography. Using the size exclusion chromatography, not only sorting by size [27], separation by electronic type is also achieved [28]. DNA-wrapping of CNT followed by ion exchange chromatography is used to separation by chirality [29, 30].

Basically the same Raman peaks as graphene also appears in Raman spectroscopy on carbon nanotubes, but with some modifications. Optical vibration modes that are longitudinal and transverse to the tube axis are not identical due to the curvature of the tube,

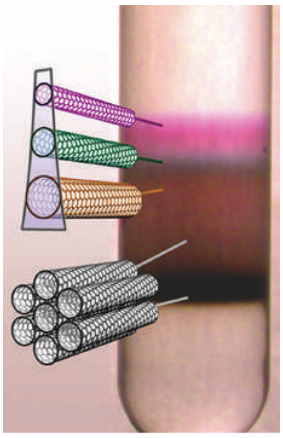

Fig. 7 CNTs sorted by the density gradient ultracentrifugation technique (Ref. [24]). Higher density solution flows into the centrifuge tube form the bottom. The CNT solution shows various colors reflecting its electronic property.

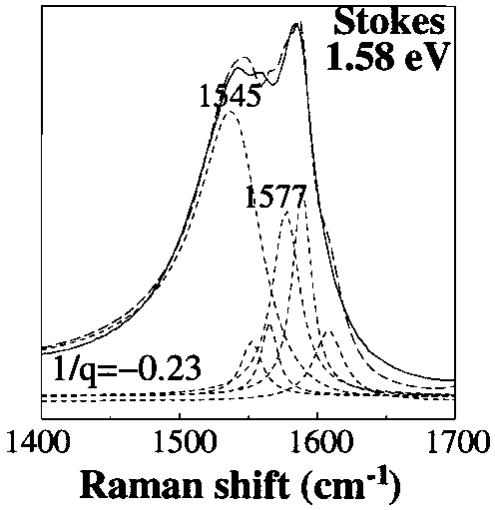

Fig. 8 Breit-Wigner-Fano (BWF) type peak observed in Raman spectrum on CNT sample with diameter 1.49±0.2 nm (Ref. [31]). The solid line is experimental data and the dashed lines are fittings to multiple Lorentzians and BWF shape centered at 1545 cm $^{-1}$.

and resulting G peak splits into two peaks: G+ and G-. Raman shift of G- peak varies depending on the tube diameter because it comes from transverse mode. There also appears additional peak, which comes from radial breathing mode (RBM). Raman shift of RBM is inversely proportional to the tube diameter.

For metallic CNTs, G- peak get additional modification. As the system is complex of continuous electron states and discrete phonon states, G- peak becomes asymmetric Breit-Wigner-Fano (BWF) shape (Fig. 8) [31]. This enables the determination whether the CNTs are metallic or not without performing transport measurement.

1.2. Graphene

Graphene is a monoatomic sheet of carbons, viewed as isolated single layer out of layered material, graphite. Theoretically, it has been object of consideration since 1940s and its peculiar linear energy dispersion relation was known [32]. It was in 2004 when experimental isolation of graphene out of graphite was realized [33]. It was surprising because you can easily obtain an ideal 2-dimensional electron system, which also remains stable in the atmosphere. From the viewpoint of fundamental physics, too, graphene has curious properties including the Dirac fermion behavior of quasiparticles in it explained in relativistic quantum mechanics. Since then, experimental research on graphene spread quickly. Electron mobility at room temperature on SiO_2 substrate is reported to be $\sim 15,000$ cm^2/V·s [33],

while mean free path is reported to be over 1 μm [34], both being high values. It is also mechanically strong and flexible. So, applications to the devices, including spintronics, are expected.

From the viewpoint of fundamental physics, graphene's distinctive energy band structure is a subject of the interest. The bands are crossing each other linearly at K and K' points in Brillouin zone. The bands forming cones are called Dirac cones, and the vertex is called Dirac point (Fig. 9). Graphene is called massless Dirac fermion system as quasiparticles in linear dispersion relation region neighboring the Dirac point are described by Dirac Hamiltonian for massless fermion (Weyl Hamiltonian) .

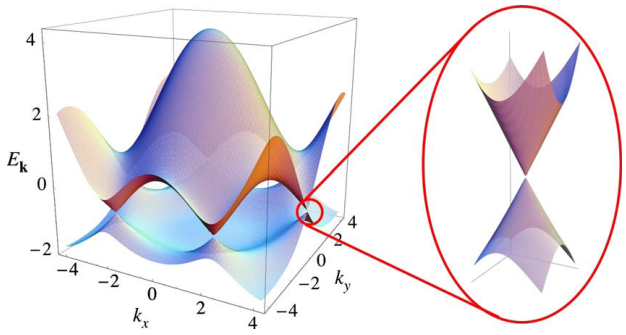

Fig. 9 Energy band structure of graphene obtained by tight-binding calculation [35].

Using field effect transistor (FET) structure, Fermi energy of graphene can be tuned by manipulating the electrochemical potential with gate voltage, as it is only one-atom-thick layer. The gate voltage dependence of conductance measured by sweeping the gate voltage reflects the energy band structure. Gate voltage dependence of resistance shows the peak structure called Dirac peak when the Fermi energy crosses the Dirac point and the carrier density decreases, where conductivity shows minimum, while resistance shows maximum (Fig. 10).

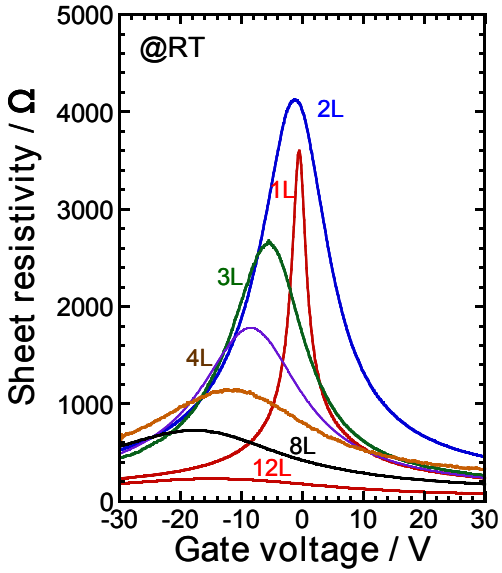

Fig. 10 Gate voltage dependence of sheet resistances of monolayer (1L) and multilayer (2∼12L) graphenes [36]. The resistance reaches maximum (Dirac peak) when the Fermi energy crosses the Dirac point.

1.3. Transport properties in nanocarbon materials

1.3.1. Tomonaga-Luttinger liquid (TLL)

Electron system with spacial dimension higher than one is described with Fermi liquid theory. For free electron system, the states are occupied from low energy up to Fermi energy. Therefore, distribution function for the system looks like a step function (Fig. 11). For electrons with interaction, the distribution is modified, still with finite discontinuity at the Fermi energy. The step height correspond to the fraction of the elementary fermionic excitations that remains in this quasiparticle state. Finite discontinuity means that the lifetime of quasiparticles near Fermi level is long enough, which makes Fermi liquid theory work. However, in one dimensional system, Fermi surface disappears and Fermi liquid theory fails. Fermionic excitations can no longer survive and are converted into collective ones. The system is described with Tomonaga-Luttinger liquid (TLL) theory instead.

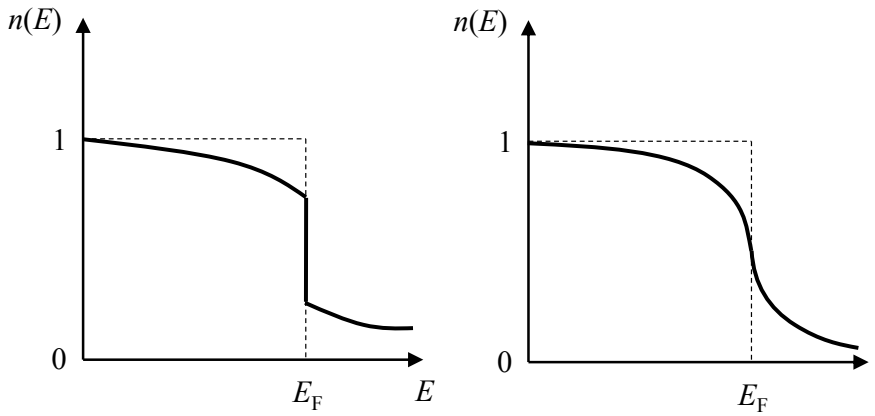

Fig. 11 left: Distribution function of electrons systems in spacial dimensions higher than one. There is a finite discontinuity at the Fermi energy E_{F}. right: Distribution function of one dimensional electron system. There is no discontinuity at E_{F}.

Instead of original free electron model, purely linear spectrum is considered on Tomonaga-Luttinger model [37, 38]. Fermionic operator close to the Fermi surface is written as

$$\psi(x) \cong \frac{1}{\Omega}\left[\sum_{-\Lambda<k-k_{\mathrm{F}}<\Lambda} e^{ikx}c_k + \sum_{-\Lambda<k+k_{\mathrm{F}}<\Lambda} e^{ikx}c_k\right] \tag{5}$$

where $\Omega = L$ for one dimension. Thus it is decomposed into right movers and left movers

$$\psi(x) = \psi_{\mathrm{R}}(x) + \psi_{\mathrm{L}}(x). \tag{6}$$

g_1, g_2 and g_4 scattering processes are possible (Fig. 12). If spin is ignored for simplicity here, the g_1 process is identical to g_2, since the final state of g_1 is transformed to that of g_2 by exchanging the particles. Using bosonization, g_4 process of right movers can be written

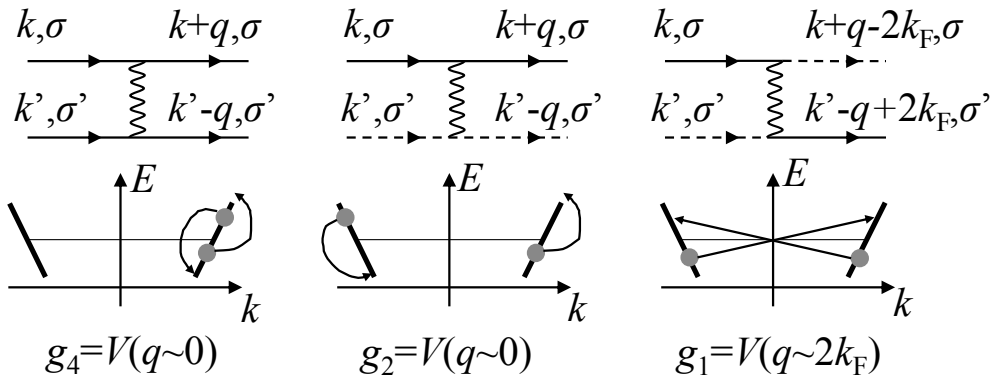

Fig. 12 Scattering processes near the Fermi energy in one dimensional system.

as

$$\frac{g_4}{2}\psi_{\mathrm{R}}^{\dagger}(x)\psi_{\mathrm{R}}(x)\psi_{\mathrm{R}}^{\dagger}(x)\psi_{\mathrm{R}}(x) = \frac{g_4}{2}\rho_{\mathrm{R}}\rho_{\mathrm{R}} \tag{7}$$

$$= \frac{g_4}{2}\frac{1}{(2\pi)^2}(\nabla\phi - \nabla\theta)^2 \tag{8}$$

and similarly for left movers ($\psi - \theta \to \psi + \theta$), with bosonic fields ϕ and θ. Total g_4 interaction is then

$$\frac{g_4}{(2\pi)^2}\int \mathrm{d}x\left[(\nabla\phi)^2 + (\nabla\theta)^2\right] \tag{9}$$

and it renormalizes the velocity of excitations v_{F} to

$$u = v_{\mathrm{F}}\left(1 + \frac{g_4}{\pi v_{\mathrm{F}}}\right). \tag{10}$$

g_2 process can be written as

$$g_2\psi_{\mathrm{R}}^{\dagger}(x)\psi_{\mathrm{R}}(x)\psi_{\mathrm{L}}^{\dagger}(x)\psi_{\mathrm{L}}(x) = g_2\rho_{\mathrm{R}}(x)\rho_{\mathrm{L}}(x) \tag{11}$$

$$= \frac{g_2}{(2\pi)^2}(\nabla\phi - \nabla\theta)(\nabla\phi + \nabla\theta) \tag{12}$$

$$= \frac{g_2}{(2\pi)^2}\left[(\nabla\phi)^2 - (\nabla\theta)^2\right], \tag{13}$$

which modifies not only the velocity but also relative weights of the $\nabla\phi$ and $\nabla\theta$. The whole Hamiltonian can be written as

$$H = \frac{1}{2\pi}\int \mathrm{d}x\left[uK\left(\pi\Pi(x)\right)^2 + \frac{u}{K}\left(\nabla\phi(x)\right)^2\right] \tag{14}$$

where $\Pi(x) = \frac{1}{\pi}\nabla\theta(x)$ (conjugate momentum) with two parameters u and K.

$$uK = v_{\mathrm{F}}\left(a + \frac{g_4}{2\pi v_{\mathrm{F}}} - \frac{g_2}{2\pi v_{\mathrm{F}}}\right) \tag{15}$$

$$\frac{u}{K} = \left(a + \frac{g_4}{2\pi v_{\mathrm{F}}} + \frac{g_2}{2\pi v_{\mathrm{F}}}\right) \tag{16}$$

are solved as

$$u = v_{\mathrm{F}} \left[(1 + y_4/2)^2 - (y_2/2)^2 \right]^{1/2} \tag{17}$$

$$K = \left(\frac{1 + y_4/2 - y_2/2}{1 + y_4/2 + y_2/2} \right)^{1/2} \tag{18}$$

where $y_i = g_i/(\pi v_{\mathrm{F}})$. Therefore, one dimensional interacting system is described by free bosons. K is interpreted as interaction of quasiparticles; $K > 1$ is attractive and $K < 1$ is repulsive.

When spin freedom is introduced, g_1 process is no longer identical to g_2. The g_1 process is included as

$$H_1 = \int \mathrm{d}x g_{1\parallel} \sum_\sigma \left[\psi^\dagger_{\mathrm{L},\sigma} \psi^\dagger_{\mathrm{R},\sigma} \psi_{\mathrm{L},\sigma} \psi_{\mathrm{R},\sigma} \right] + g_{1\perp} \sum_\sigma \left[\psi^\dagger_{\mathrm{L},\sigma} \psi^\dagger_{\mathrm{R},-\sigma} \psi_{\mathrm{L},-\sigma} \psi_{\mathrm{R},\sigma} \right]. \tag{19}$$

After bosonization, the total Hamiltonian separates into charge part and spin part:

$$H = H_\rho + H_\sigma \tag{20}$$

with H_ρ again purely quadratic, but H_σ not:

$$H_\sigma = H^0_\sigma + \frac{2 g_{1\perp}}{(2\pi\alpha)^2} \int \mathrm{d}x \cos(2\sqrt{2}\phi_\sigma) \tag{21}$$

where H^0_σ is quadratic. Parameters are also separated into u_ρ, K_ρ and u_σ, K_σ. Charge and spin excitations now move individually and called spinon and holon. This charge-spin separation is an important consequence of the 1D model.

Physical quantities can now be computed [39] using modified spectrum:

$$\epsilon(p) = u|p| = u \frac{2\pi|n|}{L}. \tag{22}$$

For simplest example, specific heat is:

$$C_{\mathrm{V}} = \frac{\mathrm{d}E}{\mathrm{d}T} = \frac{\mathrm{d}}{\mathrm{d}T} \sum_{p \neq 0} \epsilon(p) f_{\mathrm{B}}\left(\epsilon(p)\right) \tag{23}$$

$$= \beta^2 \sum_{p \neq 0} \epsilon(p)^2 \frac{e^{\beta\epsilon(p)}}{(e^{\beta\epsilon(p)} - 1)^2} \tag{24}$$

$$= \frac{u^2}{4T^2} \sum_{p \neq 0} \frac{p^2}{\sinh^2(\beta u p/2)} \tag{25}$$

$$= \frac{u^2}{4T^2} \frac{L}{2\pi} \left[\frac{\pi^2 8}{3(\beta u)^3} \right] \tag{26}$$

$$= \frac{T}{u} \left(\frac{L\pi}{3} \right). \tag{27}$$

For comparison, in case of free fermions:

$$E = 2\sum_p \epsilon_p^{\mathrm{F}} f_{\mathrm{F}}(\epsilon_p^{\mathrm{F}}) \tag{28}$$

$$C_{\mathrm{V}} = \frac{L}{\pi v_{\mathrm{F}}}\beta^2 \int_{-\infty}^{\infty} \mathrm{d}\epsilon \frac{\epsilon^2}{4\cosh^2(\beta\epsilon/2)} \tag{29}$$

$$= \frac{T}{v_{\mathrm{F}}}\left(\frac{L\pi}{3}\right). \tag{30}$$

Similarly, thermodynamic (static) quantities such as susceptibility and compressibility look like those of Fermi liquid, except for renormalized coefficients.

For dynamic quantities, the situation changes. Single particle Green's function is given by

$$G_{\mathrm{R}}(r) = -\langle \psi_{\mathrm{R}}(r)\psi_{\mathrm{R}}^{\dagger}(0)\rangle \tag{31}$$

$$= -\frac{e^{ik_{\mathrm{F}}x}}{2\pi\alpha}\langle e^{i(\phi(r)-\theta(r))}e^{-i(\phi(0)-\theta(0))}\rangle \tag{32}$$

$$= -\frac{e^{ik_{\mathrm{F}}x}}{2\pi\alpha}e^{-}\left[\frac{K+K^{-1}}{2}F_1(r) + F_2(r)\right] \tag{33}$$

where

$$F_1(r) = \frac{1}{2}\log\left[\frac{x^2+(u|\tau|+\alpha)^2}{\alpha^2}\right] \tag{34}$$

$$F_2(r) = -i\mathrm{Arg}(y_\alpha + ix) \tag{35}$$

$$y_\alpha = u\tau + \alpha\mathrm{Sign}(\tau) \tag{36}$$

Using this, occupation factor is given by

$$n(k) = \int \mathrm{d}x e^{-ikx} G_{\mathrm{R}}(x, \tau = 0^-) \tag{37}$$

$$= \int \mathrm{d}x e^{i(k_{\mathrm{F}}-k)x}\frac{-1}{2\pi\alpha}e^{-\left[\frac{K+K^{-1}}{2}F_1(x,\tau=0^-)+F_2(x,\tau=0^-)\right]}. \tag{38}$$

At $T = 0$ this gives

$$n(k) = \int \mathrm{d}x e^{i(k_{\mathrm{F}}-k)x}\frac{-1}{2\pi\alpha}\left(\frac{\alpha}{\sqrt{x^2+\alpha^2}}\right)^{\frac{K+K^{-1}}{2}} e^{-i\mathrm{Arg}(-\alpha+ix)}, \tag{39}$$

which is the Fourier transform of a power law. The resulting power law behavior of the occupation factor

$$n(k) \propto |k-k_{\mathrm{F}}|^{\frac{K+K^{-1}}{2}-1} \tag{40}$$

characterizes TLL. Similarly, dynamic quantities obtained from correlation function, such as T1 in NMR and electrical conductivity, behave as power law.

In 1950, Tomonaga showed that low energy excitation of the system is described by two collective modes behave like bosons [37], followed by more general consideration by Luttinger in 1963 [38]. The model they considered is now called Tomonaga-Luttinger model. Later in 1981, Haldane stated that the behavior is common characteristics for 1D many-body system with interactions [40], and now is being confirmed in many models. Nowadays, spinon and holon are handled with conformal field theory and studied as Tomonaga Luttinger liquid.

Tomonaga Luttinger liquid behavior is observed in various 1D systems, such as quantum Hall edge state [41], quantum wire in semiconductor heterostructure [42], and CNT.

In CNT, there are two species of Fermions (each with two spin orientations), and thus four degrees of freedom instead of two in a normal TLL (Fig. 13). Wave function for each species is of the form:

$$\psi_j(x,y) = \psi_{x,j}(x)\psi_{y,j}(y) \tag{41}$$

where x is along the axis of the tube and y is transverse direction. Consequently, four collective modes are present. C As a first approximation, one can neglect backward scat-

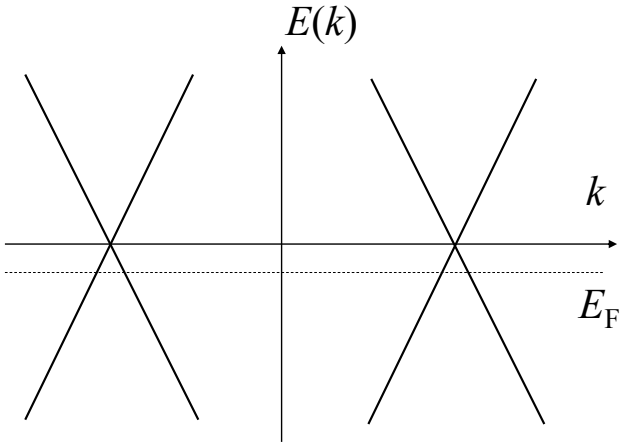

Fig. 13 Dispersion relation of (metallic) CNT with two linear bands crossing at the Fermi level E_{F}.

tering and thus interactions only affects a change mode: $K_{\rho-} = K_{\sigma+} = K_{\sigma-} = 1$ and only $K_{\rho+} \neq 1$. This gives occupation factor [39]

$$n_{\mathrm{bulk}}(\epsilon) \sim \epsilon^{(K_{\rho+}+K_{\rho+}^{-1}-2)/8} \tag{42}$$

in the middle of the CNT. Assuming the end of the CNT as hard boundary, the occupation factor is modified to

$$n_{\mathrm{end}}(\epsilon) \sim \epsilon^{(K_{\rho+}-1)/4}. \tag{43}$$

The occupation factor is reflected in the transport properties. Electrons tunnel into end/bulk of the CNT give [43, 44]

$$\begin{array}{ll} \mathrm{d}I/\mathrm{d}V \propto V^{\alpha} & (eV \gg k_{\mathrm{B}}T) \\ G(T) \propto T^{\alpha} & (eV \ll k_{\mathrm{B}}T) \end{array} \tag{44}$$

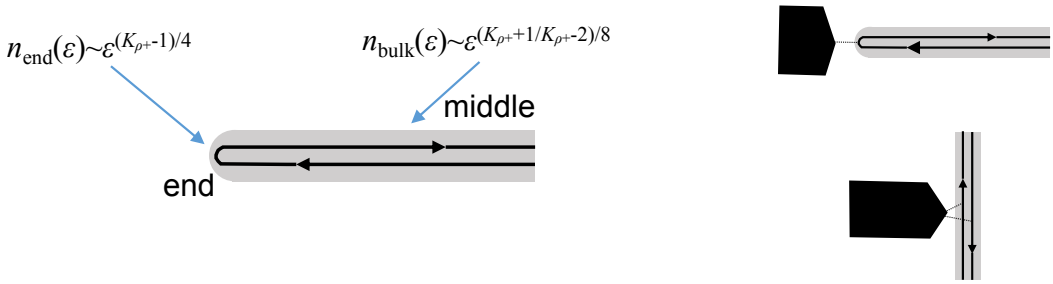

Fig. 14 left: occupation number for the Tomonaga-Luttinger liquid (TLL) with a hard boundary. right upper: Electron tunneling from an electrode to the end of TLL (end contacted configuration). right lower: tunneling to the bulk state (bulk contacted configuration).

with

$$\alpha_{\text{end}} = (g^{-1} - 1)/4 \tag{45}$$
$$\alpha_{\text{bulk}} = (g^{-1} + g - 2)/8 \tag{46}$$

where g is called Luttinger parameter. For finite length tube or rope, the Luttinger parameter is given by [45]

$$g = \left[1 + \frac{2U}{\Delta}\right]^{-1/2} \tag{47}$$

where U is charging energy of the tube and Δ is single particle level spacing. From single-electron transport experiments on SWCNT [46] and theoretical estimates [47], $U/\Delta \approx 6$, which yields $g \approx 0.28$ and gives

$$\alpha_{\text{end}}(\text{theory}) = 0.65 \tag{48}$$
$$\alpha_{\text{bulk}}(\text{theory}) = 0.24. \tag{49}$$

The power law in transport is confirmed in experiments. Bockrath *et al.* showed that the configuration of the electrode determines whether it become bulk contact or end contact (Fig. 15) [45]. If electrodes are deposited over a CNT rope, electrons are confined between the electrodes and result in end contact with exponent $\alpha \approx 0.6$. Contrary to that, if a CNT is put onto predefined electrodes, electrons are not confined and result in bulk contact with $\alpha \approx 0.3$.

The exponent of the power law is modified for multi-walled CNTs. Tunneling into the outermost shell of multi-walled CNT with N conducting shells gives exponents [48]

$$\alpha_{\text{end}} = (g^{-1} - 1)/4N \tag{50}$$
$$\alpha_{\text{bulk}} = (g^{-1} + g - 2)/8N. \tag{51}$$

This result can also be applied to the ropes of N SWCNTs. For the limit $N \to \infty$, the exponents approach 0, which is the value of Fermi liquid.

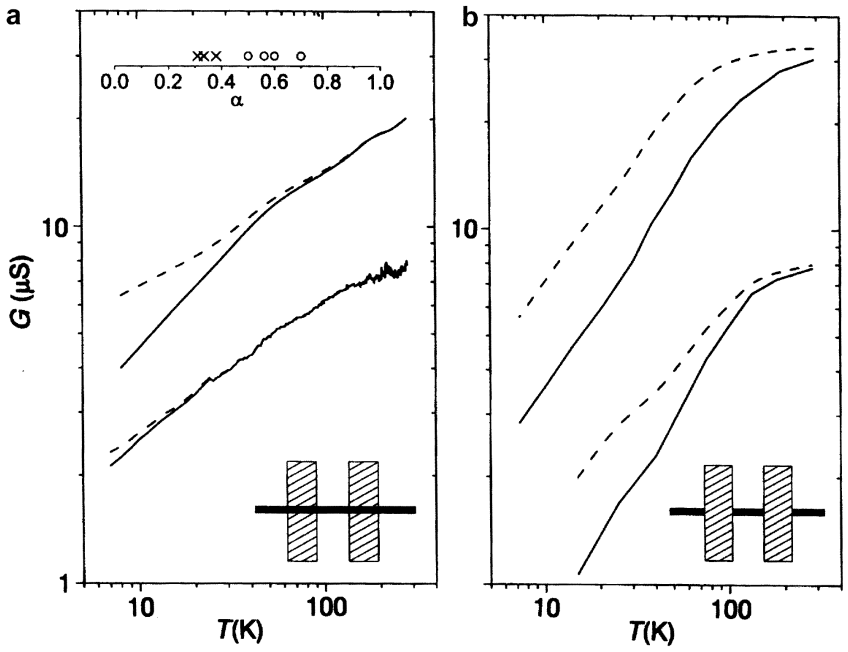

Fig. 15 An experimental realization of bulk contact and end contact [45]. Temperature dependence of conductance of CNT with bulk contacts (left) and end contacts (right). The solid lines are raw data and the dashed lines are corrected using Coulomb blockade model. The inset of the left panel shows the distribution of the exponents α of power-law. The open circles are end contacted samples and the crosses are end contacted ones.

For TLL to TLL tunneling, the Luttinger parameter is theoretically doubled [49, 50]:

$$\alpha_{\mathrm{end-end}} = 2\alpha_{\mathrm{end}} = (g^{-1} - 1)/2 \tag{52}$$

$$\alpha_{\mathrm{bulk-bulk}} = 2\alpha_{\mathrm{bulk}} = (g^{-1} + g - 2)/4. \tag{53}$$

This was confirmed experimentally by Postma *et al.* [51]. They used AFM tip to bend a SWCNT sharply to make a buckle, which they confirmed to work as end-end junction with exponent $\alpha = 1.4$. They also cut a SWCNT by AFM tip and made crossing, which works as bulk-bulk junction with $\alpha = 0.50$.

The behavior of CNT-CNT junction also depends on electronic type (metallic/semiconducting) of the CNTs. While CNT-CNT junction with same electronic types show ohmic behavior, junction with different types result in band bending and show Schottky behavior [52].

1.3.2. Variable range hopping

In a condition such that the amount of thermally activated carriers are sufficiently small, hopping conduction emerges as the major conduction mechanism. Hopping conduction is mediated by overlapping tails of wave functions from neighboring localized states. Temperature dependence of the hopping conduction is derived by qualitative consideration [53].

Consider the localized states at energy level ϵ_i near the Fermi energy μ: $|\epsilon_i - \mu| \leq \epsilon_0$ (Fig. 16). Using the density of states at Fermi energy $g(\mu)$, the concentration of states in

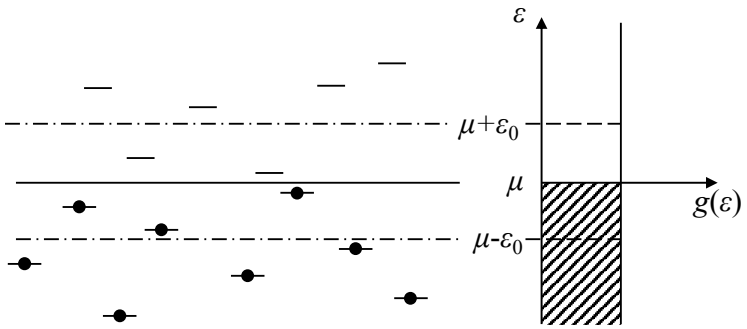

Fig. 16 Distribution of localized states near the Fermi level μ. $g(\epsilon)$ is the density of states at energy ϵ.

this region is $N(\epsilon_0) = 2g(\mu)\epsilon_0$. Here, density of states near the Fermi energy is assumed to be constant. Therefore, typical spacial distance between localized states is $N(\epsilon_0)^{-1/d}$ with spacial dimension of the system d. The hopping amplitude depends on the distance and energy spacing between the states, both exponentially. Therefore, the resistivity is written as

$$\rho = \rho_0 \exp\left(\frac{N(\epsilon_0)^{-1/d}}{\xi} + \frac{\epsilon_0}{k_\mathrm{B}T}\right) \tag{54}$$

$$= \rho_0 \exp\left(\frac{(2g(\mu)\epsilon_0)^{-1/d}}{\xi} + \frac{\epsilon_0}{k_\mathrm{B}T}\right) \tag{55}$$

where ξ is the radius of localized states. This, as a function of ϵ_0, has a minimum at

$$\epsilon_0 = \epsilon_0(T) \equiv \left(\frac{\xi d\,(2g(\mu))^{1/d}}{k_\mathrm{B}T}\right)^{1+1/d}. \tag{56}$$

The band with the width $\epsilon_0(T)$ is called the optimal band. ρ with optimal band is therefore

$$\rho(T) = \rho_0 \exp\left(\frac{d+1}{\xi d}\left(\frac{\xi d}{2g(\mu)k_\mathrm{B}T}\right)^{1/(d+1)}\right) \tag{57}$$

$$= \rho_0 \exp\left((T_0/T)^{1/(d+1)}\right) \tag{58}$$

with

$$T_0 = \frac{\beta_d}{k_\mathrm{B}g(\mu)\xi^d} \tag{59}$$

where β_d is d-dependent parameter. The case of $d = 3$ was derived by Mott, so it is called Mott's law. Here, average hopping length is temperature dependent, contrary to

the nearest-neighbor hopping with constant hopping length. Eq. (58) is then called d-dimensional variable range hopping (VRH). Arrhenius behavior results from nearest neighbor hopping correspond to $d = 0$ case of the formula.

To obtain the value of β_d, further consideration with percolation method [54] is needed. According to a calculation with three-dimensional finite sites array, $\beta_3 = 22.8 \pm 1.2$ [55]. Extrapolation to infinite array gives $\beta_3 = 21.2 \pm 1.2$ [56]. Two-dimensional case is also calculated in [55], which gives $\beta_2 = 13.8 \pm 0.8$.

Efros and Shklovskii considered the effect of Coulomb interaction on VRH [57]. As a result of finite Coulomb gap at the Fermi energy, d is fixed to 1, regardless of the dimension of the system. The case is called Efros and Shklovskii (ES) VRH.

The VRH contribution to the magnetoresistance is as follows [58, 59]:

$$\frac{\Delta G}{G} = -A_{\mathrm{KK}} \frac{H^2}{H_{\mathrm{KK}}^2 + H^2} \tag{60}$$

$$\mu_{\mathrm{B}} H_{\mathrm{KK}} = a k_{\mathrm{B}} T \left(\frac{T_0}{T}\right)^{1/4}, A_{\mathrm{KK}} = 1 - \exp\left[-b\left(\frac{T_0}{T}\right)^{1/4}\right], \tag{61}$$

where a and b are constants depending on the system. KK stands for Kurobe and Kamiura.

1.3.3. Weak localization

Let τ be the phase coherence length. In ideal Fermi liquid, $\tau \sim T^{-2}$. Here, τ and T are related as follows:

$$\frac{1}{\tau} \sim \Gamma T^p. \tag{62}$$

Therefore, phase coherence length L is as follows:

$$L = \sqrt{\tau D} = \sqrt{\frac{D}{\Gamma}} T^{-p/2} \tag{63}$$

where D is diffusion coefficient. Correction to conductivity by weak localization is in the following form [60]:

$$\Delta\sigma = \begin{cases} \dfrac{e^2}{\pi^2\hbar}\sqrt{\dfrac{\Gamma}{D}} T^{p/2} & (d = 3) \\ \dfrac{pe^2}{2\pi^2\hbar} \log T & (d = 2) \end{cases} \tag{64}$$

p depends on the scattering mechanism and $p < 2$ for disordered system [61].

The 2D WL contribution to the magnetoresistance is as follows [62]:

$$\Delta G = \frac{e^2}{2\pi^2\hbar}\left[\psi\left(\frac{1}{2} + \frac{1}{x}\right) + \ln(x)\right] \tag{65}$$

$$x = L_{\mathrm{Th}}^2 \frac{4eH}{\hbar}, \tag{66}$$

where L_{Th} is Thouless length and $\psi(x)$ is the digamma function:

$$\psi(x) = \frac{\mathrm{d}}{\mathrm{d}x}\ln\Gamma(x) = \frac{\mathrm{d}}{\mathrm{d}x}\ln\left(\int_0^\infty t^{x-1}e^{-t}\mathrm{d}t\right). \tag{67}$$

The 3D WL contribution is as follows [63, 64]:

$$\Delta G = \frac{e^2}{2\pi^2\hbar}\sqrt{\frac{eH}{\hbar}}f_3(x) \tag{68}$$

$$f_3(x) = \sum_{n=0}^{\infty}\left[2\left(\sqrt{n+1+\frac{1}{x}} - \sqrt{n+\frac{1}{x}}\right) - \frac{1}{\sqrt{n+1/2+1/x}}\right] \tag{69}$$

where x is same as 2D case. The infinite sum is approximated by following formula [65]:

$$f_3(x) \approx 2\left(\sqrt{2+\frac{1}{x}} - \sqrt{\frac{1}{x}}\right) - \left(\frac{1}{2}+\frac{1}{x}\right)^{-1/2} - \left(\frac{3}{2}+\frac{1}{x}\right)^{-1/2} + \frac{1}{48}\left(2.03+\frac{1}{x}\right)^{-3/2} \tag{70}$$

with accuracy better than 0.1% for all x.

1.4. Objective and structure of this thesis

This thesis has the following four major objectives.

1. Investigation of electronic properties of pure CNT networks
   Electronic properties (mainly transport properties) of metallic SWCNT and DWCNT will be investigated by transport measurements in a wide temperature range down to 0.3 K and in high magnetic fields up to 9 T using CNT network samples (buckypapers) of high sorting purity (99%) which became recently available. One of the major aims here is to study roles of the underlying TLL nature of CNT on transport properties of macroscopic network samples which may have wide applications.

2. Confirmation of metallicity of 1D sulfur chains embedded in CNTs and search for its possible superconductivity
   By comparing electrical conductivity of network samples of CNT with and without 1D sulfur chains, the recently reported metallicity of the sulfur chain will be tested. The measurement will be extended below 0.3 K using a dilution refrigerator to see if there is a superconducting transition.

3. Observation of oxygen exposure effects on transport properties of monolayer graphene
   Graphene samples with high crystallinity are usually obtained by exfoliation of graphite in the air. It is important to know the effect of exposure to oxygen gas on electronic properties of graphene and for its application to gas sensor. Detailed time evolution of transport properties of monolayer graphene as well as bilayer one exposed to oxygen will be investigated in this research and compared with the previous research on bilayer graphene.

4. Attempts of band gap opening by gas adsorption
   Controlled amount of Kr gas will be adsorbed on graphene to confirm the theoretical prediction of bandgap opening by symmetry breaking due to atoms/molecules adsorption.

In the rest of this thesis, Chapter 2 is devoted to describe results of the first two objectives on CNT networks. In this chapter, theoretical background and previous experimental reports are reviewed in Section 2.1, and then experimental methods (Section 2.2), experimental results and related discussions (Section 2.3) and conclusion (Section 2.4) follow. Chapter 3 is devoted to show results of the oxygen exposure experiments on graphene. In this chapter, after reviewing the previous experimental reports in Section 3.1, experimental methods (Section 3.2), experimental results and related discussions (Section 3.3) and conclusion (Section 3.4) are given. About the band gap opening of graphene by Kr gas adsorption, brief descriptions are given in Chapter 4 in a similar organization to the previous two Chapters. Finally, overall summary of this research is given in Chapter 5.

2. Transport properties of metallic carbon nanotube network

本章については、雑誌で刊行予定のため非公開

3. Effects of oxygen adsorption on transport properties of graphene

3.1. Background

3.1.1. Carrier doping to graphene by adsorption of molecules[1]

Transport properties of graphene is sensitive to carrier density increase or decrease, caused by adsorption of various gas molecules with charge transfer(Fig. 54), which leads to the application to gas sensors.

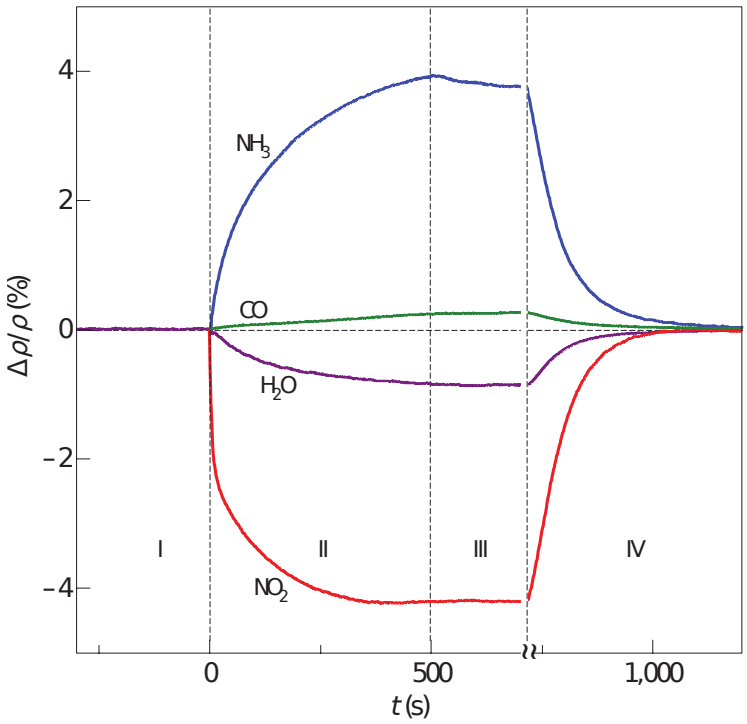

Fig. 54 Temporal change of electrical resistivity of monolayer exfoliated graphene by gas adsorption [101]. I: vacuum, II: exposure to each gas diluted to 1 ppm with helium or nitrogen, III: evacuation, IV:annealing at 150°C.

Detection of individual adsorption and desorption of molecules has been realized with

[1]Surface transfer doping is argued here. Substitutional doping, meaning the alternation of carbon atoms with other kinds of atoms, is not the subject.

Hall resistance measurement [101]. Recently, detection of individual CO_2 within 2-terminal resistance using suspended strained graphene device [102] was also reported. These reports qualifies the capability of graphene as an ultimate gas sensor device.

Adsorbed molecule accepts electrons from graphene, or holes are doped to graphene, only if electron affinity of adsorbed molecule is higher than work function of graphene [103]. It is confirmed that in oxygen atmosphere graphene is hole-doped [104, 105], in spite of the electron affinity 0.44 eV lower than work function of graphene 4.6 eV, prohibiting the direct transfer of electrons. Actual transfer of electros is thought to be achieved through such electrochemical reaction that $O_2 + 2H_2O + 4e^- \rightarrow 4OH^-$ [106] and hole doping occurs. Water in the atmosphere or residual water on SiO_2 substrate contributes to the reaction. In water-rich atmosphere, irreversible hole doping occurs [107]. Irreversible hole doping is reported to occur also by long-period exposure to the atmosphere [105].

Such electrochemical reaction shown above is expected to change its reactivity by modifying Fermi energy by applying gate voltage [108, 109]. In case of hole doping by oxygen, it indeed has been confirmed experimentally [110]. Especially in [110], temporal change of the hole doping speed to bilayer graphene sample by oxygen was analyzed in detail, to show that time derivative of amount of doping obeys power law function of time. It was also reported that change in conductance (not that at Dirac point; gate voltage was not applied) obeys double exponential function of time [111] (Fig. 55).

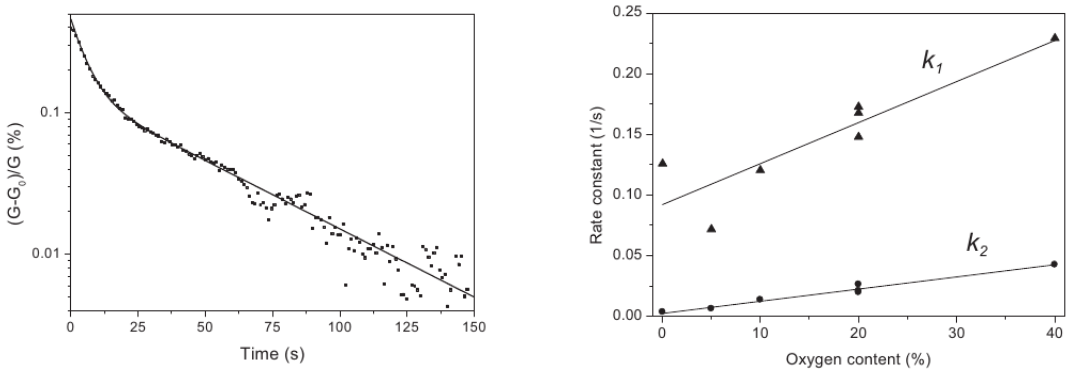

Fig. 55 Left: temporal change of conductance after changing the oxygen content of atmosphere from 10% to 21%. The change well obeys double exponential function (solid line). Right: oxygen content dependence of two rate constants k_1 and k_2. Solid lines are linear fits.

In this thesis, temporal change of the hole doping to monolayer graphene by oxygen is analyzed. Also, change in the resistance at Dirac point is considered.

3.1.2. Effects of oxygen physisorption on graphene

Figure 56 shows the phase diagram of oxygen molecules adsorbed on graphite surface without charge transfer [112]. The solid phases are all incommensurate to graphite, so no bandgap opening by symmetry breaking is expected by oxygen physisorption on graphene.

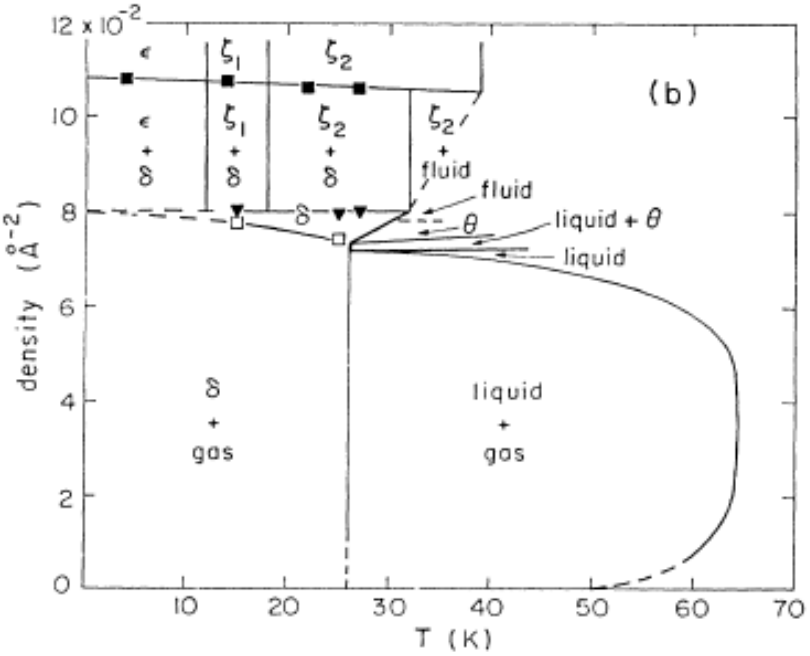

Fig. 56 Temperature-areal density phase diagram of oxygen molecules physisorped on graphite [112]. ζ_1, ζ_2, δ, ϵ and θ are all incommensurate solid phase.

While an oxygen molecule is electrically neutral, triplet configuration of electrons at the ground state shows paramagnetism and it behaves as magnetic impurity. An example is the Kondo effect observed on the system of oxygen molecules physisorped on gold surface [113].

3.2. Experimental methods

3.2.1. Sample preparation for graphene

Major production methods of graphene are micromechanical cleavage method (top-down method) [33], or SiC graphene and epitaxial growth method (bottom-up). High-quality graphene is easily obtained in former method, which we use in our laboratory. Graphene with large area is obtained in latter method.

Micromechanical cleavage method

In this research, mono or multilayer graphenes were obtained by exfoliating the Kish graphite [114] by micromechanical cleavage method and transfered onto the substrate. The procedure is described below.

Silicon wafer topped with silicon dioxide (SiO_2) was used as substrate. The 285-nm-thick SiO_2 layer works as insulating layer. The Si layer was n-doped to be conducting ($0.001 \sim 0.0045\ \Omega\,\mathrm{cm}$), which would work as back gate electrode to apply electric field to graphene.

1. Wafer cut-out

   Manual scriber [115] was used to scribe the wafer surface with desired size. It must be scribed along the crystal plane of silicon. It was then cleaved by pushing from the back side.

   The final size of the substrates should be about 8 mm $\times$ 8 mm to mount it on the stage of the sample cell. In the beginning of the research, the substrate were cut to final size at this stage. There may be cracks in SiO_2 layer near the edge of the substrate (approximately 1 mm from the edge) and the insulation may be broken. So, the substrate was kept large at this stage and cut after transferring the graphene and locating, so that the graphene would be located at the center of the 8 mm-square-sized substrate(Fig. 57). This procedure reduces the probability of graphene to be located near the edge.

   Small shards of substrate may fall on graphene when the substrate is scribed with graphene on it. It was confirmed by optical microscope observation that shards remain very near the scribed lines and do not affect the area 1mm away.

2. Substrate cleaning

   Cut-out substrates were immersed in acetone and cleaned by ultrasonic cleaner [116] for 5 minutes, followed by ultrasonic cleaning in isopropanol for 5 minutes. Substrates were then dried by soft-baking in constant-temperature oven [117] at 110°C for 5 minutes.

   Next, piranha etching was done. Substrates were immersed in piranha solution, 1:1 mixture of sulfuric acid and hydrogen peroxide, for 15 minutes. Etched substrates

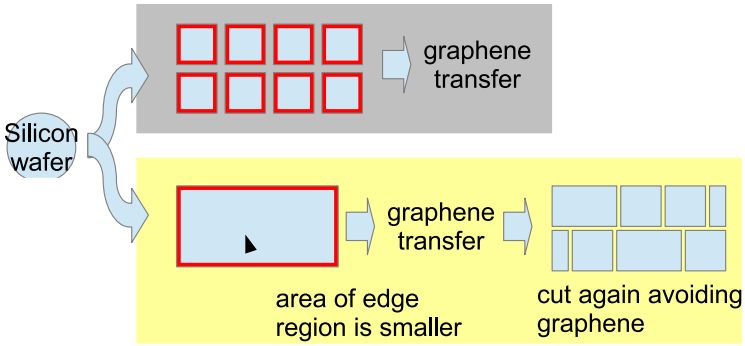

Fig. 57 Procedure of wafer cutting. Compared to cutting the substrates to final size at the beginning (above), it is more efficient to cut them after the transfer and locating of graphene (below).

were rinsed with water, followed by soft-baking in constant-temperature oven at 110°C for 5 minutes.

3. Cleavage of graphite and transfer to substrate

   Small amount of Kish graphite were put on sticky side of adhesive cellophane tape or dicing tape [118]. The tape were folded to put sticky side onto each other and then removed to cleave the graphite. This procedure was repeated until whole the surface is covered by graphite. Repeated cleavage makes the graphite thinner and thinner, reaching to graphene (micromechanical cleavage method). After that, sticky side of the tape was put on the substrate and attached firmly by pressing it using cotton-tipped stick, plastic tweezer, or rubber eraser. This makes part of the graphenes remain on the substrate (transfer, Fig. 58). Residual adhesive compound is reduced if the surface is covered by graphite.

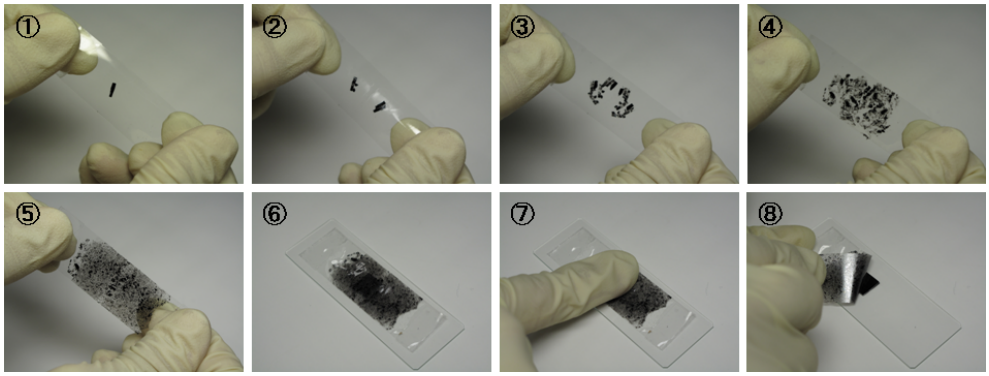

Fig. 58 Sample cleaving by micromechanical cleavage method and transferring to the substrate [119].

Normally, substrates are rinsed in acetone and isopropanol to remove the residual adhesive compound after the transfer. To avoid graphenes to be removed, ultrasonic

cleaning is limited to few seconds, or instead just immersed for several hours without ultrasonic cleaning. However, acetone and isopropanol may leave contaminants in liquid or in air on the surface when they evaporate. As surface-sensitive phenomenon are dealt with in this research, the cleaning was skipped. Effect of residual adhesive compound can be avoided as it is identified by optical microscope.

4. Locating graphene

   Whole the surface of the substrate were observed with digital optical microscope [120] to locate the transferred graphenes. The locations of the graphenes were recorded and photos were taken at the same time for subsequent layer number determination and electrodes fabrication.

   To avoid touching on the surface during the cleavage, scribed substrates were put on the concave side of plastic watch glass and then cleaved(Fig. 59).

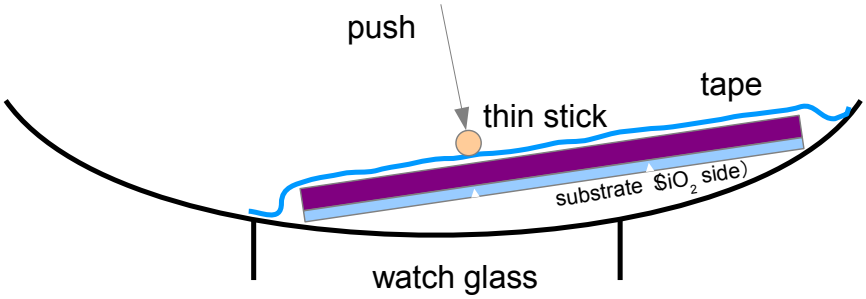

Fig. 59 Cleaving the substrate without touching the SiO_2 side.

Cleaning by vacuum annealing

Annealing is a common way for cleaning the sample. It is known that H_2O, NH_3, CO and NO_2 adsorbed on graphene would desorb by annealing in vacuum at 150˚C [101], while O_2 need higher temperature, 200˚C, to desorb [121]. Also, polymer residues on the surface would be removed by annealing in vacuum at 600˚C [122]. Fig. 60 is optical microscope images of SiO_2/Si substrate surface during the trial on removal of residual glue by annealing in vacuum of rotary pump in a furnace [83]. Adhesive tape is sticked on the substrate surface and then removed to leave the glue, which looks purple or light blue on SiO_2/Si surface. The glue was almost completely removed by annealing at 700˚C. If residual glue confusable with graphene is removed, it would be easier to locate the graphene.

Unfortunately, removal of residual glue by vacuum annealing was not suitable for this research, because graphene samples after the annealing were found to be so heavily hole-doped that Dirac peak could not be observed. This phenomenon is known as vacuum annealing effect [123, 124]. Annealing above 300˚C is reported to degrade the electrical properties of graphene [124]. Therefore, removal of residual glue by annealing was gave up and 200˚C was chosen as annealing temperature. Fig. 61 is gate voltage dependence of 2-terminal resistance of graphene before (black) and after (red) the annealing in vacuum of

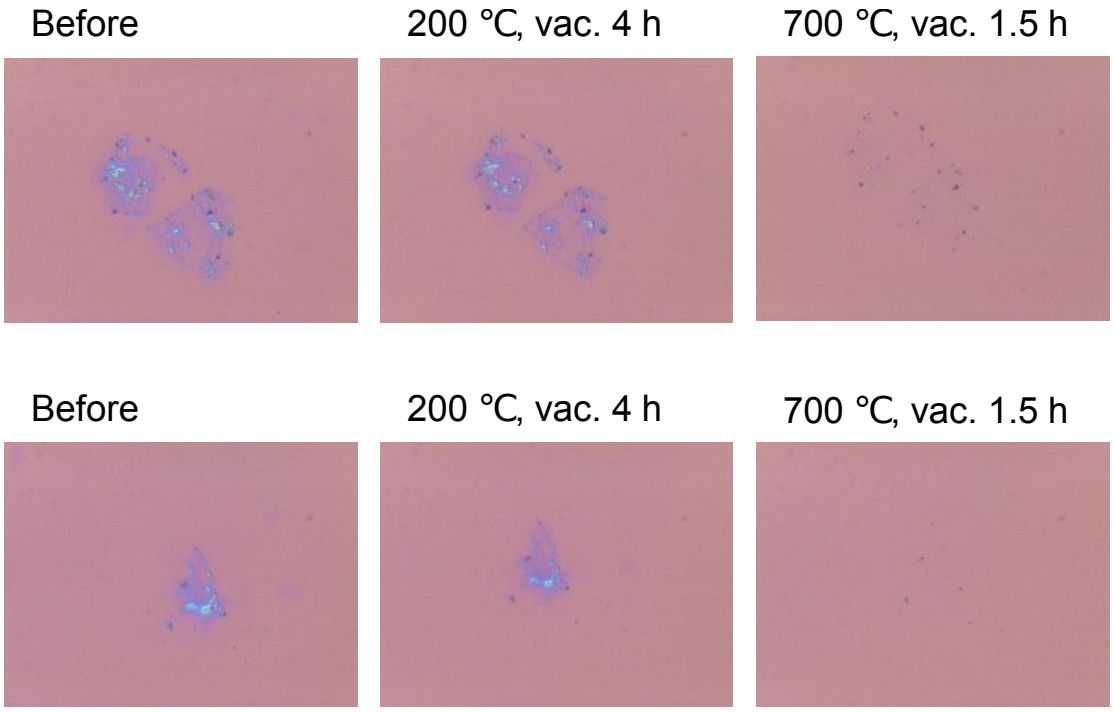

Fig. 60 Removal of residual glue on SiO_2/Si substrate surface by annealing in vacuum

rotary pump at 200°C for 3 h in a furnace [83]. Gate voltage at Dirac peak shifted from 20 V to 5 V, which indicates the reduction of hole doping by adsorbed oxygen. Also, width of the peak got narrower. Decrease in resistance at Dirac peak from 54 kΩ to 11 kΩ is including the decrease of contact resistance.

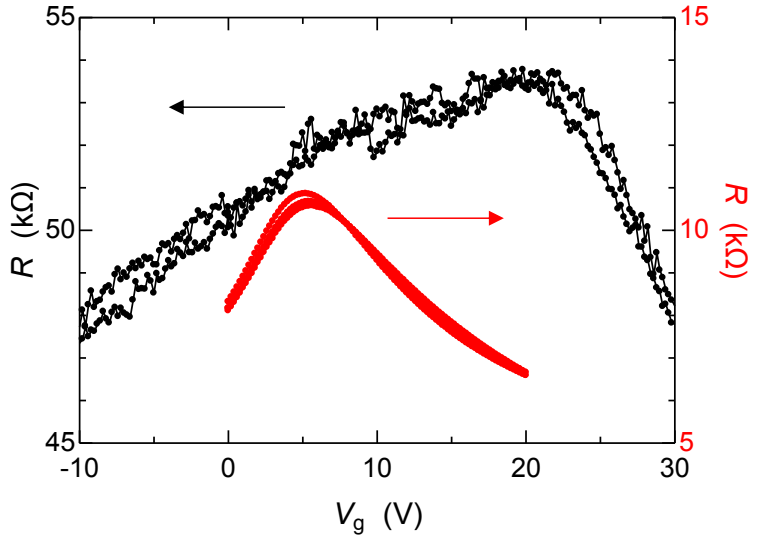

Fig. 61 Gate voltage dependence of 2-terminal resistance of graphene before (black) and after (red) the vacuum annealing at 200°C for 3 h.

Layer number determination of few layer graphite ① (optical method)

Visible light transmittance of graphene is about 98% [125]. Using optical microscope, reflected light from graphene transferred on SiO_2/Si substrate can be observed. Depending on the interference of lights, as air and graphene have different refractive indices, intensity of reflected light from the area with graphene differs from that from the area without graphene. This enables the determination of the layer number of graphene [126, 127].

Figure 62 shows the contrast difference depending on the thickness of SiO_2 layer and wavelength, extracted from a literature [126]. Substrates used in this research have 285-

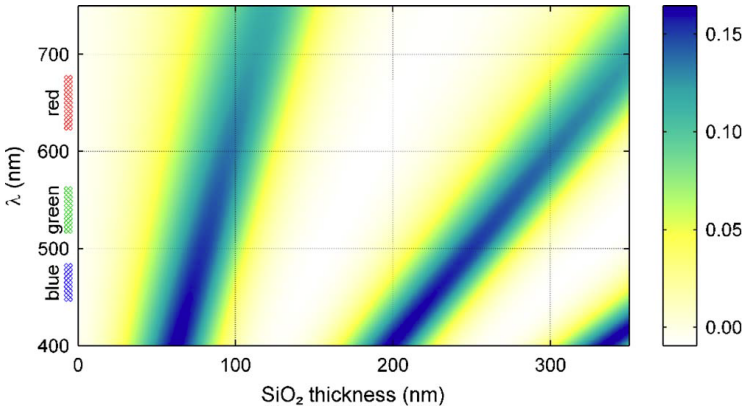

Fig. 62 Contrast difference depending on the thickness of SiO_2 layer and wavelength [126]. Color scale: C_{GS}.

nm-thick SiO_2 layer, which give the highest contrast for green light. Fig. 63 shows the snapshot during the color analyzation using the photo retouching software (Paint.NET). Distribution of RGB components within green frame in left hand side optical microscope

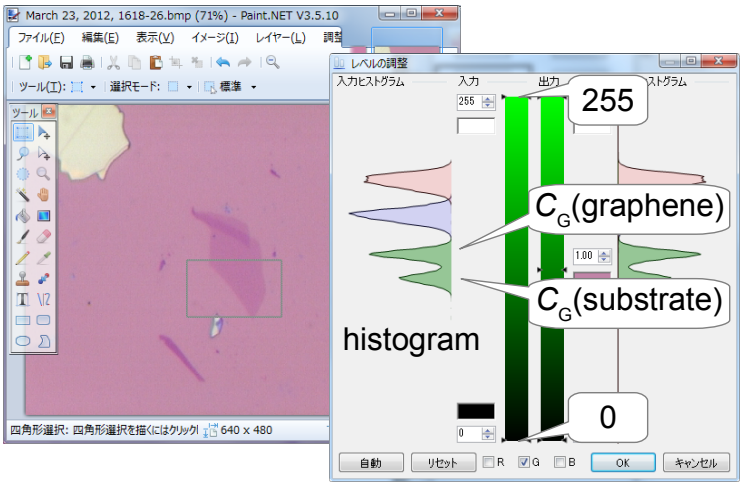

Fig. 63 Extraction of intensity of green component using photo retouching software.

image is shown in right hand side window. While R and B components have single peak, G

component indeed has 2 peaks. These correspond to the substrate area and the graphene area. This confirms that samples used in this research give highest contrast for green light.

Using this, to determine the layer number of graphene, contrast of green component of graphene area to the substrate area (without graphene) was defined as

$$C_{\mathrm{GS}} := \frac{(\text{G component of substrate}) - (\text{G component of graphene})}{(\text{G component of substrate})}. \tag{71}$$

Derived C_{GS} as above from G components of substrate and graphene shows histogram as 64 with descrete values corresponding to the layer numbers of graphenes.

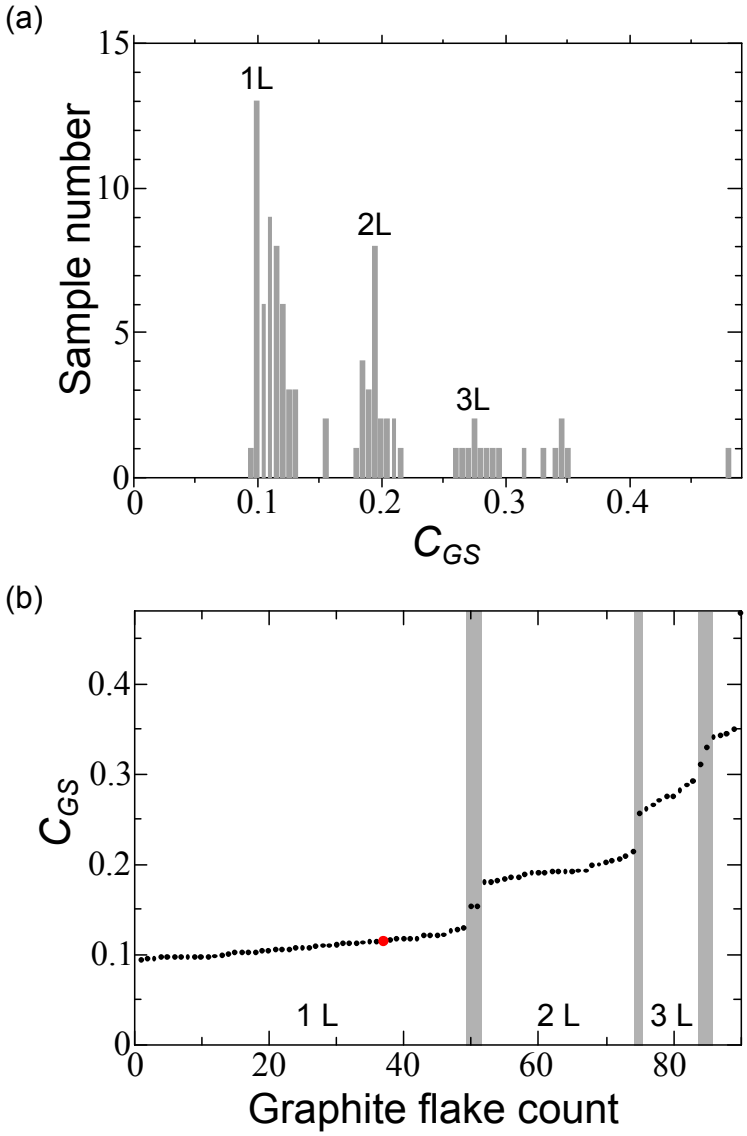

Fig. 64 Distribution of the contrast of graphenes obtained in our laboratory and estimation of the number of layers [128].

Mainly this method was used in this research to find monolayer or bilayer graphenes.

Layer number determination of few layer graphite ② (Raman spectroscopy)

Raman spectroscopy is optical spectroscopy using Raman scattering, which is inelastic scattering of light by electron-phonon interaction. Graphene with optically determined layer number with the method described in Section 3.2.1 was then examined by Raman spectroscopy [129] to confirm the layer number (Fig. 65). Ratio of the intensities of the G peak and G' peak is proportional to the layer number of graphene [130, 131]. Also, intensity of G peak is smaller than that of G' peak only if the graphene is monolayer. Not only layer number, it can also be used for evaluation of the quality of graphene. Intensity of D peak increases with an increase in density of disorders [132], because Raman process of D band is mediated by elastic intervalley scattering by disorder. Intensity of G' peak decreases with an increase in charge density reflecting the change in lattice constant [133], which can be used to determine the amount of charged impurities [134].

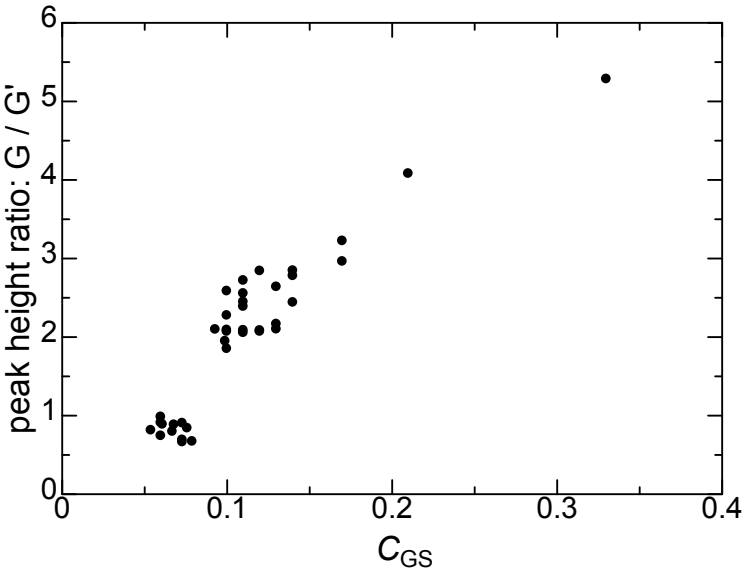

Fig. 65 Comparison between optical contrast C_{GS} and peak height ratio of raman spectroscopy G/G' for numbers of samples.

Layer number determination of few layer graphite ③ (transport property method)

Layer number can also be confirmed electrically using the gate voltage dependence of resistance after the fabrication of electrodes. Dirac peak, obtained by measuring the gate voltage dependence of resistance in vacuum at room temperature, changes its shape systematically depending on the layer number [36]. Using this, layer number was determined by comparing the shape of the Dirac peak with reference (Fig. 66) [36]. As the SiO_2 layer thickness of substrates used in Ref. [36] were 90 nm, the gate voltage values were multiplied by 285/90 to compare with our samples with 285 nm-thick SiO_2 layer.

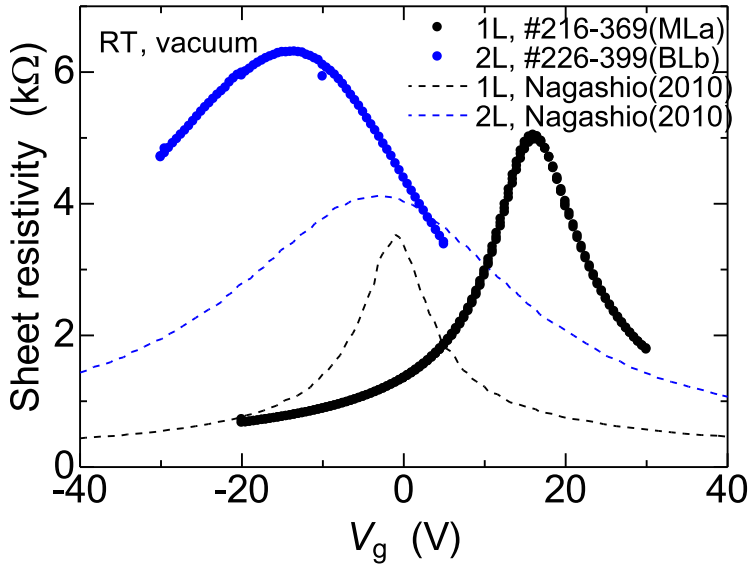

Fig. 66 Layer number confirmation by gate voltage dependence of resistance. Black and blue data points are for monolayer and bilayer graphene samples, respectively, measured in this research. Dashed lines are reference data [36], corrected considering the difference of the thickness of SiO_2 layer.

3.2.2. Electrodes fabrication

To perform the four-terminal transport measurements of exfoliated graphene samples, two different fabrication methods were employed in this work. One is the common photolithography method used in the early stage of the work, and the other is the indium microsoldering method [135]. Since alignment of small graphene samples with the mask aligner in our laboratory, whose magnification is not high enough, was difficult in the former method, most of the transport measurements were carried out by the latter method. Also, possible residual resist on graphene sample after the wet process in the lithography technique is unfavorable for gas adsorption experiments to try to create band gap in graphene. On the other hand, the microsoldering method is essentially a dry process where the electrodes are directly attached to the graphene sample in inert gas atmosphere. We first describe the photolithography technique and then the microsoldering one in the following.

Microsoldering method

Microsoldering method for graphene was proposed and established by Girit *et al.* in 2007 (Fig. 67) [136]. Indium is melted to form a thin needle on a tungsten tip and then attached directly onto the sample. Contrary to conventional fabrication methods, the sample surface is kept free from resist or evaporated films commonly used in the lithography process as it was synthesized and electrodes can be fabricated without contamination.

The microsoldering method requires a sample holder that can heat the substrate and

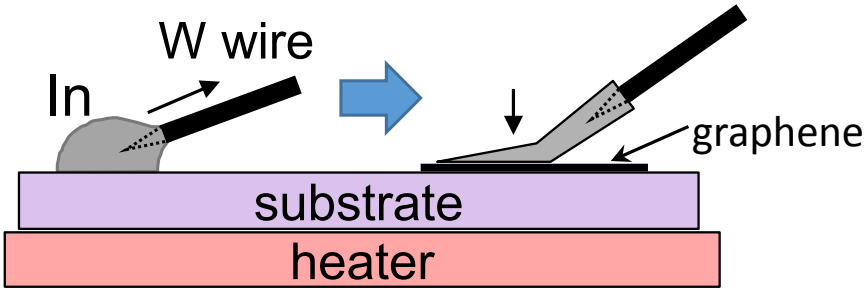

Fig. 67 Schematic overview of Microsoldering method.

mechanism to manipulate the position of the indium needle precisely. For this, we made an instrument shown in Fig. 68. Two arms with tungsten tips are connected to XYZ stages and approach to the stage of the optical microscope [120] from right and left. The tips are electrolytically polished sharp tungsten wires of 0.3 mm diameter. Fig. 69 is a close looking of the microscope stage. Two individual ceramic heaters (allowable input: 100 V, 100 W) are placed underneath the sample holder; one is to melt indium beads and the other is to heat the sample substrate. The heaters are powered through variable transformer to enable temperature control by voltage. Figure 70 shows the achieving temperature versus voltage. The temperature was measured by thermocouple pressed onto the substrate on the heater. Considering the insufficient contact between thermocouple and the heater, actual substrate temperature might be higher than this. As a matter of fact, when 38 V was applied, the substrate do not exceed the melting point on indium 156˚C according to Fig. 70, while indium on the substrate actually melted.

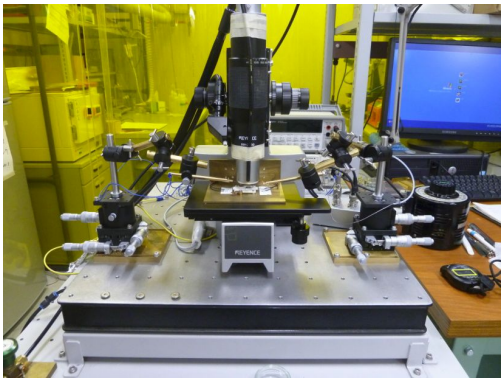

Fig. 68 Whole image of Microsoldering instrument

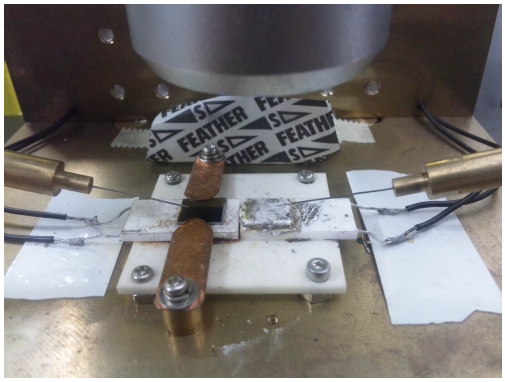

Fig. 69 Around the sample substrate

Procedure of electrode fabrication by Microsoldering method is described below. Empirically, sharp indium needle was rarely formed when thick oxide layer was formed on the surface of the indium. Also, oxide layer is supposed to degrade the contact. Although in the original paper of microsoldering no inert or forming gas was used, it was reported that indium melted in air shows poor wetting angle on Au/Ti-deposited Si surface [137]. To avoid the oxidation, surface of the indium wire was polished and the wire was stored in

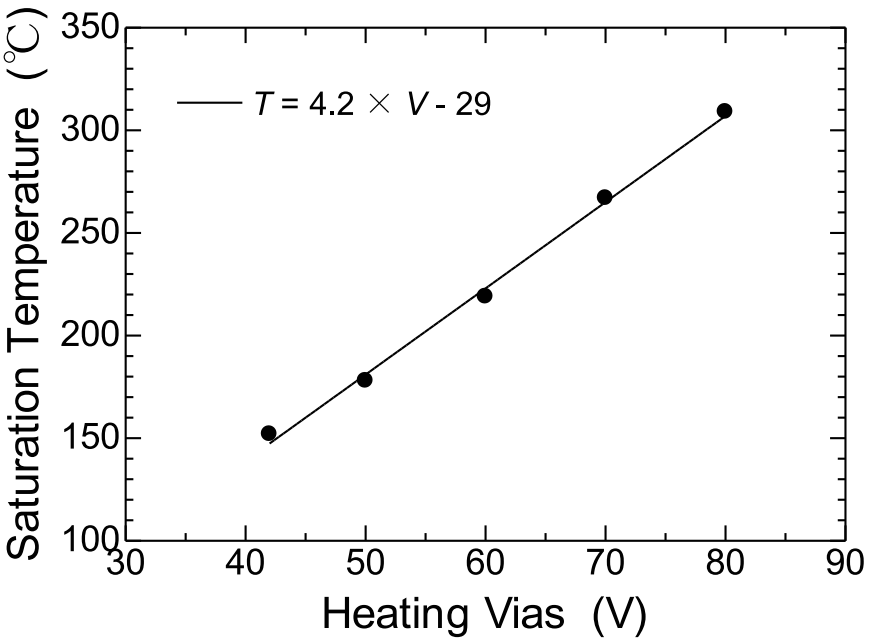

Fig. 70 Relation between the sample holder temperature and the applied voltage to the heater under the holder. The temperature was measured by pressing the thermocouple on the substrate and actual temperature might be higher. Solid line in the plot is linear fitting of the data.

acetone until just before the use. In later phase of research, whole the instrument was put in a big plastic bag and inert argon gas was filled. Nitrogen gas could not be used because it reacts with indium to form InN [138].

1. Indium needle formation

   99.99% Indium [139] was melted by applying 38 V to the heater for indium melting. It started melting by 2∼3 minutes of heating from room temperature. Tungsten needle was inserted into the molten indium and then slowly pulled out, which comes with solidified indium fixed on the tip of the tungsten needle. Sharp needle can be formed by optimizing the temperature and speed. The tip of the indium needle was observed by optical microscope to see if it is thin enough compared to the sample. To enhance the operation efficiency, it is better to prepare number of indium needles at this time.

2. Attaching electrodes to the sample

   Sample substrate was heated by applying 38 V to the heater for sample substrate heating. The temperature would be appropriate by 2 minutes of heating from room temperature. Indium needle was positioned above the sample and approached to it under the optical microscope. Indium touched to the sample or substrate would melt and remain in that position. Once the indium on the substrate reached to sufficient length, the tungsten needle was pulled up to cut the indium. This procedure was repeated until required numbers of electrodes are placed. Then, the heater was

switched off to naturally cool the sample substrate. The indium would solidify and fixed on the sample.

In situ conduction test between the indium electrodes and the sample is possible by touching two different indium electrodes with two tungsten needles and measure the resistance through the needles.

3. Anneal

To improve the electrical contact between the sample and indium, the sample was annealed. After attaching the electrodes, 82 V was applied to the heater and the sample substrate was heated for 2 minutes. To avoid thermal damage to the objective lens, the lens tube was disengaged beforehand. Finally, the heater was switched off, and the sample substrate was naturally cooled.

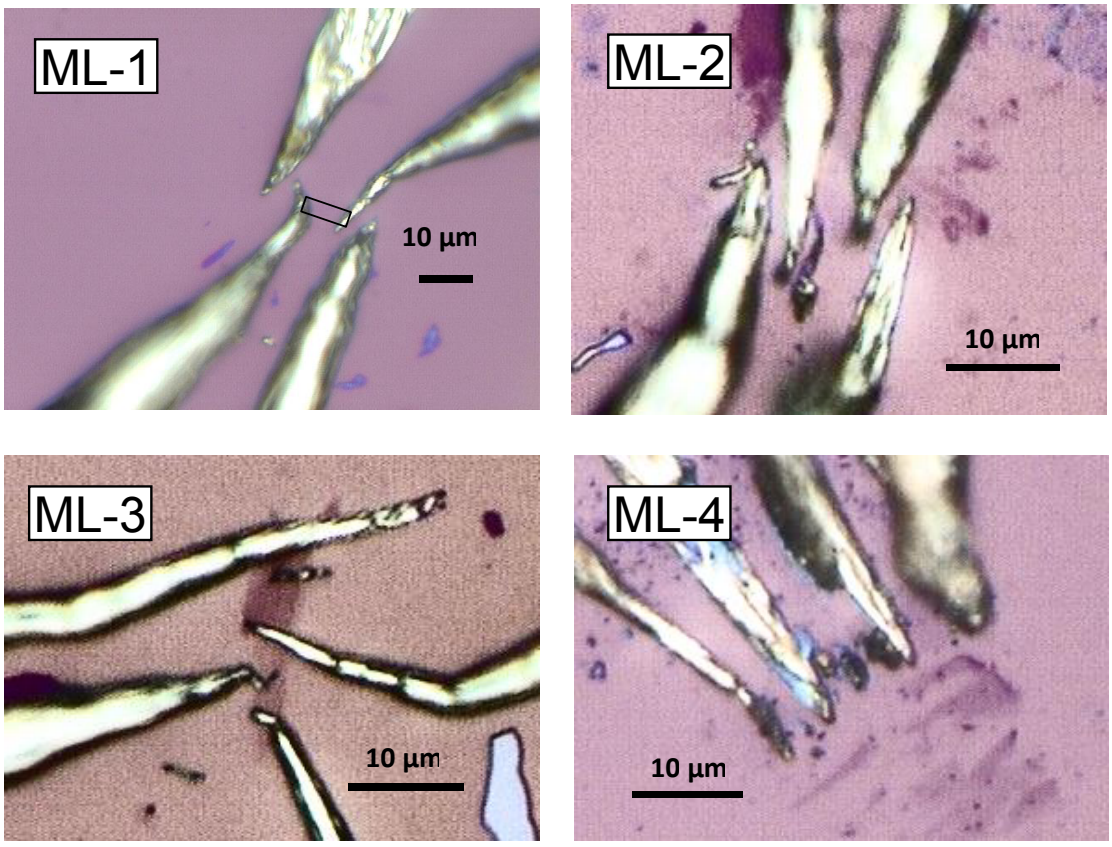

Fig. 71 Optical microscope images of graphene samples used in O_2 adsorption experiments. Contrasts of the images are modified to increase the visibility of the graphene. The electrodes were fabricated with indium microsoldering method.

3.2.3. Measuring system

Sample cell and cryostat

Figure 72 is the appearance and cross-section drawing of the sample cell used in this research. It was originally designed and used for the experiment of gas adsorption with precisely controlled areal density on the sample. Detail of the cell, especially about the Grafoil stack, will be described in Section 4.2.

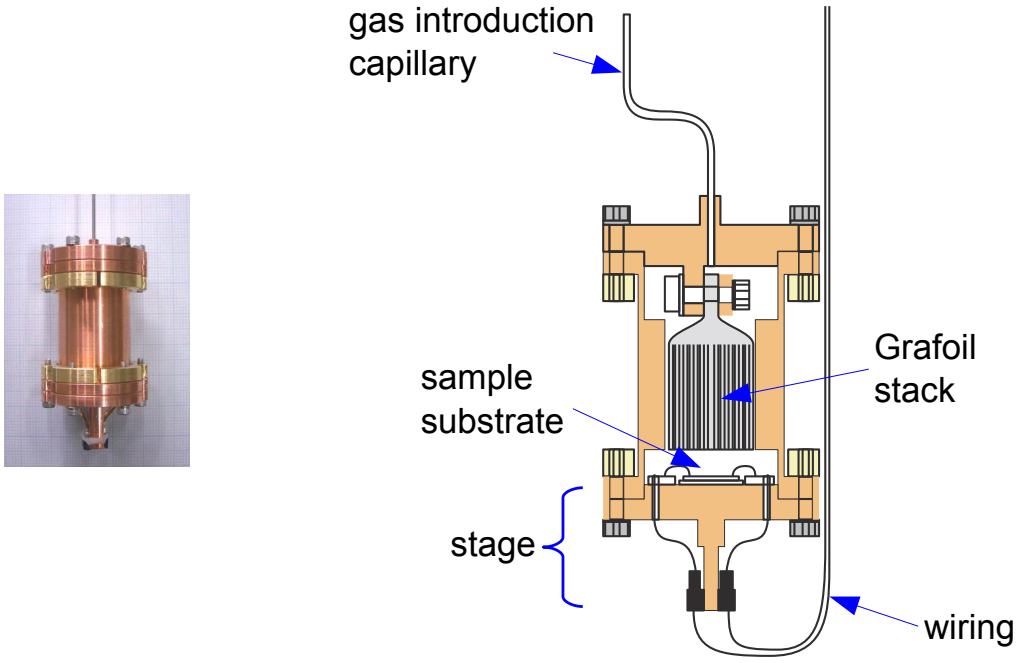

Fig. 72 Appearance (left) and cross-section (right) of the sample cell.

Cernox resistance thermometer and heater for temperature control was attached to the sample cell. The cell was mounted on the cryostat to enable the cooling with cryogen (Fig. 73).

Sample substrate was bonded on an oval-shaped copper plate with air drying silver paste [140]. The plate was screwed onto the stage. The plate was insulated from the stage by putting the Kapton tape on the stage where the plate touches, and also insulating washer made of Teflon sheet. Then, electrodes on the stage and indium electrodes on the sample substrate were wired. Wire bonder is commonly used, but bonding on the indium electrode was not successful. In this research, the electrodes were connected by gold wire using air drying silver paste under the stereoscopic microscope by hand. Figure 74 is the wired sample substrate on the stage.

Gas handling system

Gas handling system (Fig. 75) was used to control the amount and pressure of gas introduced to the sample cell. Two standard volumes SV1, SV2 with known inner volumes,

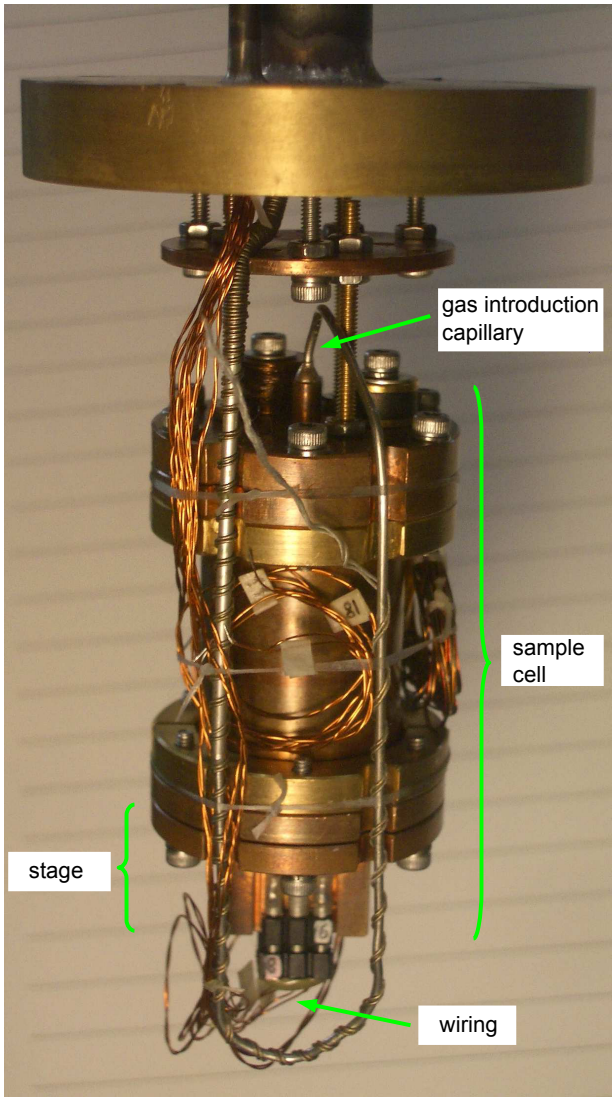

Fig. 73 Sample cell mounted on the cryostat.

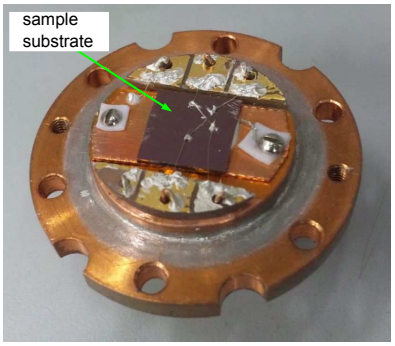

Fig. 74 Sample substrate fixed on the stage and wired.

with their own thermometer [143] attached, are equipped. Also, piezoresistive pressure gauge [144] witch can be used from vacuum to atmospheric pressure is equipped. Introduced gas from four lines can be measured by these equipments and introduce to the sample cell.

Transport measuring system

Transport properties measurement of graphene was performed by lock-in amplifiers [90] with current-driven lock-in measurement (Fig. 76). Same circuit as buckypaper measurements (Section 2.2.3) was used for the measurements of graphene. The voltage applied to the back gate was controlled by a SourceMeter [145].

Measurements were controlled by a computer. Gate voltage sweeping, measurement with temperature variation, etc. were realized by the program built on LabVIEW 2010 or 2012.

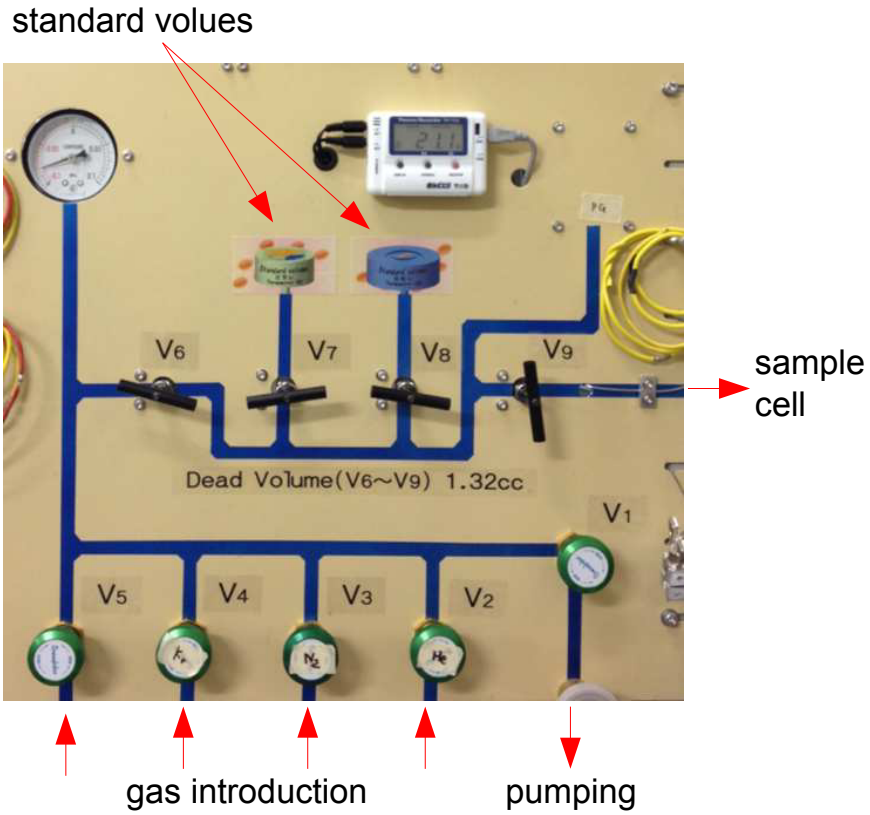

Fig. 75 Photo of the front panel of the homemade gas handling system (Ref. [141, 142]).

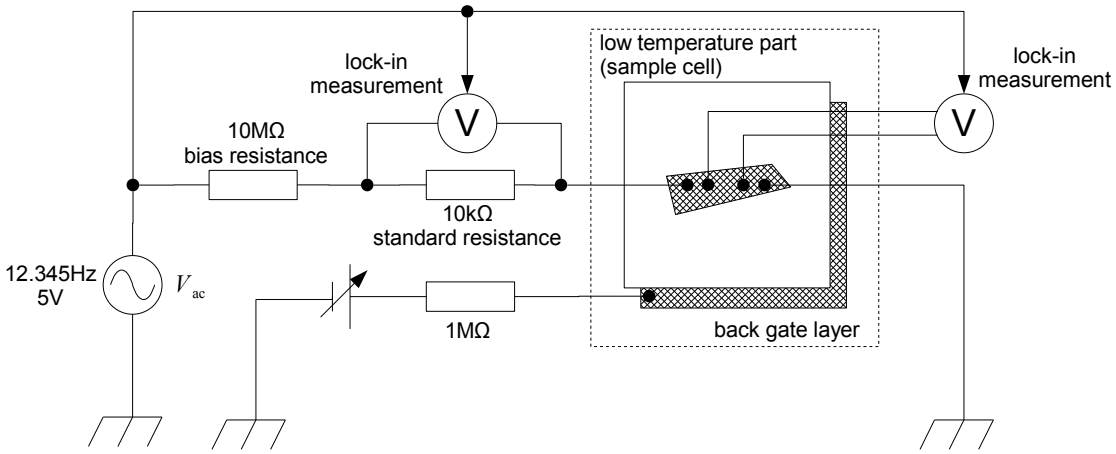

Fig. 76 Circuit of transport measurement system.

3.3. Results and discussion

3.3.1. O_2 adsorption of monolayer graphene at room temperature

Optical microscope images of exfoliated monolayer graphene samples (ML-1, ML-2, ML-3 and ML-4) used in the O_2 adsorption experiments are shown in Fig. 71. Four electrodes were fabricated on each graphene sample by the indium microsoldering method. The width and length of each sample obtained from optical microscope image is in Table 6.

Table 6 Approximate sample width and length of measurement area for each graphene sample obtained from optical microscope image

sample	width (μm)	length (μm)
ML-1	2.5	8.8
ML-2	3.2	4.6
ML-3	3.7	3.2
ML-4	4.2	7.5

ML-1, ML-2 and ML-3 were exposed to oxygen gas at 303 $\pm$ 0.01 K regulated by the heater (hereafter, room temperature or R.T.). Conditions of the O_2 exposure are summarized in Table 7. For better time resolution of data taking, the gate voltage (V_g) was swept up and down with a speed of 0.2 V/s continuously within 0.3 min.–12 h after changing the O_2 pressure abruptly, and then switched to intermissive sweep with the same speed by resting for 10 s–1 h between the successive sweep cycles (Fig. 77). It is known that the hole doping efficiency slightly depends on V_g [110]. Therefore, it should be noted that what we measured in this experiment is a sort of average doping speed at $V_{min} < V_g < V_{max}$. The gas pressures in this experiment are much lower than those ($\approx$ 1 atm) in the previous experiments [146, 110], which slowed down the reaction between O_2 and graphene and allowed us to follow the fast doping process [147, 148] after the abrupt change of the pressure.

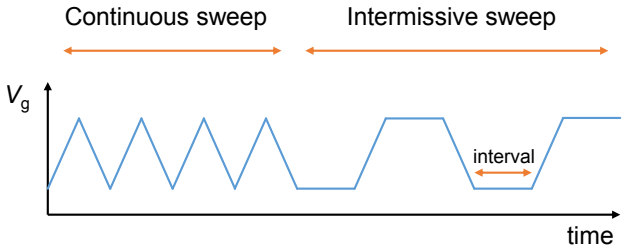

Fig. 77 Sequence of gate voltage sweep

Gate voltage vs. resistance data taken during the O_2 adsorption are shown in Fig. 78. All of them showed large positive shifts of the peak voltage at the Dirac point (V_g^{DP}; denoted by red circles in the figure) indicating hole doping to graphene.

Figure 79 describes how to characterize the Dirac peak and its shift. The shift of gate voltage at the Dirac peak $\Delta V_g^{DP} \equiv V_g^{DP}(t) - V_g^{DP}(0)$ corresponds to the amount of hole

Table 7 O_2 exposure and measuring conditions. Interval is a time interval between the two successive sweeps. During the sweep was stopped, V_g was kept alternately at V_{min} and V_{max}.

Sample	Run No.	Pre-cleaning	O_2 pressure (Pa)	Gate voltage sweeping time duration	interval	range
ML-1	1	∼100°C, pumping 11 h	422	0∼364 m ∼66 h	0 1 h	0↔ 20 V
ML-2	1	∼100°C, pumping 11 h	426	0∼166 m ∼390 m ∼150 h	0 10 m 1 h	−10 ↔ 10 V
	2	∼100°C, pumping 11 h	464	0∼22 m ∼144 h	0 1 h	−10 ↔ 10 V
	3	∼100°C, pumping 11 h	426	0∼68 m ∼94 h	0 1 h	−10 ↔ 10 V
ML-3	1	∼100°C, pumping 11 h → N_2 adsorption → RT, pumping 114 h	626	0∼12 h ∼41 h ∼51 h	0 10 s 30 s	20 ↔ 40 V

doping. A change in the resistance peak $\Delta R^{DP} \equiv R^{DP}(t) - R^{DP}(0)$ is related to increase of carrier scatterings caused by disorders caused by the O_2 adsorption. $\Delta R \equiv R^{DP} - R^{DP\pm 5V}$ is a quantity that represents the sharpness of the peak relating to the mobility. Larger ΔR means sharper peak and therefore higher mobility.

Time evolutions of the above defined parameters during the adsorption are shown in Fig. 80.

Table 8 Parameters obtained from fitting the $V_g^{DP}(t)$ data to the double-exponential function (Eq. (72)) for ML graphene samples.

Sample	Run No.	$V_g^{DP}(0)$ (V)	a_1 (V)	τ_1 (h)	a_2 (V)	τ_2 (h)
ML-1	1	11.7	1.48	0.790	8.41	33.3
ML-2	1	10.1	0.994	2.03	14.6	42.5
	2	3.80×10^3	0.754	0.869	3.80×10^3	2.06×10^5
	3	3.41	0.640	3.63	3.73	170
ML-3	1	34.9	2.38	0.745	5.08	20.2

Fittings to the double exponential function is shown in Fig. 82 in semi-log plot. Fitting parameters for double exponential function is summarized in Table 9. Almost all the data cannot be fitted by a simple function, suggesting the existence of multiple mechanisms.

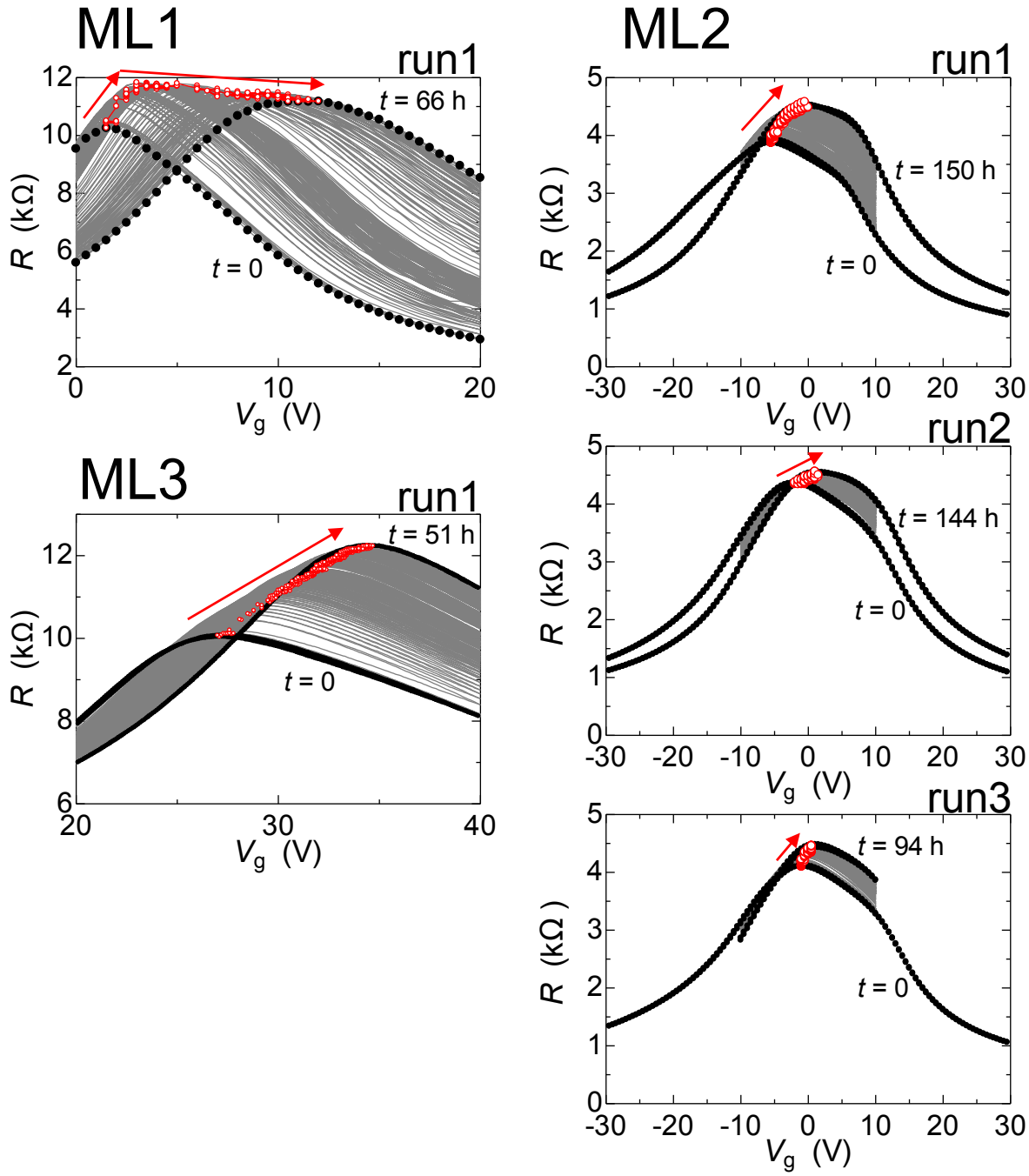

Fig. 78 Time evolutions of V_g vs. R data during the O_2 adsorption for the three monolayer graphene samples, ML-1, ML-2 and ML-3. Only for the first and last sweeps, actual data are plotted by the black points, and other sweeps are shown by the thin gray lines. The red open circles are maxima of the resistance, corresponding to the Dirac points.

The global shapes can be reproduced by the double-exponential function:

$$X(t) = X(0) - a_1 \exp(-t/\tau_1) - a_2 \exp(-t/\tau_2) \tag{72}$$

(73)

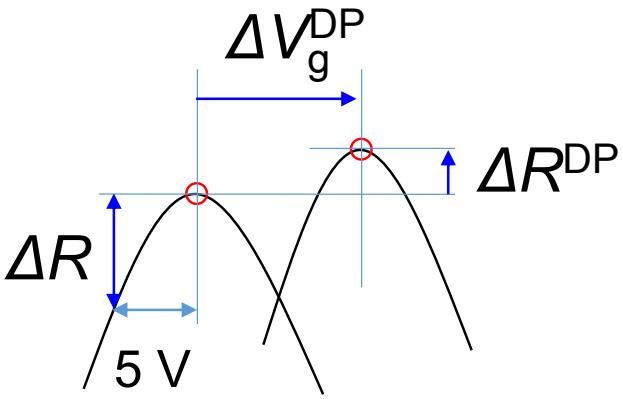

Fig. 79 Characterization of a Dirac peak and its shift

Table 9 Parameters obtained from fitting the $R_{\rm DP}(t)$ data to the double-exponential function (Eq. (72)) for ML graphene samples.

sample	run	R_0 (kΩ)	a_1 (kΩ)	τ_1 (h)	a_2 (kΩ)	τ_2 (h)
ML-1	1	11.3	1.34	0.354	0.489	26.8
ML-2	1	4.60	0.187	4.30	0.460	82.7
	2	6.12	9.57×10^{-3}	7.72×10^{-4}	1.76	2.06×10^3
	3	4.46	0.160	0.730	0.195	33.5
ML-3	1	12.3	0.813	0.483	1.35	13.2

where $X = V_{\rm g}^{\rm DP}$ or $R^{\rm DP}$, except the Run-2 of ML-2 sample, where $V_{\rm g}^{\rm DP}$ and $R^{\rm DP}$ follow linear time dependences after the initial exponential behavior. Two time constants are in range of 0.8 h $\leq \tau_1 \leq$ 4 h and $\tau_2 \geq$ 30 h. Jaaniso *et al.* [111] observed also the double-exponential time evolution of the conductance by exposing monolayer graphene to O_2 gas of 426 Pa without applying $V_{\rm g}$. Their τ_1 and τ_2 are 11 s and 260 s, respectively, which are much shorter than our time constants. We did not measure the sample resistance in such a short time scale less than 120 s in our experiment. Also, Jaaniso *et al.* did not measure the conductance in such a long time scale than 500 s. Therefore we cannot compare the results by the two groups directly.

The two step process of time evolution of resistance may be explained by portal site mediated adsorption and spillover mechanism. In this model, active sites on the surface with lower adsorption energies work as portals. Assuming that adsorbents are mobile on the surface, spillover occurs and the adsorbents diffuse to the rest of the surface. The model has previously been used to explain O_2 adsorption on catalyst particle/surface system [149]. Defects like vacancies or edges of graphene may work as the portal sites. If oxygen molecular species adsorbed on portal sites and on the rest of the surface affect the resistance differently and independently, the model can be used to explain the double step behavior; resistance change with shorter time constant is attributed to the adsorption on portal sites and change

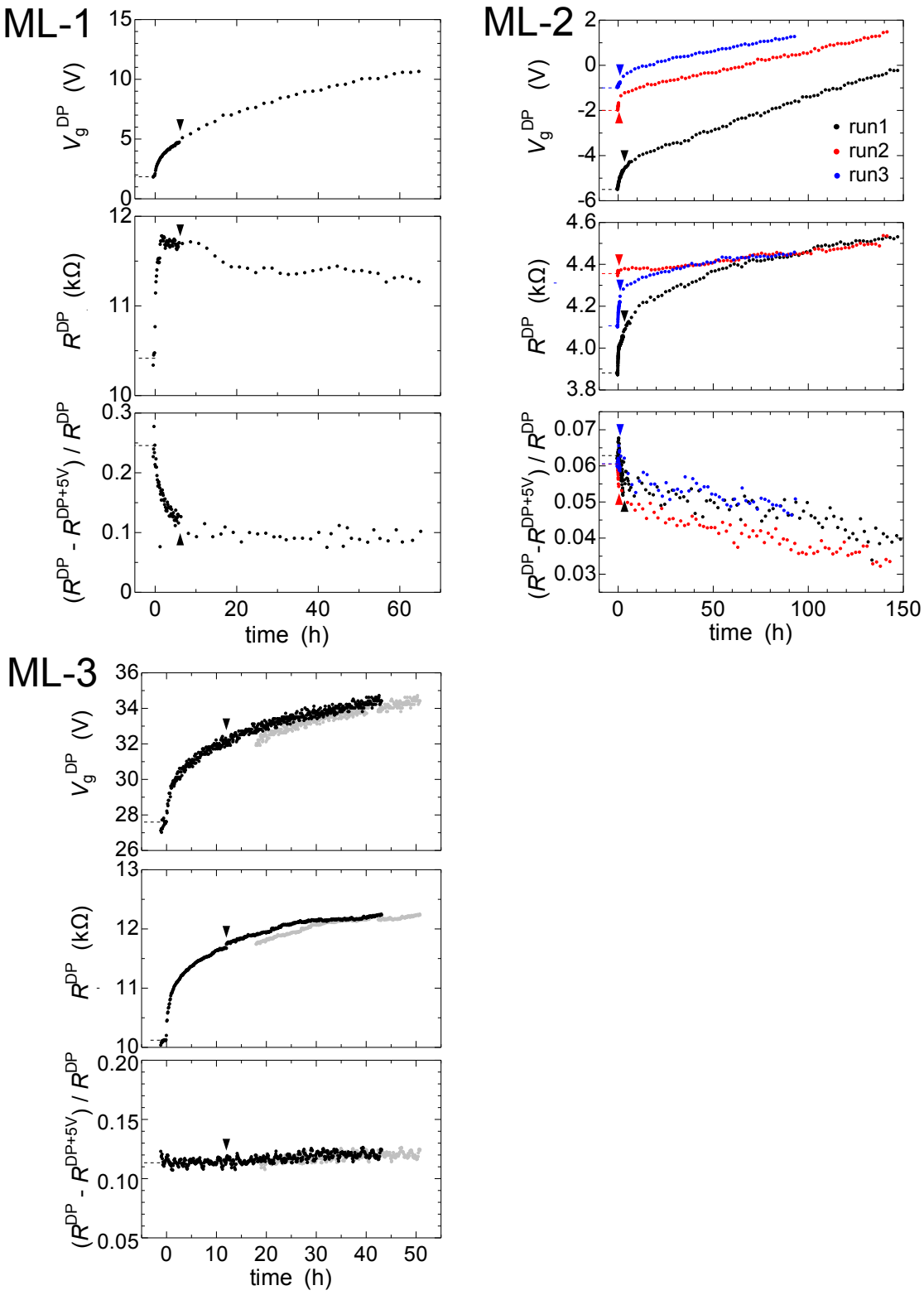

Fig. 80 Time evolutions of the gate voltage at the Dirac point $V_{\rm g}^{\rm DP}$, resistance at the Dirac point $R^{\rm DP}$ and resistance drop ratio at 5 V away from the Dirac peak $[R^{\rm DP} - R(V_{\rm g}^{\rm DP} + 5V)]/R^{\rm DP}$, which corresponds to the sharpness of the peak. The gray color points in the data of $V_{\rm g}^{\rm DP}$ and $R^{\rm DP}$ for ML-3 are raw data before being corrected for the accidental keeping of $V_{\rm g}$ at 20.7 V for $12.1 \leq t \leq 18.0$ h without sweep (see the main text). Triangles are when the $V_{\rm g}$ sweeps were switched from the continuous to intermissive mode (see the main text).

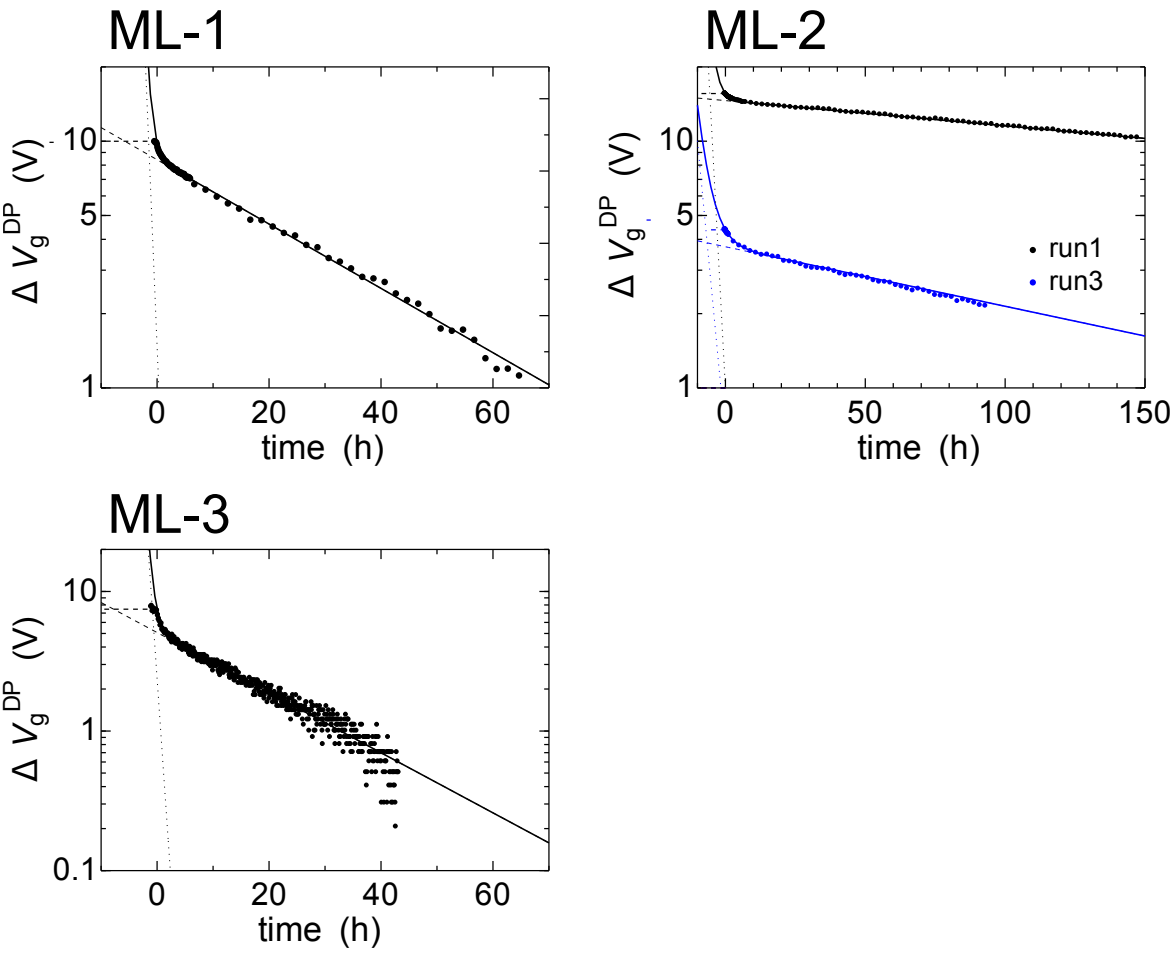

Fig. 81 Semi-logarithmic plot of $V_{\mathrm{g}}^{\mathrm{DP}}$ vs. time for the ML-1, ML-2 and ML-3 samples. The solid lines are double exponential function fittings to Eq. (72).

with longer time constant is attributed to the adsorption on the rest of the surface.

For the sample ML-2, the pumping-absorption procedure was repeated for three times (runs) on the same sample. The parameters $V_{\mathrm{g}}^{\mathrm{DP}}$, R^{DP} and ΔR did not recovered to the initial values after pumping at ∼100°C, indicating that the process of causing these parameter changes is irreversible at 100°C. In particular , the value of $V_{\mathrm{g}}^{\mathrm{DP}}$ before adsorption monotonically increased with each pumping-adsorption procedure. Also, the amount of change after the start of adsorption decreased with each repetition. From this, it is considered that the changes include the process of chemisorption to the sites where the desorption energy is larger (not desorbed at 100°C). On the other hand, some part of the changes are reproduced even after repeating the pumping-adsorption procedure. It seems to be due to chemisorption to the sites with small desorption energy. In our experiments, it is impossible to heat the sample to a temperature higher than the melting point (156°C) of indium used for the electrodes, but in the previous study it is reported that the change due to oxygen adsorption is completely recovered by pumping at 200°C.

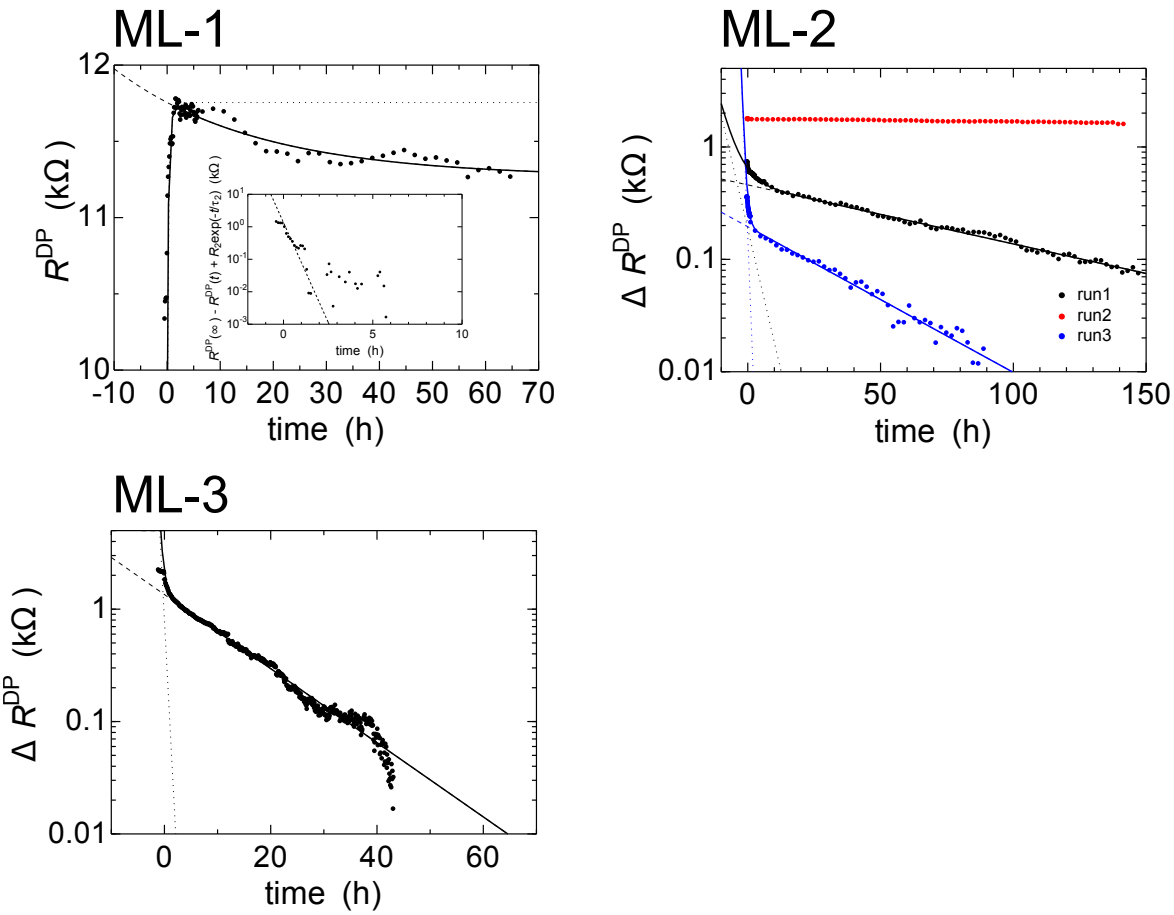

Fig. 82 Semi-logarithmic plot of ΔR^{DP} vs. time for the ML-1, ML-2 and ML-3 samples. The solid lines are double exponential function fittings.

It is noted that from $t = 12.1$ h to 18.0 h in the measurement for ML-3, the gate voltage sweeping was accidentally paused and kept at $V_{\mathrm{g}} = 20.7$ V which is the lowest bound of the sweeping range. During this period the speed of change of ΔV_{g} and R^{DP} slowed down with small discontinuous drops, indicating that the adsorption reaction rate is slightly higher for higher V_{g} as was reported previously for bilayer graphene [110]. Such small discontinuities can easily be connected.

Sato *et al.* claimed that the time evolution of $V_{\mathrm{g}}^{\mathrm{DP}}$ obeys power-law [110]. Following them, we also confirmed whether we can explain the time evolution of $V_{\mathrm{g}}^{\mathrm{DP}}$ by the power-law. Figure 83 is log-log plot of temporal change in $V_{\mathrm{g}}^{\mathrm{DP}}$ for ML-1, ML-2 and ML-3. The change in $V_{\mathrm{g}}^{\mathrm{DP}}$ roughly obeyed power law, but the detail of the behavior were reproduced well by the double exponential function fittings. Sato *et al.* used oxygen atmosphere of 1 atm [110], but in our case we used oxygen atmosphere with lower pressure, so there is a possibility that the process with shorter time constant could be more clearly observed.

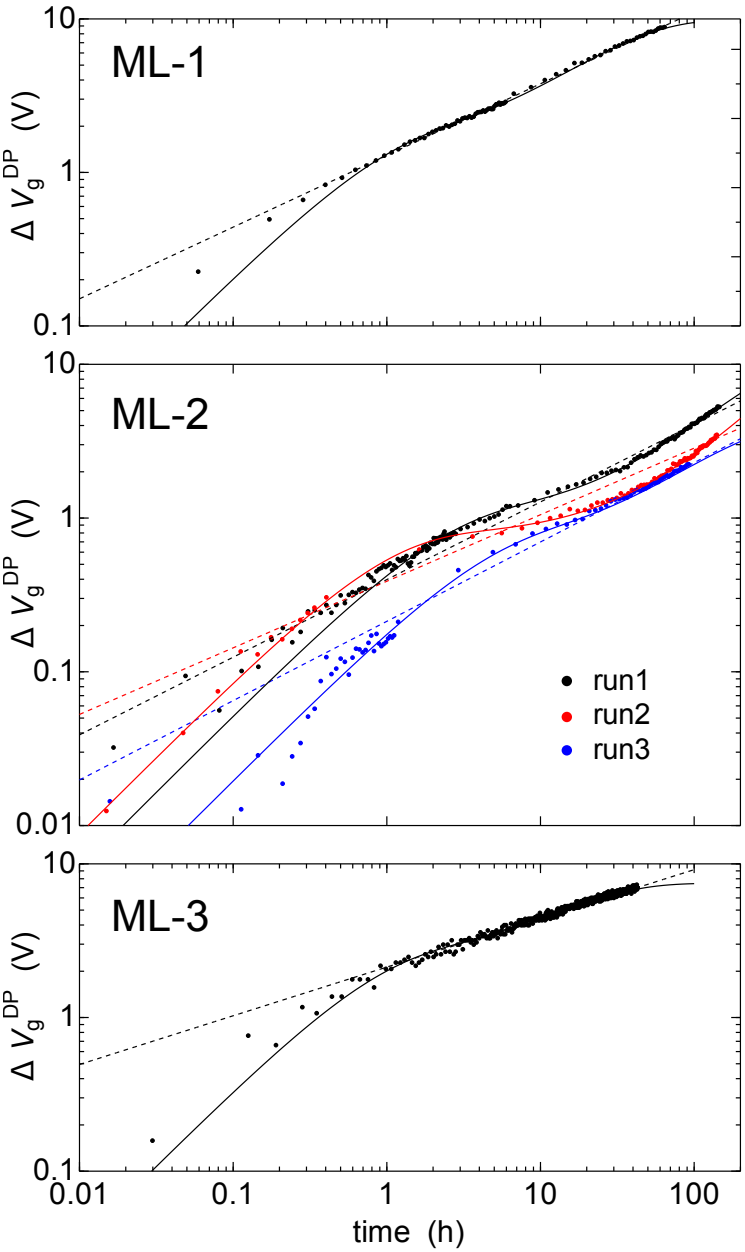

Fig. 83 Log-log plot of time evolutions of V_g^{DP} for ML-1, ML-2 and ML-3 samples. The solid lines are double-exponential fittings and the dashed lines are power-law fittings.

3.3.2. Results on bilayer graphene

Bilayer graphene sample BL-1 was exposed to oxygen gas at RT. Conditions of the O_2 exposure are summarized in Table 10. For BL-1, intermissive sweep was used for whole of

Table 10 O_2 exposure and measuring conditions. Interval is a time interval between the two successive sweeps. During the sweep was stopped, V_g was kept alternately at V_{min} and V_{max}.

Sample	Run No.	Pre-cleaning	O_2 pressure (Pa)	Gate voltage sweeping time duration	interval	range
BL-1	1	∼100℃, pumping 21 h	374	0∼26 h	—	0 ↔ 50 V
	2	∼100℃, pumping 18 h	416	0∼22 h	10 m	0 ↔ 50 V
	3	∼100℃, pumping 70 h	225	0∼45 h	10 m	0 ↔ 50 V
	4	RT, pumping 25 h → ∼100℃, pumping 6 h	493	0∼54 h	10 m	0 ↔ 50 V
	5	∼100℃, pumping 17 h	485	0∼42 h ∼62 h	1 h	0 ↔ 60 V 0 ↔ 65 V

the measurement sequence.

Gate voltage vs. resistance data taken during the O_2 adsorption are shown in Fig. 84. All of them showed large positive shifts of the V_g^{DP} indicating hole doping to graphene.

Time evolutions of the parameters during the adsorption are shown in Fig. 85. The most obvious difference between monolayer graphene samples and bilayer graphene sample is the amount of the shift in V_g^{DP}. While the amount of the shift in the monolayer samples were limited up to ∼8 V even after the adsorption over 100 h, the shift in the bilayer sample exceeded 20 V within 20 h and exceeded 50 V after the repeated adsorption. The doped carrier (hole) density is estimated to be $\sim 4 \times 10^{12}$ cm^{-2} using the thickness of the insulating SiO_2 layer, 285 nm, and relative permittivity of SiO_2, 3.8. The large amount of shift up to ∼60 V have also been reported by Sato *et al.* for bilayer graphene [110]. This means that the amount of hole doping per unit time is distinctively larger in bilayer sample.

Fittings of V_g^{DP} to the double exponential function is shown in Fig. 86. The parameters obtained from the fitting is summarized in Table 11. Compared to ML samples, both of

Table 11 Parameters obtained from fitting the $V_g^{DP}(t)$ data to the double-exponential function (Eq. (72)) for BL graphene samples.

Sample	Run No.	$V_g^{DP}(0)$ (V)	a_1 (V)	τ_1 (h)	a_2 (V)	τ_2 (h)
BL-1	1	51.6	11.4	0.855	27.7	50.5
	2	45.7	12.2	0.358	15.6	14.4
	3	49.6	7.37	0.629	18.2	36.2
	4	56.1	2.39	0.667	12.2	58.4
	5	3.06×10^4	5.22	1.73	3.05×10^4	1.52×10^5

the two coefficients (a_1, a_2) are indeed larger. Also, the two time constants (τ_1, τ_2) are shorter.

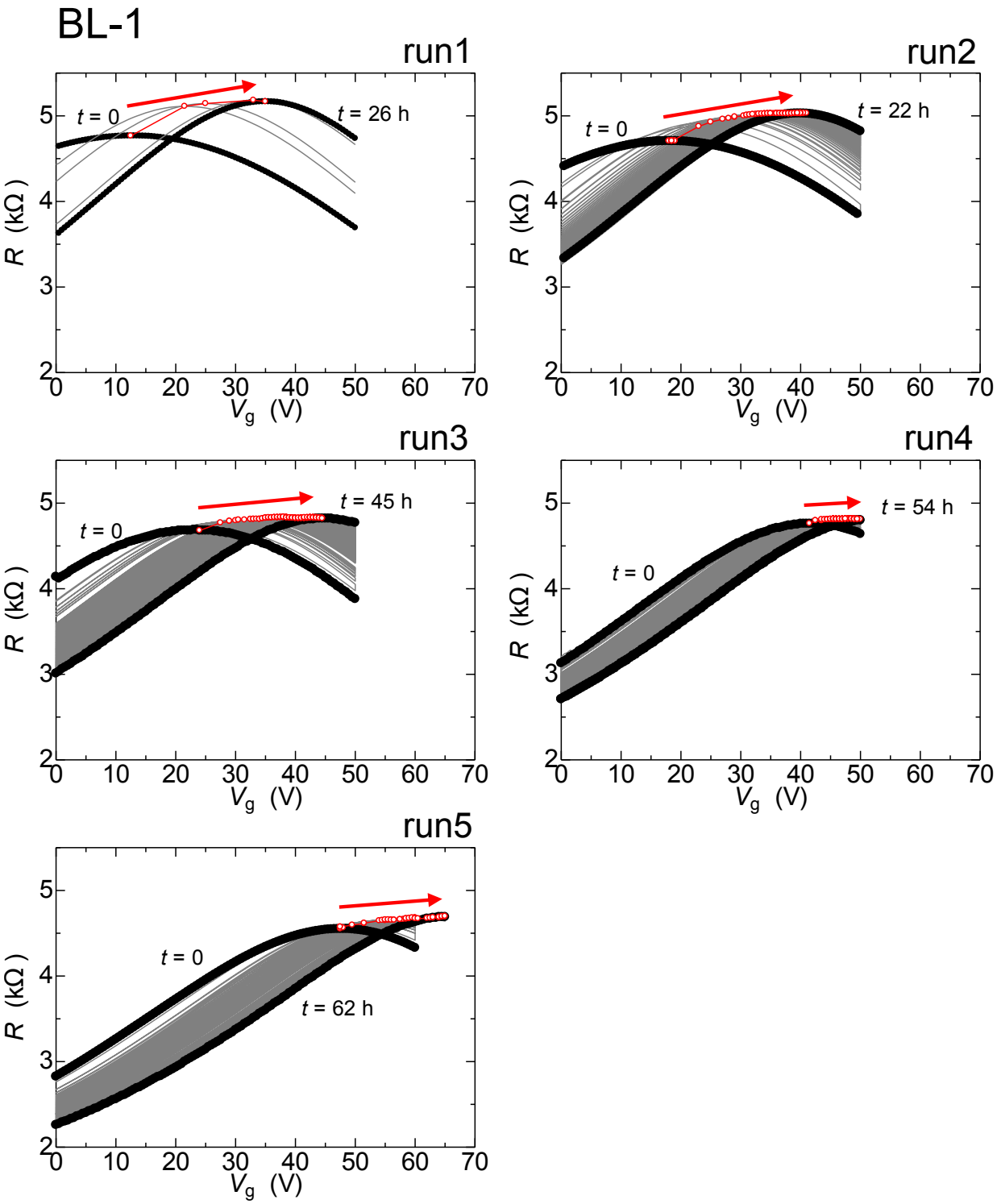

Fig. 84 Time evolutions of V_g vs. R data during the O_2 adsorption for the bilayer graphene sample BL-1. Only for the first and last sweeps, actual data are plotted by the black points, and other sweeps are shown by the thin gray lines. The red open circles are maxima of the resistance, corresponding to the Dirac points.

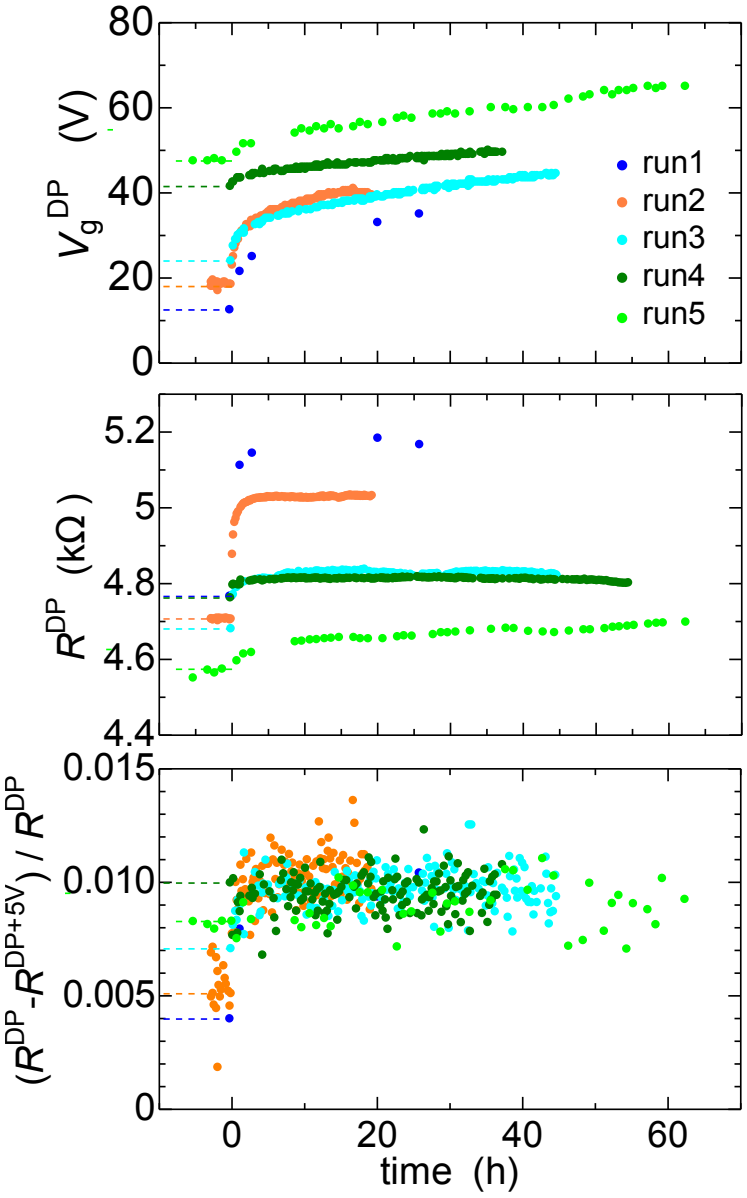

Fig. 85 Time evolutions of the gate voltage at the Dirac point V_g^{DP}, resistance at the Dirac point R^{DP} and resistance drop ratio at 5 V away from the Dirac peak $[R^{DP} - R(V_g^{DP} + 5V)]/R^{DP}$, which corresponds to the sharpness of the peak, during the O_2 adsorption on the bilayer graphene sample BL-1.

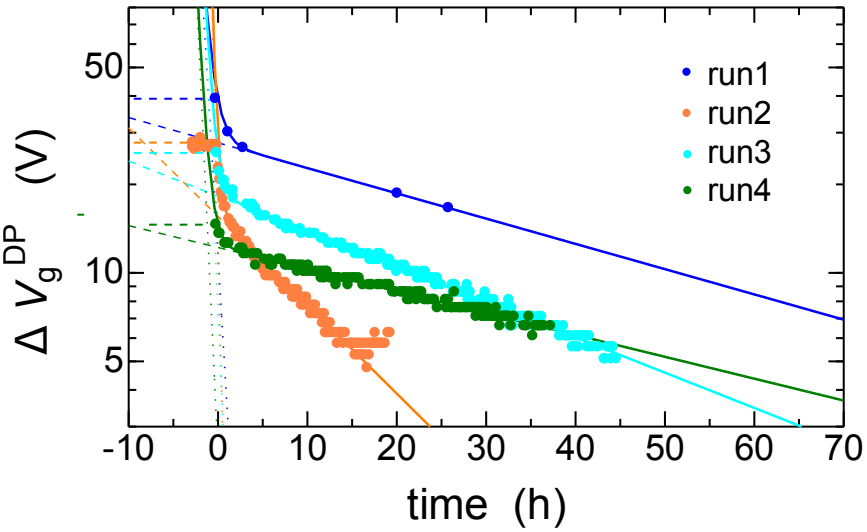

Fig. 86 Semi-logarithmic plot of $V_{\mathrm{g}}^{\mathrm{DP}}$ vs. time for the BL-1 sample. The solid lines are double exponential function fittings to Eq. (72).

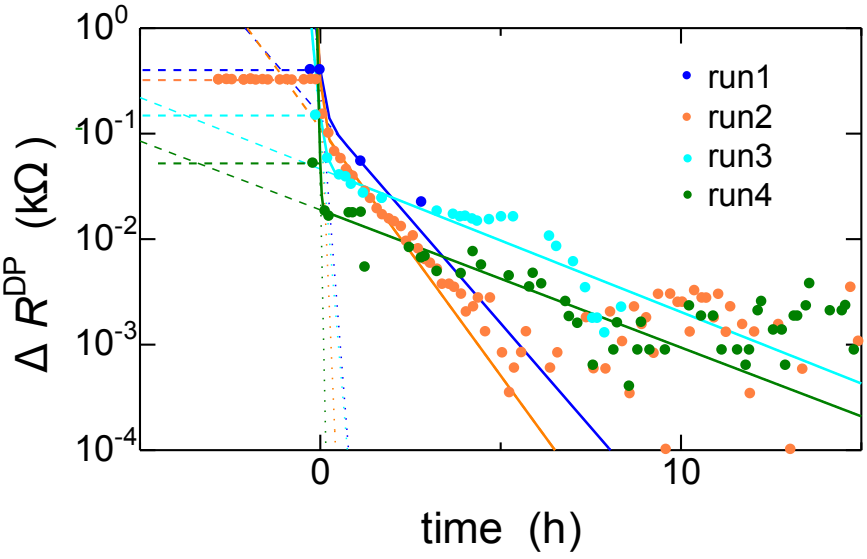

Fig. 87 Semi-logarithmic plot of R^{DP} vs. time for the BL-1 sample. The solid lines are double exponential function fittings to Eq. (72).

Table 12 Parameters obtained from fitting the $R^{\mathrm{DP}}(t)$ data to the double-exponential function (Eq. (72)) for BL graphene samples.

Sample	Run No.	$R^{\mathrm{DP}}(0)$ (kΩ)	a_1 (kΩ)	τ_1 (h)	a_2 (kΩ)	τ_2 (h)
	1	5.17	0.250	0.100	0.150	1.10
	2	5.03	0.209	5.54×10^{-2}	0.112	0.926
BL-1	3	4.83	0.102	0.108	4.62×10^{-2}	3.20
	4	4.81	3.32×10^{-2}	2.67×10^{-2}	1.89×10^{-2}	3.33
	5	5.14×10^{5}	6.82×10^{-2}	2.32	5.14×10^{5}	6.21×10^{8}

The width of the Dirac peaks changed so rapidly that the values saturated just after the introduction of O_2, and the fitting to the time evolution was not possible. The peak width was decreased, which is curious behavior, because increase in peak width is assumed if adsorbates act as scatterers. This is possibly because of multiple peaks within seemingly one peak, caused by inhomogeneous charge doping by substrate and/or impurities. If the multiple peaks shift individually, then apparent width of the peak would be changed.

The faster change in the parameters by O_2 adsorption is supposed to be arising from the higher reactivity of the bilayer graphene than the monolayer graphene. Experimental results of oxidative etching of graphene at temperatures above room temperature will help to understand this phenomenon. While it is reported that generation of the oxidative etch pits on the basal plane is faster in monolayer graphene [150, 151], it is also reported that the larger the number of graphene layers, the faster the growth of the oxidative etch pits [152, 153], which means that the oxidation at the edges becomes faster as the number of layers increases. This is believed to be due to the effect of the oxygen at adjacent edges cooperating to proceed the reactions. That is, reactions that cause hole doping and parameter changes occurred at edges rather than on the basal plane of graphene, and as a result, rapid changes was observed in the bilayer graphene. It has been experimentally demonstrated that the transport property at the graphene edge can be extracted by applying the gate voltage only at the edge [154]. Edge transport measurements during the oxygen exposure may be realized, for example, by using comb-shaped back gate to apply the back gate voltage only at the graphene edge.

3.3.3. Hole doping at low temperatures

To examine how the hole doping proceeds at lower temperatures than R.T., we adsorbed O_2 on ML-4 sample at a fixed temperature of $T = 80$ K first, and then monitored the R vs. V_{g} characteristic on subsequent warming to R.T. Unfortunately, during the microsoldering on this particular graphene sample, a small indium piece was accidentally dropped onto the graphene in between the two voltage electrodes. We removed it, but the graphene surface or electrodes could be damaged somehow.

Figure 88 is a measured gate voltage dependence of resistance of ML-4 before and after O_2 adsorption at $T = 80$ K. From the double peak shape, we assume that this sample is composed of two pieces with largely different doping levels. The O_2 gas was introduced

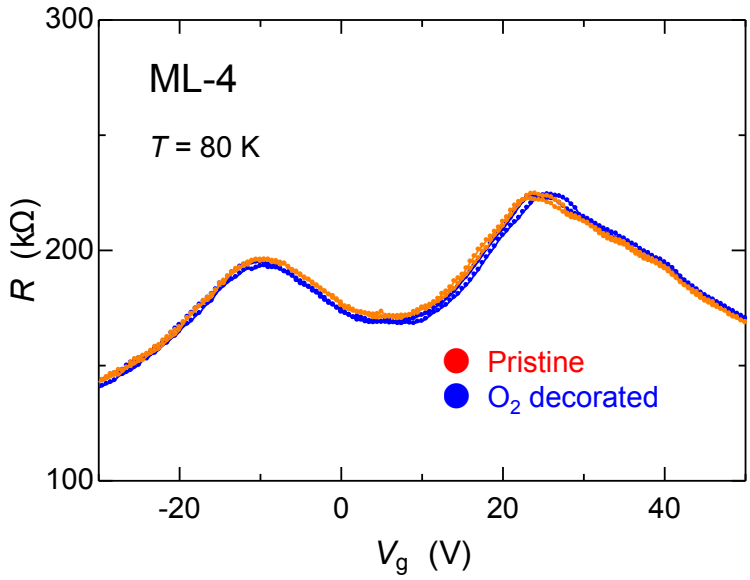

Fig. 88 Gate voltage dependence of resistance for ML-4 before and after O_2 adsorption at T = 80 K

little by little until the pressure reaches 140 Torr, but no significant change in the resistance was observed during the adsorption. Thus, the hole doping does not occur at T = 80 K.

Then, the temperature of the sample was gradually increased, while continuously measuring the gate voltage dependence of resistance (see Fig. 89). The peak originally located

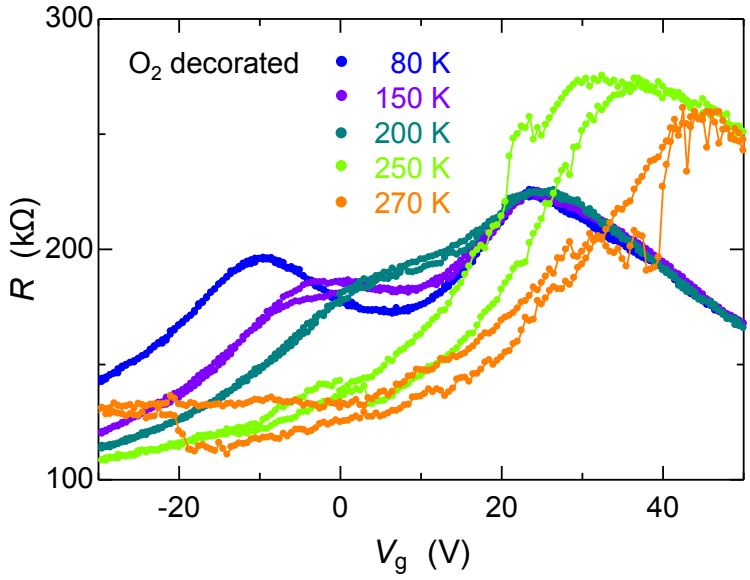

Fig. 89 Gate voltage dependence of resistance during the temperature increase after the O_2 adsorption at T = 80 K. The 80 K data are the same as those plotted in Fig. 88.

at a lower gate voltage ($V_g = -11$ V) starts to shift upward at around 120 K decreasing

the peak height (or its spectral weight), while the other peak located at a higher V_g of +23 V does not change the peak position up to 200 K. The low V_g^{DP} peak is then merged to the high V_g^{DP} one, and the resultant single peak shifts toward higher gate voltage in the sub sequent warming above 250 K.

An interesting question is which parts in the sample correspond to the two peaks. We speculate that the low and high V_g^{DP} peaks correspond to a clean graphene surface and that covered by the indium residue, respectively. On the clean surface, the chemical reaction which causes the hole doping starts to take place by thermal energies above 120 K. The thermal energy may be necessary to overcome the energy barrier for the chemisorption described in Section 3.1.1 or to surface diffuse to defect sites on graphene. On the other hand, such processes would be suppressed on the indium contaminated graphene surface where O_2 should intercalate into the interface between the indium residue and graphene. Indium is known to donate electrons to graphene [155], so the indium residue might act as a reservoir of carriers. This would somehow suppress the hole doping effect of O_2, and higher thermal energies may be necessary to recover the effect. Anyway, physisorped O_2 molecules need an activation energy of 120 K at least to dope holes into graphene. From this, it is understood that the reaction is rate-limited by the thermal activity at the defect site, not the surface diffusion of the oxygen molecular species.

3.3.4. Low temperature transport properties of O_2 adsorbed graphene

After the O_2 exposure measurement for the sample ML-3 at room temperature, the sample cell was evacuated for 18 hours at room temperature. The evacuation caused no effect on the gate voltage dependence of resistance (Fig. 90), which means that the hole doping is completely irreversible at room temperature. This result is consistent with the previous report [110].

The sample was then cooled down to 2 K using a glass dewar with liquid helium. Fig. 91 shows gate voltage vs. resistance data taken at several different temperatures before and after the adsorption. The flat shape of the Dirac peak of pristine graphene at low temperatures is possibly an ensemble of multiple peaks coming from different positions, which was presumably caused by inhomogeneous carrier doping from the substrate. Many small peaks appeared at $T < 10$ K even before the adsorption. To subtract a smoothed base line for the V_g vs. R data so that we can examine the complicated peak structure more in detail, the data points within a ± 1.0 V or ± 1.5 V window about each data point were averaged. Then, the smoothed base line was subtracted from the raw data points giving Figs. 91(c)(f). It is obvious that the peak amplitude becomes larger with lowering the temperature. The peak structure was unchanged over a number of V_g sweeps and reproducible as long as the temperature was kept below liquid nitrogen temperature ($T = 77$ K). Once the sample was warmed up to $\sim$200 K, however, details of the peak structure were changed and the peak amplitude was enhanced presumably due to contamination with new adsorbents. After information described above, we attribute the origin of the peaks to quantum interference caused by inhomogeneities, such as charge inhomogeneities caused

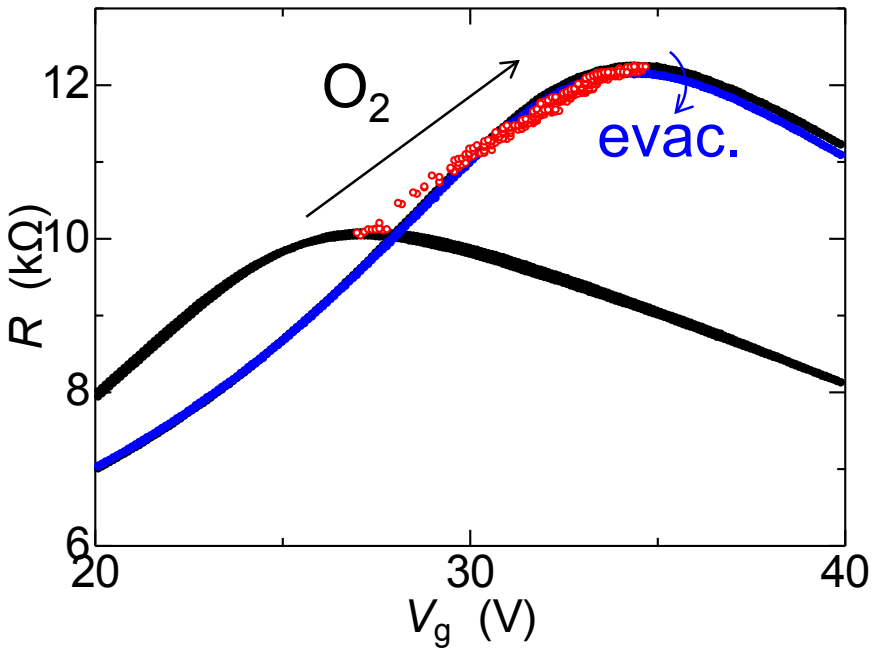

Fig. 90 Gate voltage dependence of resistance before and after the O_2 adsorption and evacuation. Red circles are positions of the maximum at each sweep during the adsorption.

by the substrate or adsorbent molecules. Similar oscillations have been observed by other group [156, 157], where the origin has been attributed to the intervalley scattering.

Figure 92 shows temperature dependence of the averaged resistances at a typical peak ($V_g = 30.8$ V) and an anti-peak ($V_g = 29.3$ V). Although the temperature range ($2 \leq T \leq 20$ K) and temperatures (T = 2.0, 2.2, 2.5, 3.0, 4.0, 5.0, 10.0 and 20.0 K)) where we took the data is rather limited, the data are well described by the two-dimensional variable range hopping (2D VRH) model: $R \propto \exp(T_0/T)^{1/3}$, both before and after the O_2 adsorption. There are small discontinuities in the data at around 3.4 K, which is the superconducting transition temperature (T_C) of indium used for the electrodes. The temperature dependence was changed over and below the T_C, still obeying the 2D VRH. Here, T_0 over and below the T_C are defined as T_0^{HT} and T_0^{LT}, respectively. The discontinuity might be due to the change in effective sample configuration. Superconducting proximity effect [158] by indium electrodes might reduce the resistance by reducing the effective sample size which contribute to the sample resistance. Change in T_0 is then explained by inhomogeneous distribution of the impurities or adsorbates inducing localized states.

Figure 93 is T_0's extracted for each gate voltage. Near the Dirac points, both T_0^{LT} and T_0^{HT} increased by O_2 adsorption. There may be two ways to interpret the increase in T_0: decrease in density of states $g(\mu)$, or decrease in radius of localized states ξ. It is difficult to assume the former as a result of O_2 adsorption. The latter is realistic by assuming such mechanism that oxygen molecular species adsorb on existing impurities or defects and decrease their effective radius (or strengthen the localization). Therefore, contribution of adsorbed oxygen molecular species to the increase in localized states do not occur, or

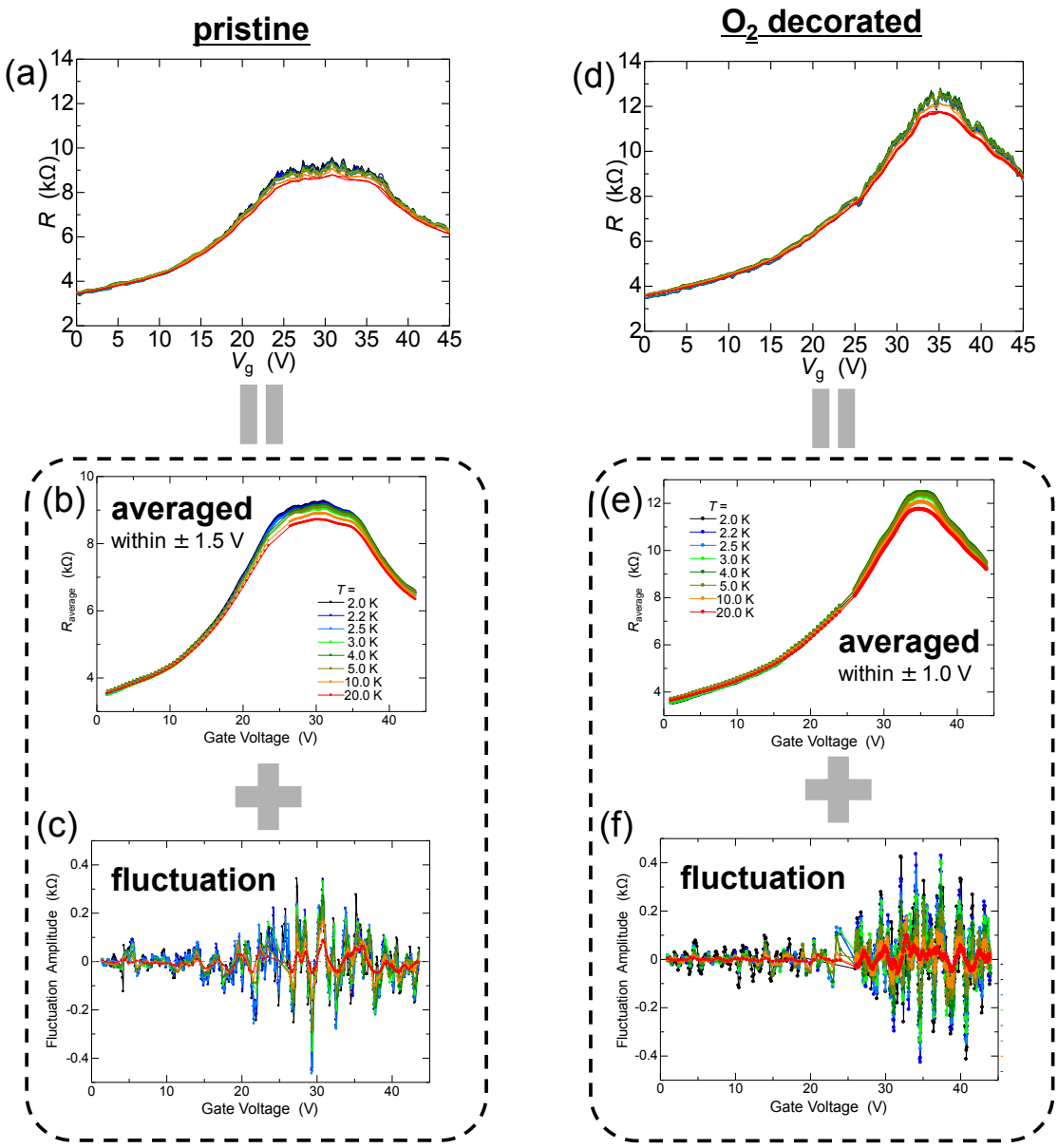

Fig. 91 Gate voltage vs. resistance at several different temperatures before and after the adsorption. Many small peaks appeared at $T < 10$ K. The data points within a ±1.0 V or ±1.5 V window about each data point were averaged to extract the smoothed base line.

limited.

3.4. Conclusion

In order to clarify the carrier (hole) doping characteristic in graphene by exposure to oxygen gas, we first developed the indium microsoldering technique which enabled us to

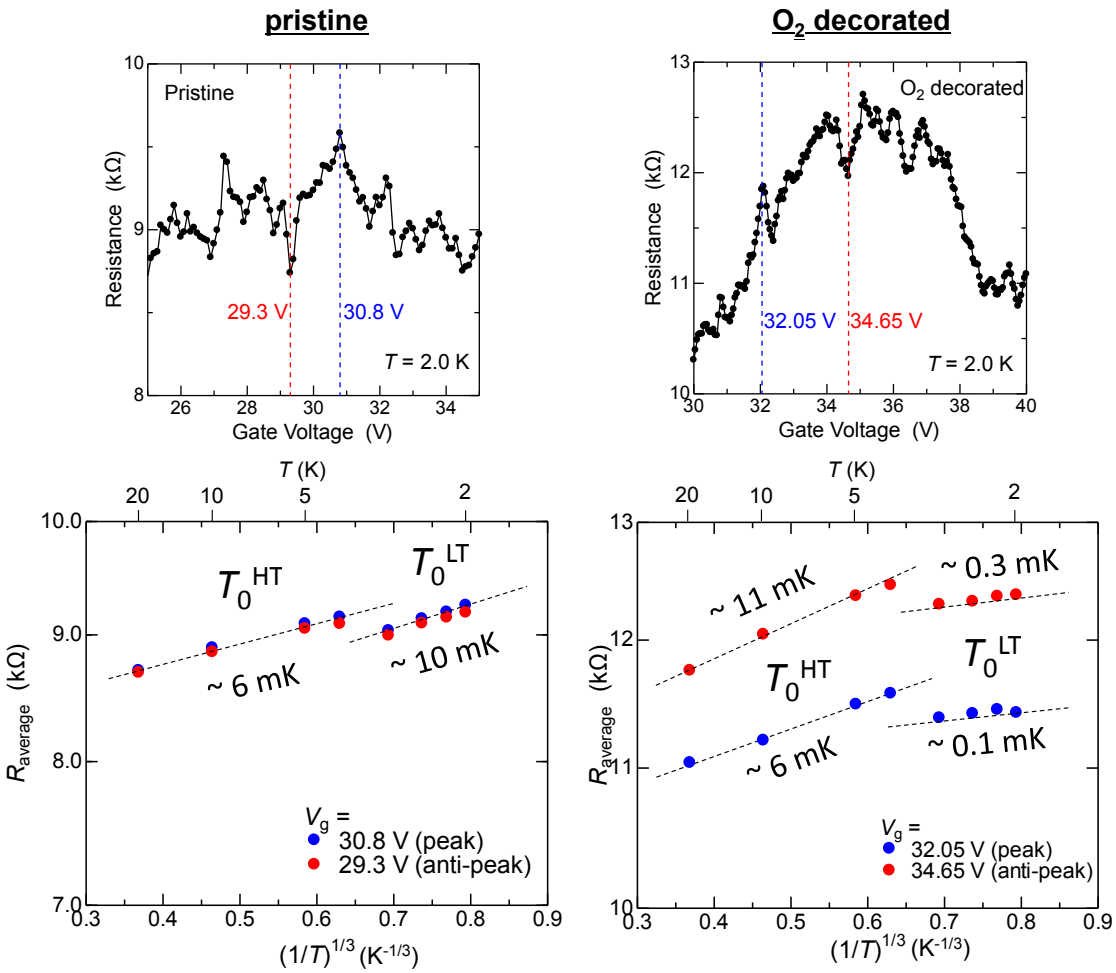

Fig. 92 Temperature dependence of averaged resistances at peak and anti-peak position before and after the O_2 adsorption

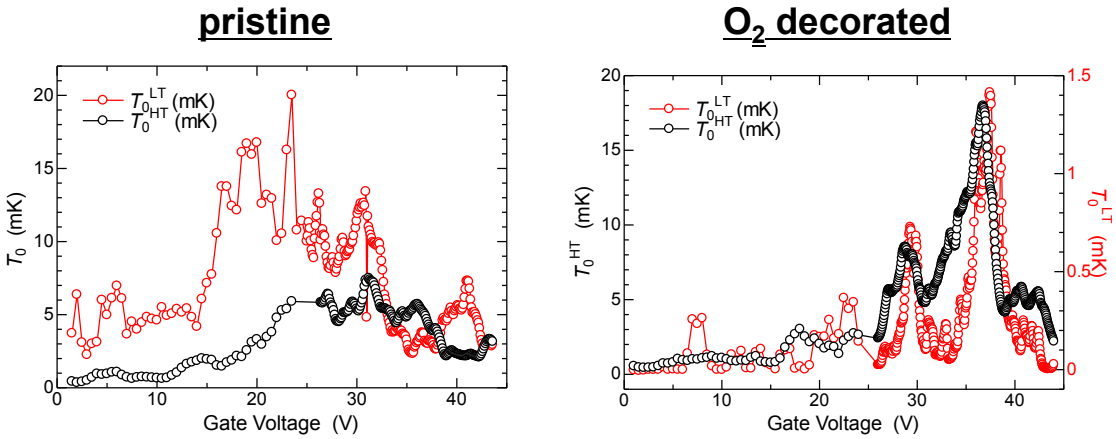

Fig. 93 VRH parameter T_0 extracted for each gate voltage, before and after the O_2 adsorption

fabricate four microelectrodes onto a small exfoliated graphene sample of about 10 μm long without using any liquids (dry process). Then we carried out measurements of the long-term time evolution of the gate voltage (V_g) dependence of sample resistance after the oxygen exposure (P = 400-600 Pa) at room temperature by continuously sweeping V_g up and down.

Unlike the previous research on bilayer (BL) graphene reporting the power law time dependence, our data on both BL and monolayer (ML) graphenes showed the two-step behavior described by the sum of two exponential functions: $\Delta V_g^{DP}(t) = a_1 \exp(-t/\tau 1) + a_2 \exp(-t/\tau 2)$. Here V_g^{DP} is the bias voltage corresponding to the Dirac point, whose shift is a measure of the doped hole concentration, and τ_1 and τ_2 are the short time constant and the long one, respectively. The observed time evolution is clearly not associated with the surface diffusion of oxygen but with thermally activated chemical reactions, most likely at defect sites, involving at least two elementary reaction processes. The hole doping concentrations (a_1, a_2) in BL are much larger than in ML by one order of magnitude. In BL, the doped hole concentration was 4×10^{12} cm^{-2} (ΔV_g = 60 V) at most. The time constants (τ_1, τ_2) are not so different between BL and ML, but BL has slightly shorter values roughly by a factor of two. Apparently, the reactivity of oxygen is much higher in BL graphene, and the reaction takes place presumably at edge defects rather than surface defects. The thermally activated nature of the reaction was verified from the observation that no hole doping proceeds when oxygen is adsorbed at a low temperature (T = 80 K, P = 0.18 bar) and that, on subsequent heating above 150 K, the reaction starts. By repeating the cycle of oxygen exposure and evacuation at room temperature, it was found that a part of the reaction has a larger activation energy than 100°C (more stable final state).

The V_g vs. R data showed many small peaks at $T < 10$ K, which may be attributed to quantum interference caused by inhomogeneities in the sample. The temperature dependence within $2 \leq T \leq 20$ K showed 2D VRH behavior, and the characteristic temperature T_0 increased by O_2 adsorption, indicating that the localization is strengthened by adsorbed O_2 molecular species.

4. Attempts of band gap opening by gas adsorption

4.1. Background

4.1.1. Possible band gap opening in graphene

Graphene has band structure with conduction band and valence band touching at Dirac point. However, conduction band and valence band have to be isolated with energy gap in between to make it work as FET. With the gap, on/off feature is obtained by modulating the Fermi energy in and out of the gap by applying gate voltage to change the carrier density.

Graphene has bipartite lattice with two identical triangular lattices A, B as sublattices (Fig. 94). Energy gap is induced by breaking the symmetry of sublattices [159]. Hamilto-

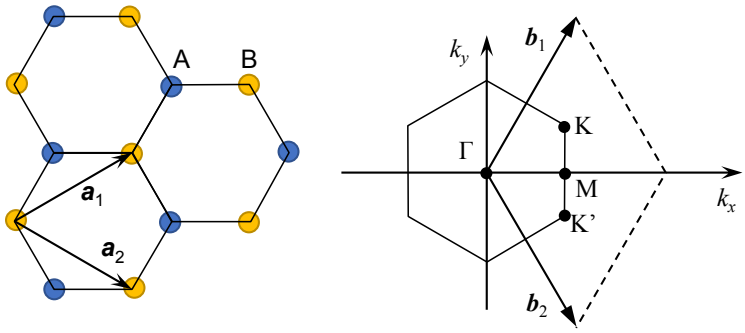

Fig. 94 Lattice of graphene. left: Real space representation, consist of two sublattices A and B. right: Reciprocal lattice space representation.

nian of graphene near the Dirac point is written as

$$H = \begin{pmatrix} \Delta & v_{\mathrm{F}}(k_x - \mathrm{i}k_y) \\ v_{\mathrm{F}}(k_x + \mathrm{i}k_y) & -\Delta \end{pmatrix} \tag{74}$$

[32, 159, 160]. Here, k is wave number, v_{F} is Fermi velocity, Δ is on-site energy difference on sublattice A and B, and it operates on a wave function $\psi = {}^{\mathrm{t}}(\phi_{\mathrm{A}}\ \phi_{\mathrm{B}})$ written with wave functions of sublattices A and B ϕ_{A}, ϕ_{B}. In an ideal graphene, with $\Delta = 0$, it results in linear dispersion relation $E = \pm v_{\mathrm{F}}|k|$ and no gap exists. On the other hand, when the symmetry of sublattices A and B is broken ($\Delta \neq 0$), $E = \pm\sqrt{\Delta^2 + (v_{\mathrm{F}}k)^2}$ and finite gap is induced.

To realize this, several methods has been proposed and realized; fabricating graphene into quantum dots [161], nanoribbons [162, 163] and using the effect of substrate such as graphene on SiC [164, 165].

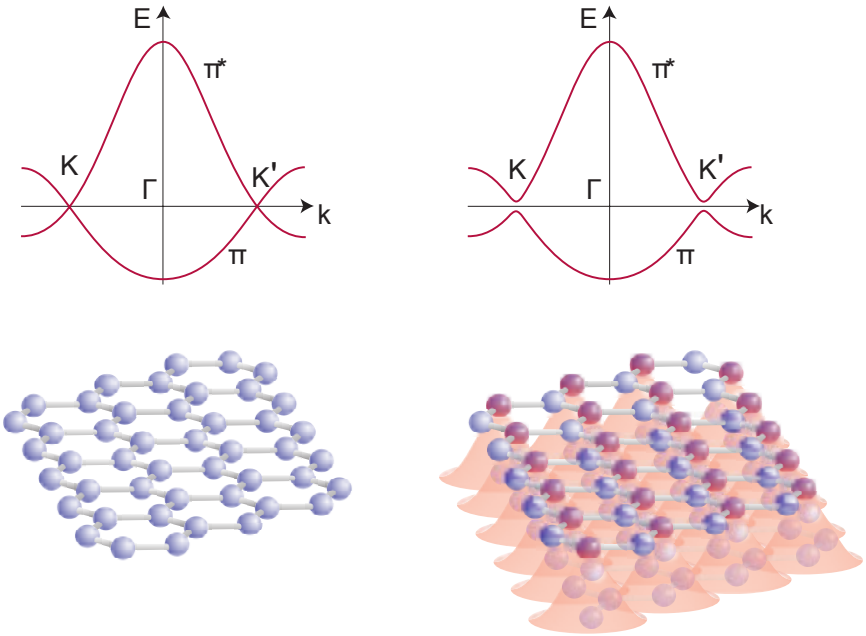

Fig. 95 Gap induced by AB symmetry breaking [165]. Left: band structure and lattice structure of graphene. Right: difference in AB sublattices made by the effect of substrate induces the gap.

Besides, in bilayer graphene, electric field perpendicular to the surface induce the gap (Fig. 96) [166, 160]. Sublattices of two layers A1, B1, A2 and B2 result in four bands, in which only two bands have influence, and the effective Hamiltonian is written as

$$H = \begin{pmatrix} \Delta & -(\hbar^2/2m)(k_x - \mathrm{i}k_y)^2 \\ -(\hbar^2/2m)(k_x + \mathrm{i}k_y)^2 & -\Delta \end{pmatrix} \tag{75}$$

[168, 160]. This operates on a wave function $\psi = {}^{\mathrm{t}}(\phi_{\mathrm{A1}}\ \phi_{\mathrm{B2}})$. As the sublattices belong to different layers, the symmetry is broken by applying electric field perpendicular to the surface, and gap is induced.

It is theoretically expected that energy gap is induced in graphene when lithium atoms are adsorbed in $(\sqrt{3} \times \sqrt{3})R30^\circ$ (more generally, $(n\sqrt{3} \times n\sqrt{3})R30^\circ$) periodicity [169]. According to the calculation, adsorption of lithium modifies the C-C bonds, which are originally identical, into 2 types (Fig. 97). As a result, in the tight binding hamiltonian

$$H = \sum_i \epsilon_i c_i^\dagger c_i - \sum_{ij} t_{ij} c_i^\dagger c_j \tag{76}$$

hopping amplitude t_{ij} are modified into two values t_1 or t_2. Here, energy gap determined by the difference of these two values $E_g = 2|t_2 - t_1|$ is expected to be induced (Fig. 98).

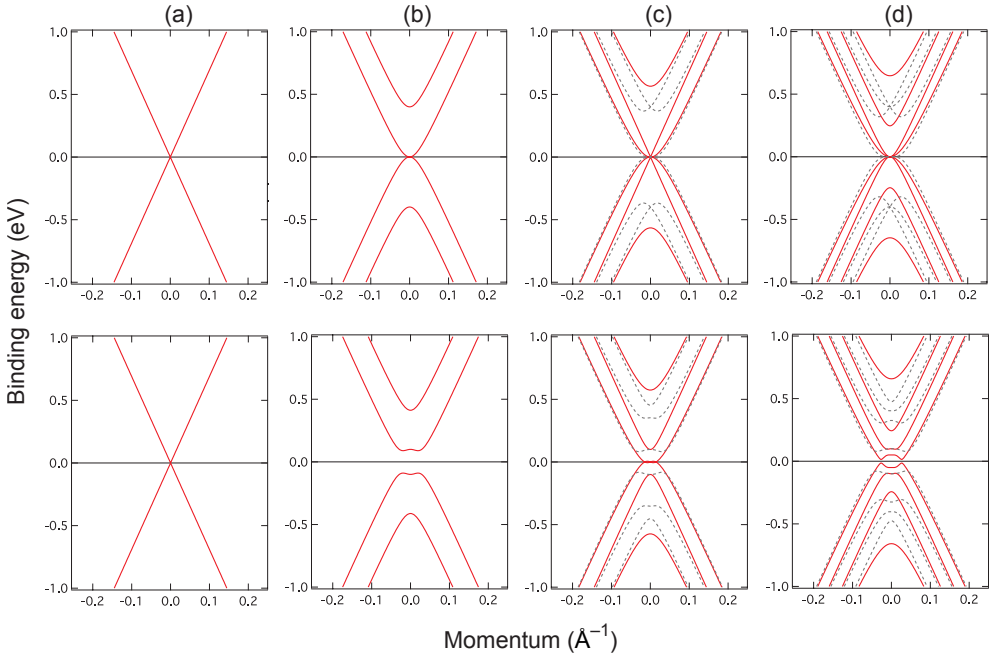

Fig. 96 Change in band structure of 1∼4 layer graphene when electric field perpendicular to the surface is applied [167]. (a)∼(d) are 1∼4 layers, respectively. Upper figures are without electric field, and lower figures are with electric field. Solid and dashed lines are for different stacking of graphenes; solid lines are Bernal (AB) stacking, and dashed lines are rhombohedral (ABC) stacking case. Gap is induced in bilayer graphene when electric field is applied.

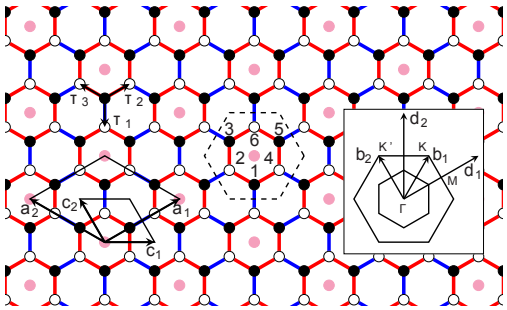

Fig. 97 Two unidentical C-C bonds shown by red and blue lines emerge by lithium $(\sqrt{3}\times\sqrt{3})R30^\circ$ phase adsorption [169].

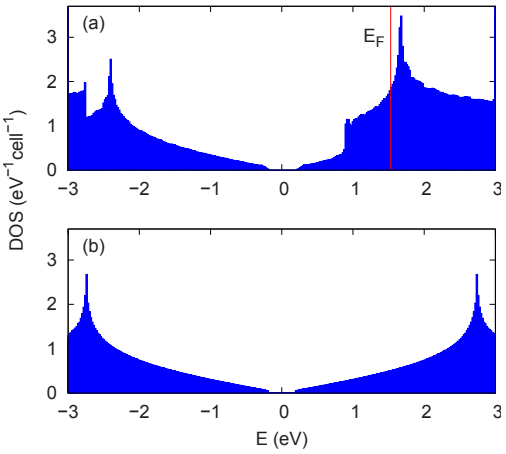

Fig. 98 Energy gap induced by lithium $(\sqrt{3}\times\sqrt{3})R30^\circ$ phase adsorption [169]. Above: DFT calculation, below: tight binding calculation.

In our laboratory, in the system of noble gas atoms (helium, krypton and xenon) adsorbed on graphite, dips around the Fermi energy in density of states, which possibly be interpreted

as energy gaps, were observed by tunneling spectroscopy using STM [170, 171] (Fig. 99).

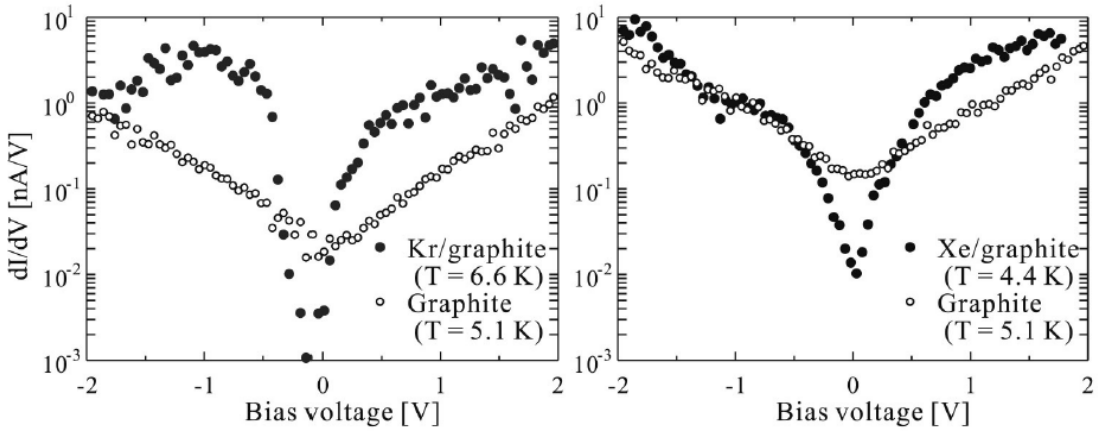

Fig. 99 Dips in density of state, which possibly be interpreted as energy gaps, observed using STM [171].

The modification of density of states did not exist in graphite. Possible origin is symmetry breaking in the surface one layer graphene. Other possibilities are symmetry breaking in two layers of graphene, or local deformation of graphite surface [172].

Another experiment is CO molecules arranged on the Cu(111) surface, where 2-dimensional electron system of the substrate is modulated to form graphene-like honeycomb structure. Here, too, gap induction under the condition $t_1 \neq t_2$ was confirmed [173].

Previous trials of gap inducing by gas adsorption in our laboratory were not successful. One possible reason is the effect of the substrate. Surface hydroxyls or charged impurities in the SiO_2 layer are known to affect the graphene on it, in terms of electrical transport properties [174] and chemical reactivity [146]. Also, the adsorbates may go underneath the graphene, which was confirmed by adsorption experiment [175], and also suggested by STM measurements in our laboratory. To exclude the effect of the substrate, suspended graphene was decided to be introduced.

4.1.2. Kr physisorbed on graphite

Graphite physisorbs various atoms or molecules on its surface by van der Waals force. Pressure of gas phase (vapor pressure of adsorbed solid) and areal adsorption density are in a certain relation when they are in equilibrium. The relation of pressure and areal density is represented by adsorption isotherm. A model only taking surface-adsorbate interaction into account was considered by Langmuir [176], in which areal density increases with the pressure gets higher, and finally saturates when all the adsorption sites are occupied by adsorbates. For real, interactions between adsorbates have to be taken into account [177]. As the adsorbates have finite effective radius, 2nd and 3rd layers are formed when the areal density exceeds certain value. It can be observed as steps in the adsorption isotherm (Fig. 100) [178].

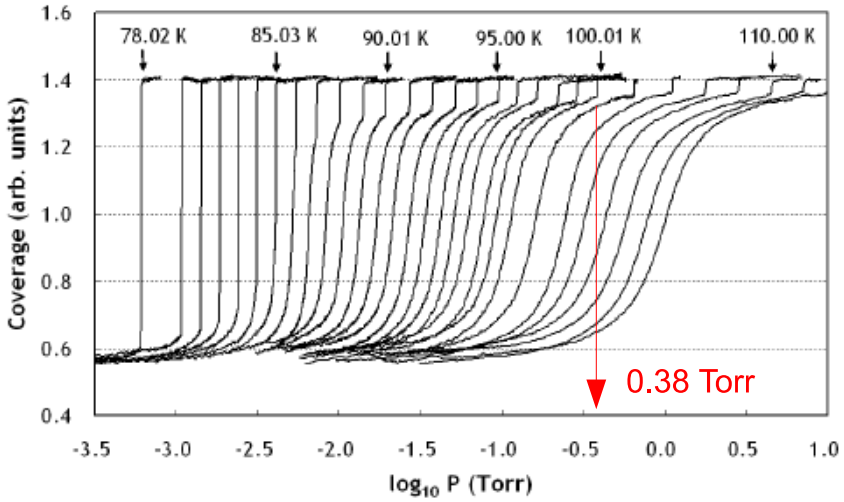

Fig. 100 Adsorption isotherm of krypton on graphite [179]. Substeps correspond to $(\sqrt{3}\times\sqrt{3})R30^\circ$ phase is observed.

Adsorbed molecules show various phases depending on areal density and temperature, which results in phase diagram(Figs. 101, 56). Especially in some cases, solid phases which reflect the periodicity of graphite surface (commensurate phase) are realized. The potential set up by adsorbed molecules can be utilized to apply periodic modulation to the graphite.

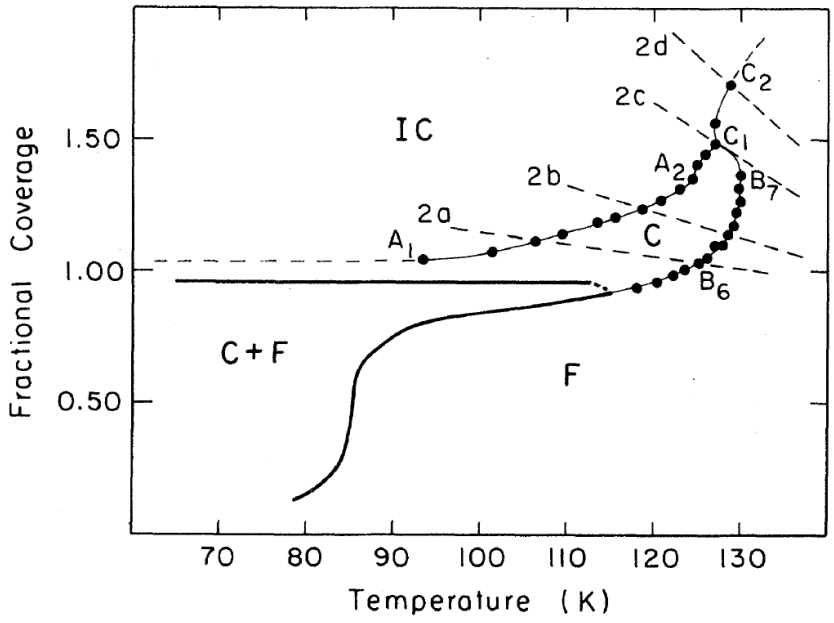

Fig. 101 Temperature-areal density phase diagram of krypton on graphite [180]. F: Fluid phase, C:Commensurate solid phase, IC:Incommensurate solid phase.

4.2. Experimental methods

4.2.1. Grafoil stack

Same sample cell as oxygen adsorption experiments (Fig. 72) was also used in this experiment. Because graphene has small area, change in the areal density against adsorption amount is too large. To realize precise control of areal density, exfoliated graphite which has large surface area was included to the same space as graphene sample. When the chemical potentials on graphene an on graphite are in equilibrium, areal density on graphene and macroscopic adsorption amount on graphite come to corresponds to each other, which enable precise control.

Grafoil, a kind of exfoliated graphite, was used sandwich a silver foil and bonded by thermocompression. 20 sandwiches were stacked to make Grafoil stack (Fig. 102) and then fixed inside the sample cell. The silver foils enable rapid thermal relaxation of the whole

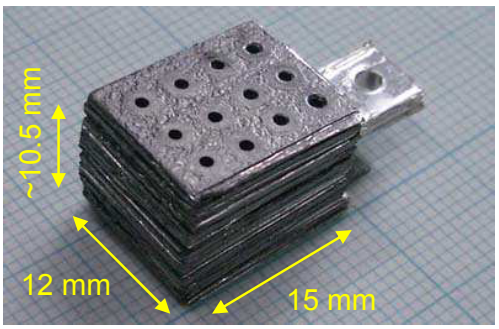

Fig. 102 Appearance and scale of the Grafoil stack

Grafoil stack. They also shorten the cooling or heating time. Through-holes were opened to reduce the impedance and shorten the pressure relaxation time during gas adsorption or pumping. It was designed to have about 40 m^2 surface area, by estimation from Grafoil stack previously made [181].

Procedure of Grafoil stack making is shown below. Grafoils and silver foils were cut into 12 mm×15 mm in advance. Silver foils have tab-like on a side, which can be used to fix grafoil stack to the sample cell.

1. Grafoil baking. They were baked in vacuum at 1000°C for 24 h using oil diffusion pump and electric furnace.

2. Silver foil etching. They were immersed in 10% HNO_3 for 15 min.

3. Silver foil baking. They were baked in 10^{-5} Torr air atmosphere at 650°C for 2 hours.

4. One silver foil was sandwiched with two Grafoils, and then many of them were stacked. It was then pressurized perpendicular to the surface by 2 MPa using hydraulic jack. Stainless steel jig was used to keep the thickness when it was pressurized.

5. Diffusive bonding. It was baked in vacuum at 650°C for 3 hours with the jig.

6. Boring. Cigarette papers were inserted in between the Grafoils, and then many through holes perpendicular to the surface were opened using $\phi 1$ drill bits. To avoid the contamination of Grafoil by cutting oil on the drill bits, they were immersed in acetone and ultrasonic-cleaned in advance. This possibly accelerate the wearing of drill bits, so number of the holes opened by one bit was limited to three.

4.2.2. Realization of $(\sqrt{3} \times \sqrt{3})R30°$ structure on graphene

$(\sqrt{3} \times \sqrt{3})R30^\circ$ phase of adsorbate atoms on graphite is formed for certain temperature and pressure region. To realize $(\sqrt{3} \times \sqrt{3})R30^\circ$ phase on graphene, difference in the adsorption energy between graphite and graphene have to be taken into account. As there was no experimental determination of temperature and pressure region of $(\sqrt{3} \times \sqrt{3})R30^\circ$ phase reported, it had to be estimated from theoretical calculations.

Let $\mu(P, T)$ the chemical potential on the surface of substrate which is in equilibrium with gas phase with pressure P and temperature T. Relation of chemical potentials at two different pressure P_0, P_1 is

$$\mu(P_1, T) = \mu(P_0, T) + k_\mathrm{B} T \ln \frac{P_1}{P_0} \tag{77}$$

and thus using the energy difference $\Delta\epsilon = \mu(P_1, T) - \mu(P_0, T)$,

$$P_1 = P_0 \exp(\Delta\epsilon / k_\mathrm{B} T) \tag{78}$$

follows. Regarding $\Delta\epsilon$ as difference in adsorption energies of graphene and graphite, a pressure P_0 in the phase diagram of adsorbates on graphite is converted to that on graphene, P_1, using the relation above.

In this research, krypton was chosen as the adsorbate because it is the largest among noble atoms that are capable of forming $(\sqrt{3} \times \sqrt{3})R30^\circ$ phase on graphite. $\Delta\epsilon$ was estimated in three methods by using theoretically obtained adsorption energies (Table 13).

1. Estimation from adsorption energies of Xe/graphite, Xe/graphene in a calculation [182] and Xe/graphite, Kr/graphite in another calculation [183]. $\Delta\epsilon$ was obtained as

$$\Delta\epsilon = (188.3 - 126.8)\frac{160}{204} = 48 \text{ meV}. \tag{79}$$

2. Interpolation from calculations of other noble gases. From the adsorption energies of He, Ar and Xe on graphite and graphene [182], that of Kr was estimated by interpolation with respect to their mass (Fig. 103). $\Delta\epsilon = 45$ meV was obtained.

3. Direct calculation from adsorption energies of Kr/graphite and Kr/graphene appear within one paper [184]. $\Delta\epsilon = 135.8 - 122.7 = 13.1$ meV.

As summarized in Table 14, estimated pressure showed wide variation. To overcome this, C+F phase where $(\sqrt{3} \times \sqrt{3})R30^\circ$ phase exists in coexistence with liquid phase for wide pressure range below 85 K was chosen for the experiment, rather than pure C phase with narrow pressure range.

Table 13 Adsorption energies of noble gas atoms on graphite and graphene by theoretical calculations. Values are in meV.

adsorbate/substrate	Ref. [182]	Ref. [183]	Ref. [184]
He/graphite	−13.0		
He/graphene	−11.6		
Ar/graphite	−106.4		
Ar/graphene	−78.0		
Xe/graphite	−188.3	−160	
Xe/graphene	−126.8		
Kr/graphite		−204	−135.8
Kr/graphene			−122.7

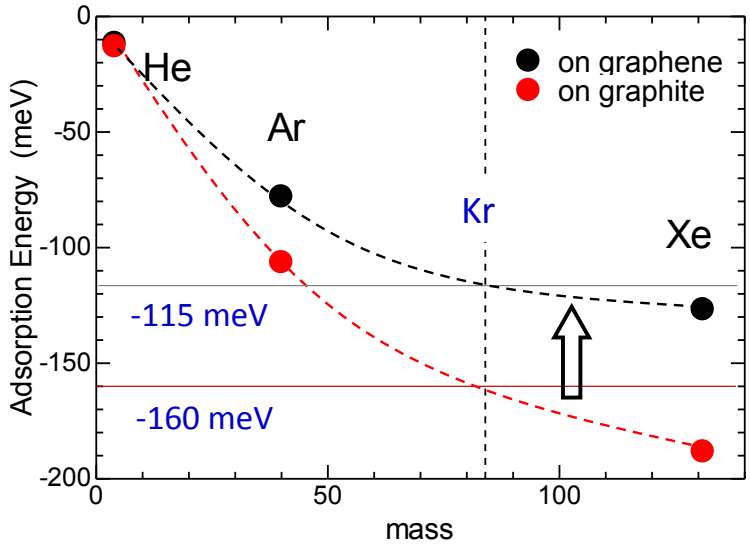

Fig. 103 Estimation of adsorption energies of Kr/graphite and Kr/graphene by interpolation. Values for He, Ar and Xe are extracted from Ref. [182].

4.2.3. Suspended graphene

Suspended graphene was realized with trenched substrate. Before the graphene exfoliation, trenches were fabricated by plasma etching. The process was done in VLSI Design and Education Center (VDEC) [185].

1. A SiO_2/Si substrate with 285-nm thick SiO_2 layer was cut into 3 cm×3 cm by stealth dicer.

2. The substrate was ultrasonic-cleaned with acetone and ethanol, then cleaned by flowing water. It was then soft-baked to be dried.

3. EB resist ZEP-520A was spin-coated on the substrate at 400 rpm for 60 sec. It was then pre-baked at 180˚C for 5 min.

Table 14 Summary of the estimations of $\Delta\epsilon$. Estimated pressure to realize $(\sqrt{3}\times\sqrt{3})R30^\circ$ phase on graphene are also shown.

	Method 1	Method 2	Method 3
Kr/graphite adsorption energy	−204 meV	−160 meV	−135.8 meV
Kr/graphene adsorption energy	−156 meV	−115 meV	−122.7meV
$\Delta\epsilon$	48 meV	45 meV	13.1 meV
graphene $\sqrt{3}$ phase pressure at 100 K	99.5 Torr	70.3 Torr	1.74 Torr

4. The pattern of trenches were drawn by EB lithography.
5. The substrate was developed in liquid developer ZED-N50 for 60 seconds, then rinsed in ZMD-B for two times.
6. Organic contaminants on the substrate was removed by O_2 plasma for 5 minutes. The SiO_2 layer was then etched by CHF_3 plasma at 38 W for 42 sec. The etching speed is 144 nm/min.
7. The resist was removed by liquid remover. The substrate was then rinsed in ethanol and water.
8. The substrate was cut again with stealth dicer into 1 cm×1 cm size.

Trenches were 1 μm wide and 100 nm deep, separated by 3 μm from each other (Figs. 104, 105).

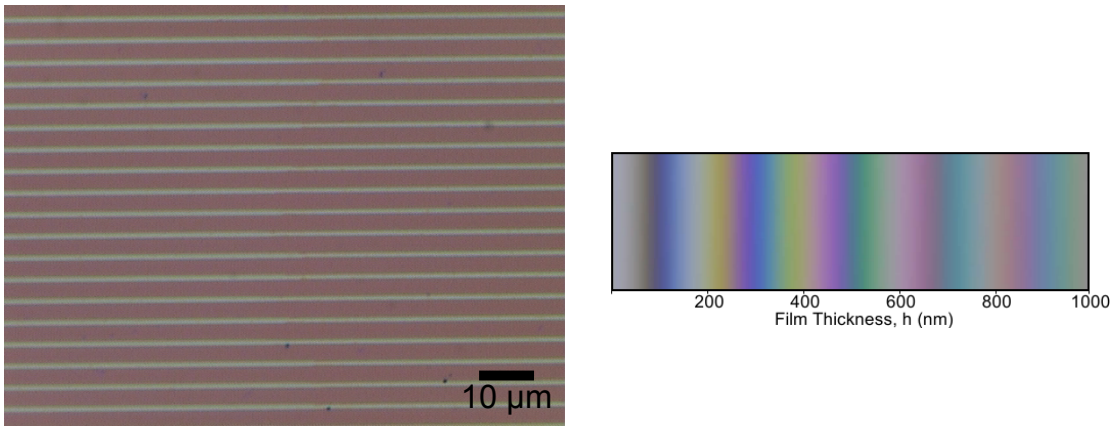

Fig. 104 left: Optical image of trenches fabricated on SiO_2 layer of SiO_2/Si substrate. The thickness of SiO_2 layer is 285 nm and the depth of the trenches are 100 nm. right: Relation between the thickness of SiO_2 layer and the color [186]. The thickness of SiO_2 layer in trenched region estimated by its color was indeed around $285 - 100 = 185$ nm.

Exfoliation and transfer of graphite onto the trenched substrate was done in the same procedure as ordinary substrate case. Exfoliated graphite flakes and graphene successfully

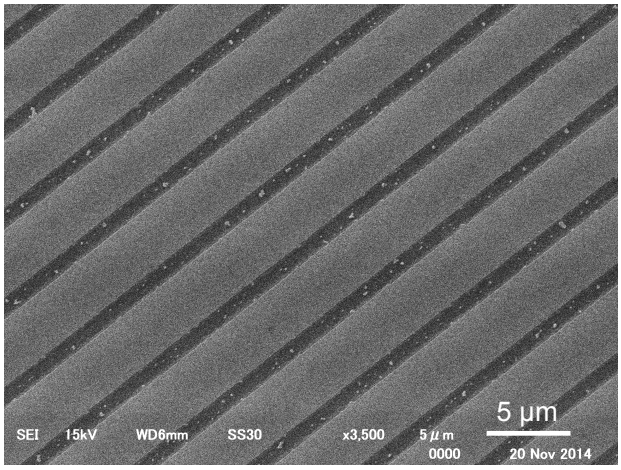

Fig. 105 SEM image of trenches on SiO_2 layer of SiO_2/Si substrate.

sticked to the surface of the substrate beside the trenches. Electrodes were fabricated by indium microsoldering. Indium electrodes was placed avoiding the suspended graphene over trenches, otherwise the the electrodes may damage the suspended graphene (Fig. 106).

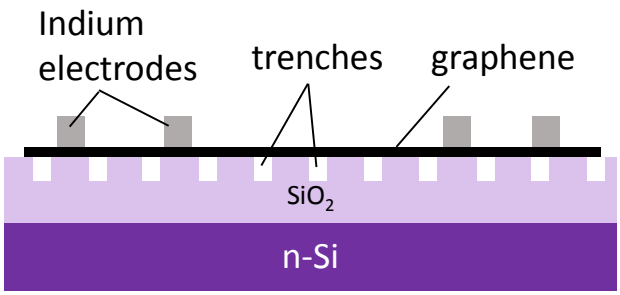

Fig. 106 Cross-section figure of suspended graphene device.

4.3. Results

Images of the suspended graphene device are shown in Fig. 107. Raman spectroscopy showed smaller amount of charged impurities in suspended region. The device is interpreted as a series of suspended and supported graphenes. Resistance change in suspended region is expected to be reflected in the total resistance of whole device.

The suspended graphene device was then installed in the sample cell and cooled down to 1.6 K with liquid helium in glass dewar. Gate voltage dependence of resistance during the cooling is shown in Fig. 108. It showed two peaks, one of which was sharper and located at $V_g = 0$ V and attributed to be the Dirac peak of suspended region, while the other is broader and shifted by hole doping from the substrate. The dirac peak of suspended region yielded the mobility 30,000 $cm^2/V\,s$.

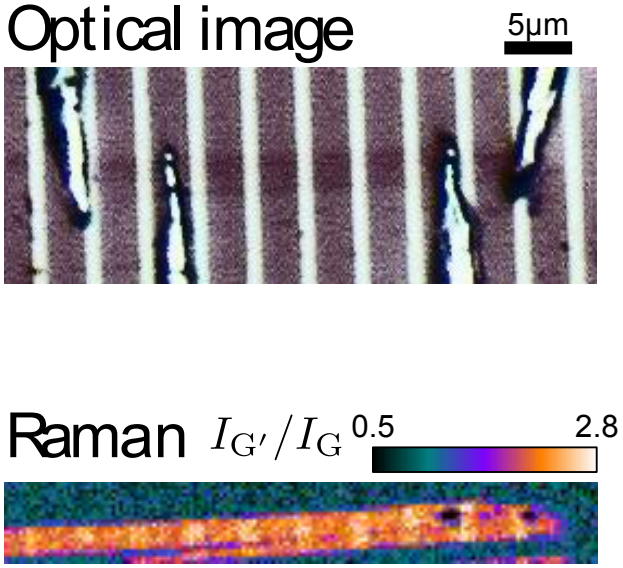

Fig. 107 Upper: Optical microscope image of suspended graphene device. Contrast was exaggerated. Lower: Spacial mapping of ratio of intensities of Raman peaks $I_{G'}/I_G$, which gets smaller if density of carriers is higher.

The sample cell was cooled down with liquid nitrogen in glass dewar. Krypton gas was installed in the sample cell while keeping the temperature at 110 K. The installation was stopped when the pressure reached 7.10 Torr. Then, the temperature was gradually lowered to 50 K in ∼5 hours by pumping the liquid nitrogen. The liquid nitrogen turns into sherbet-like solid nitrogen by pumping and can serve as cryogen which gives the temperature slightly below 50 K. The amount of krypton was chosen so that C+F phase is realized on graphene at around 50 K. As the krypton gas in the sample cell and the adsorbed krypton on graphite are in equilibrium, pressure of the gas P and temperature T obeys August equation (simplified form of Antoine equation) $P = \exp(A - B/T)$ (Fig. 109). Parameters A and B for areal density $\theta = 0.5$ were extracted from experimental data [179]. Here, areal density of $(\sqrt{3} \times \sqrt{3})R30^\circ$ phase on graphite is defined as $\theta = 1$. Krypton with areal density $\theta = 0.5$ shows C+F phase below 85 K on graphite. The temperature is converted to $85 \times 122.7/135.8 = 77$ K on graphene. The krypton installed in the sample cell obeys August equation for graphite and crosses that of graphene, where $\theta = 0.5$ on graphene is realized.

Figure 110 is gate voltage dependence of resistance with and without krypton at 50 K. Resistance at Dirac peak of suspended region was slightly increased after krypton adsorption (23.92 to 23.96 kΩ, 0.17%). Resistance at Dirac peak of suspended region was also increased (27.33 to 27.37 kΩ, 0.15%). After the adsorption, the sample cell was evacuated at 200 K, and cooled down to 50 K to measure the gate voltage dependence of resistance again. The resistance just around the peaks seems to get back to the values before adsorption. These changes may attributed to the effect of krypton adsorption, but judging from whole gate voltage depenedence of resistance (Fig. 111), it is difficult to attribute the

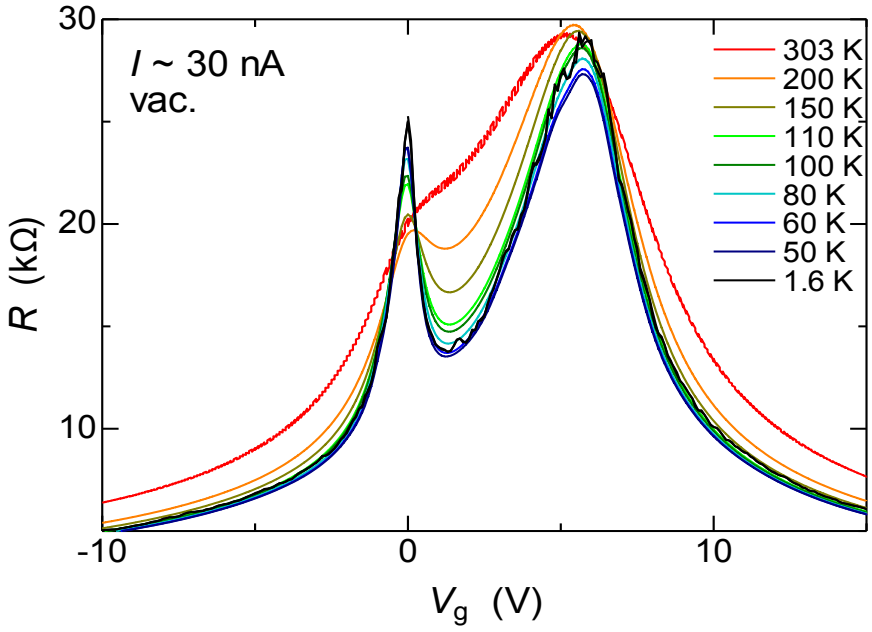

Fig. 108 Gate voltage dependence of resistance of suspended graphene sample with varying temperature

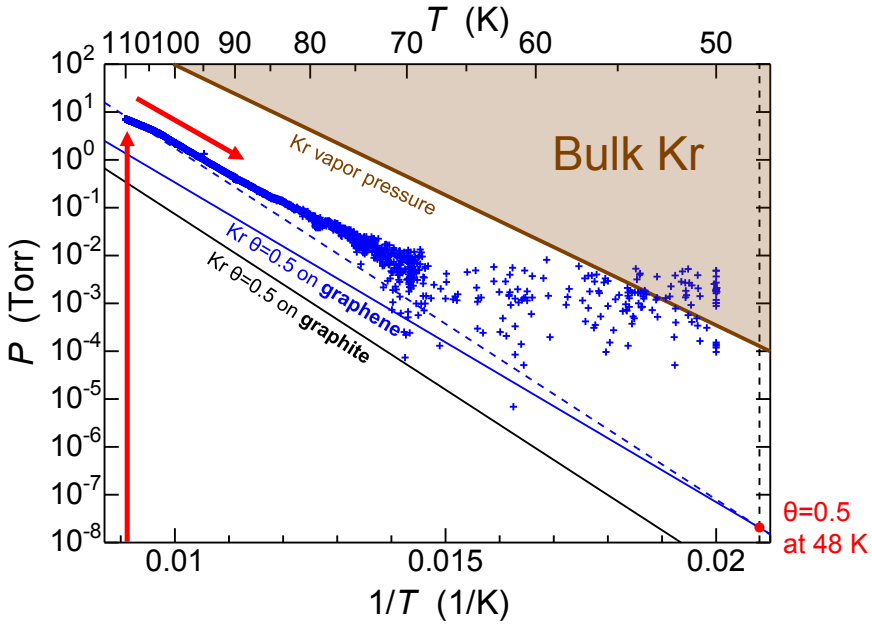

Fig. 109 Procedure of krypton adsorption to suspended graphene. Blue plus symbols are experimental data. Black line is $\theta = 0.5$ on graphite by experimental data [179]. The line is converted to that of graphene (blue line) by method 3 in Section 4.2.2. Dashed blue line is parallel to $\theta = 0.5$ line on graphite and crosses that on graphene at 48 K, where $\theta = 0.5$ on graphene is realized. The pressure of this region is too low to measure within the experimental setup used here.

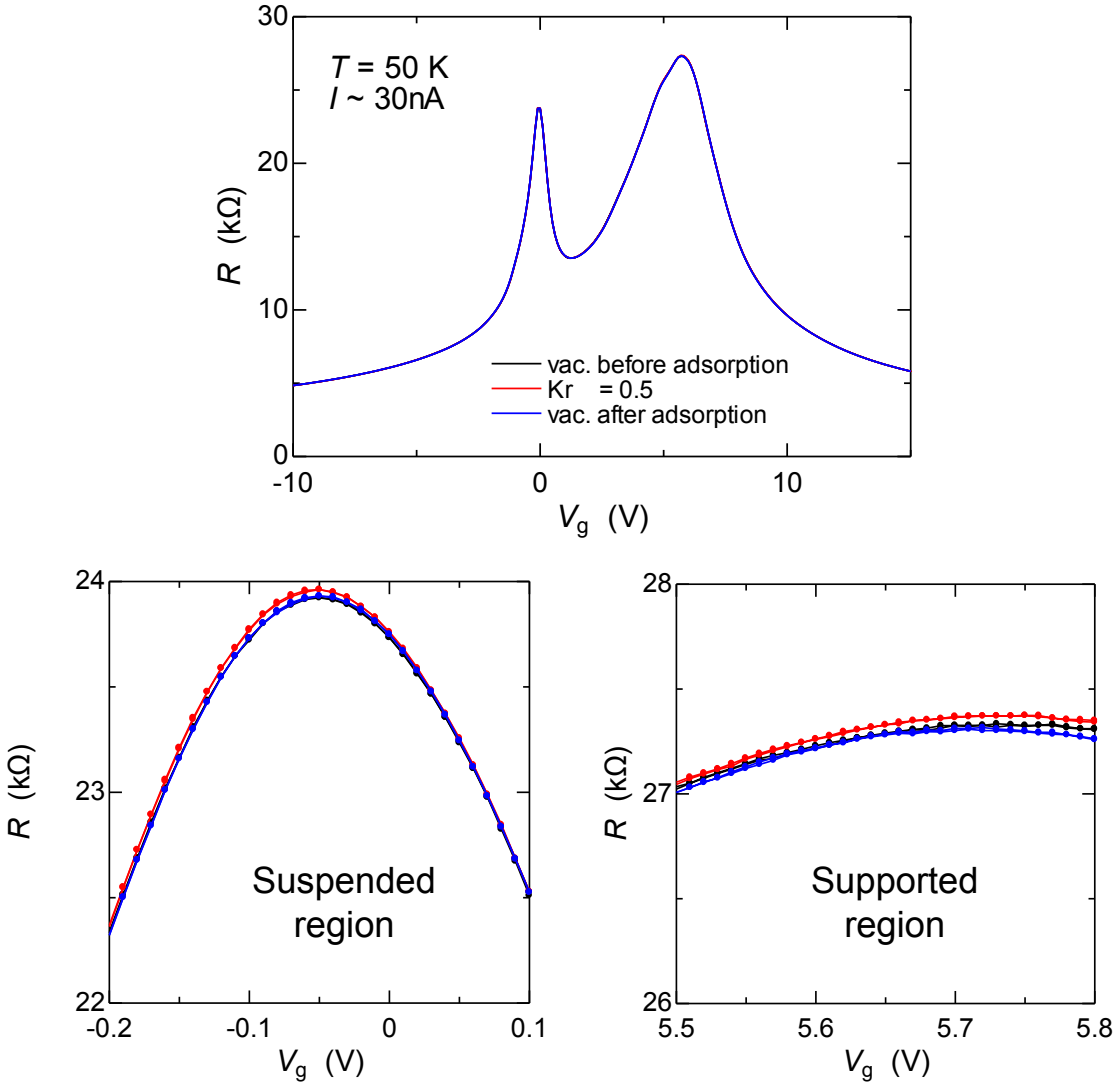

Fig. 110 Gate voltage dependence of resistance of suspended graphene with and without adsorbed krypton.

change to the gap opening. It is rather likely conventional mechanism such as peak shift by carrier doping or carrier scattering. Anyway, the effect of krypton was, even if there it was, very limited.

Through this experiment, the effect of substrate is rejected as a reason why gap opening is not observed. One remaining possibility of the reason is poor cleanliness of the graphene surface. Cleaning by current-induced annealing on this sample was tried, but the sample was broken before the current density reaches reported value [122, 187]. Optimization of current annealing is one task that has to be done. Also, it is effective to perform the experiment at lower temperature to improve the degree of vacuum. Helium is more appropriate to be adsorbed on the sample surface at liquid helium temperature than krypton.

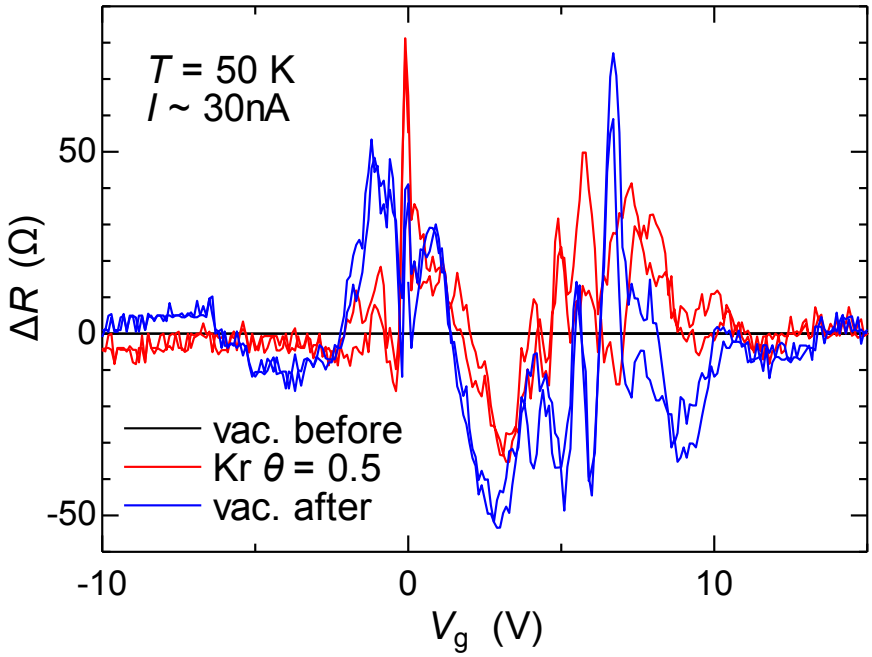

Fig. 111 Difference in gate voltage dependence of resistance of suspended graphene with and without adsorbed krypton.

4.4. Conclusion

A method to open the bandgap of graphene by breaking the symmetry of the honeycomb lattice by adsorbing atoms/molecules with periodicity of $(n\sqrt{3} \times n\sqrt{3})R30^\circ$ has been theoretically proposed. In this study, we attempted to confirm this method with Kr adsorption. It is known that Kr forms a commensurate solid phase with $(\sqrt{3} \times \sqrt{3})R30^\circ$ structure over a wide areal density range on graphite. In order to precisely control the Kr surface density on graphene sample with a small surface area, exfoliated graphite with a large surface area was installed in the sample cell as a reference surface area. To exclude the effect of the substrate, suspended graphene sample was employed. Kr adsorption experiment was carried out at $T = 50$ K to form $(\sqrt{3} \times \sqrt{3})R30^\circ$ superlattice, but no significant change in the transport properties of graphene could be found. Physisorption of Kr may have too small influence on the hopping integral of electrons in graphene.

5. Summary

Properties of pure metallic carbon nanotube network

Based on the recent progress in sorting technique, which enabled collecting a large amount of single electronic type carbon nanotubes (CNT), in this thesis, electronic properties of pure metallic single-walled (SW) and double walled (DW) CNT networks with/without one-dimensional sulfur chain inside were studied through electrical resistance measurements down to $T = 0.3$ K and up to $B = 9$ T.

Surprisingly enough, we found a clear and stable experimental signature that the transport property of the macroscopic random network of DWCNTs is governed by the Tomonaga-Luttinger liquid (TLL) theory in a wide temperature range between 2 and 100 K over nearly two orders of magnitude. The phase decoherence length (Thouless length: L_{Th}) determined from the magnetoresistance measurements revealed that, in that temperature range, L_{Th} is shorter than the mean junction-junction separation (= 100-200 nm) between adjacent CNT bundles and the electron scattering process is presumably determined by the intrinsic TLL theory. This became possible only for such CNT samples with a very high sorting purity (99% metallic CNT). Otherwise, the intra-tube scattering will be dominated by the semiconducting CNT impurity.

We also found the network of metallic SWCNTs with the same sorting purity at least for the outer tube does not show the TLL behavior in the whole temperature range we studied. The result of positive and large magnetoresistance indicates the dominant contribution from the variable range hopping (VRH) term in addition to the small but finite contribution from the 3D WL. The 3D VRH model fits the data better than the 2D one being consistent with the 3D network structure of the sample. Some of the previous reports on unsorted CNT networks show the VRH behaviors [188, 189, 190, 191], and some on pure metallic SWCNT network does the weak localization behavior [69]. Combined with the present result, the difference may be the result of subtle difference in sample preparation and then in the CNT-CNT junction conductivity.

Unlike the previous work where the original 2D VRH behavior of unsorted empty SWCNT was changed to the 3D VRH one by adding sulfur chain in CNTs, no such a big change was observed for the present pure metallic SWCNT. This would be explained by that the metallic SWCNT network already has plenty of conducting paths and no room for sulfur chains to add extra conducting paths.

Magnetic susceptibility measurements revealed the ferromagnetic saturation magnetization in our samples of $\sim 1 \times 10^{-3}$ emu/g at $T = 300$ K, which is much less than those in the previous measurements [99, 100, 97]. The temperature dependence of magnetic susceptibility below 100 K is dominated by a paramagnetic component most likely of su-

perparamagnetism in adsorbed amorphous oxygen molecules. This was supported by the measured hysteresis between data taken during the field cooling and zero-field cooling.

Effects of oxygen and krypton adsorption on the transport properties of graphene

In this research, effects of oxygen molecules and krypton atoms adsorption on electronic properties of monolayer (ML) and bilayer (BL) graphene were studied by measuring the gate voltage dependence of resistance down to $T = 1.6$ K in zero magnetic field. To keep the sample surface clean without being contaminated by liquid residues, the microsoldering method, in which molten indium is put down on the graphene surface directly under the optical microscope, was adopted rather than the typical photolithography technique. For this purpose, the microsoldering apparatus was constructed.

ML and BL graphene samples were exposed to oxygen gas atmosphere to study the hole doping phenomenon and its time evolution. The most important finding here is the fact that the doped carrier (hole) density in BL graphene ($\sim 4 \times 10^{12}$ cm^{-2}) is an order of magnitude larger than that in ML graphene. This is possibly because of higher reactivity at the defects, especially the edges, in BL than ML. The shift of the Dirac point gate voltage ($V_{\rm g}^{\rm DP}$) and the resistance at that voltage ($R^{\rm DP}$) obey the double exponential time dependence with two different time constants both for ML and BL graphene unlike the previous claim of the power law dependence for BL graphene [110]. The two step change suggests the existence of at least two processes in O_2 chemisorption. The fast component of change was not reproduced and decreased after every evacuation of the O_2 gas at $\sim$100°C for $>$ 10 h and therefore must be an irreversible process from weak chemisorption sites to strong ones. On the other hand, the slow component of change was more or less reproducible after the evacuation. This corresponds to the reversible process that has similar efficiency in terms of hole doping to the irreversible process related to the fast process. Theoretical investigations to reveal what kinds of defects in graphene are responsible for these doping sites where O_2 are chemisorbed are highly desirable. The measurements down to $T = 1.6$ K revealed that the transport mechanism is the VRH and the O_2 adsorption tends to shrink the area of localization centers.

Krypton adsorption experiments were also carried out to try to confirm the bandgap opening scenario by symmetry breaking due to gas adsorption forming the $(n\sqrt{3}\times n\sqrt{3})R30^\circ$ superlattice. The suspended graphene was used to exclude the possible substrate effects. Since the exfoliated graphene sample has so small surface area, the exfoliated graphite stack with the large surface area of $\sim$40 m^2 was installed inside the sample cell to enable the precise control of the areal density of krypton adsorbent. Kr, the largest noble atom which form is known to form the $(\sqrt{3} \times \sqrt{3})R30^\circ$ superstructure on a graphite surface in a wide density range at temperatures below 85 K. We introduced the controlled amount of Kr gas into the sample cell at 110 K and the cell was cooled down to 50 K. However, no change of the transport property induced by the Kr adsorption was observed. Possible explanations for the absence of any effects are (1) the surface of the graphene sample was not clean enough to form the $(\sqrt{3} \times \sqrt{3})R30^\circ$ structure (2) Kr physisorption does not produce large enough change in the electron hopping integral in graphene.

A. Measuring small sample resistances with large contact resistances

While measuring transport property of buckypaper samples with indium electrodes, strange behavior was observed both with AC and DC methods (Fig. A1). The resistance

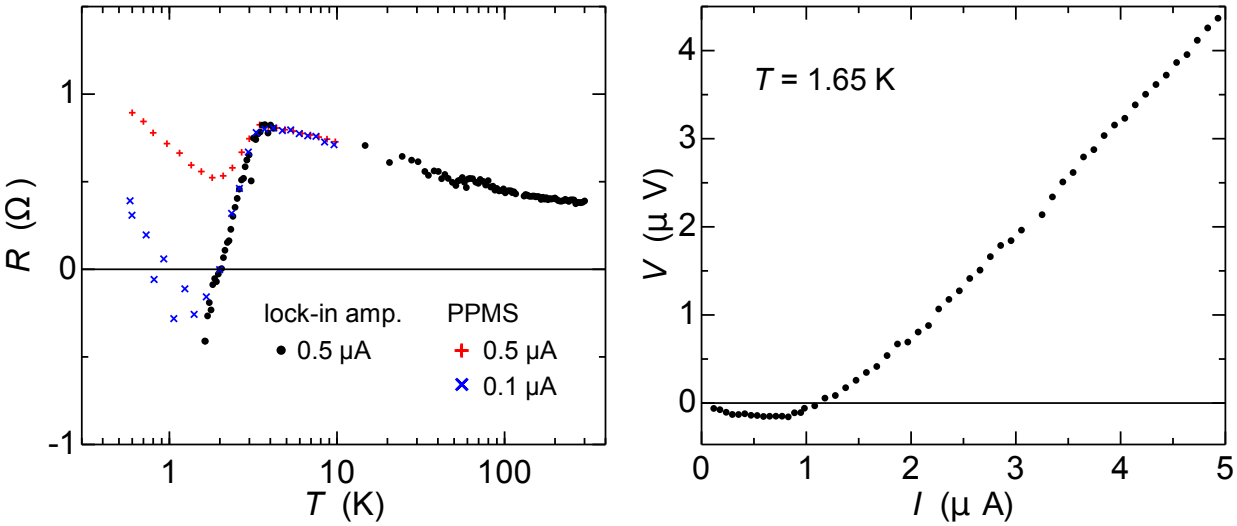

Fig. A1 Strange behavior observed while measuring transport property of buckypaper with indium electrodes. Left: temperature dependencies of resistance of S@DWCNT/In-1 taken with a homemade AC resistance bridge and PPMS. The resistance drops below T_c (=3.4 K) of indium even down to negative values. Right: I-V characteristics at T = 1.65 K measured by the DC method. Apparently negative voltages were observed below about 1 μA.

showed a sharp drop below 3.4 K, which is the superconducting transition temperature (T_c) of indium. Even apparently negative resistance was observed at lower temperatures. The apparently negative resistance was also observed in I-V characteristics. The phenomenon was first supposed to be intrinsic to the sample, but later found to be caused by an instrumental problem. It happens when contact resistances between the sample and electrodes are much higher than sample resistance and there exists a large difference in the contact resistances for four terminals.

Figure A2(a) is a block diagram of the homemade AC resistance bridge using a lock-in amplifier, where the contact resistances and internal resistances of the amplifier are explicitly shown. The input lines of the lock-in amplifier are connected to the ground through

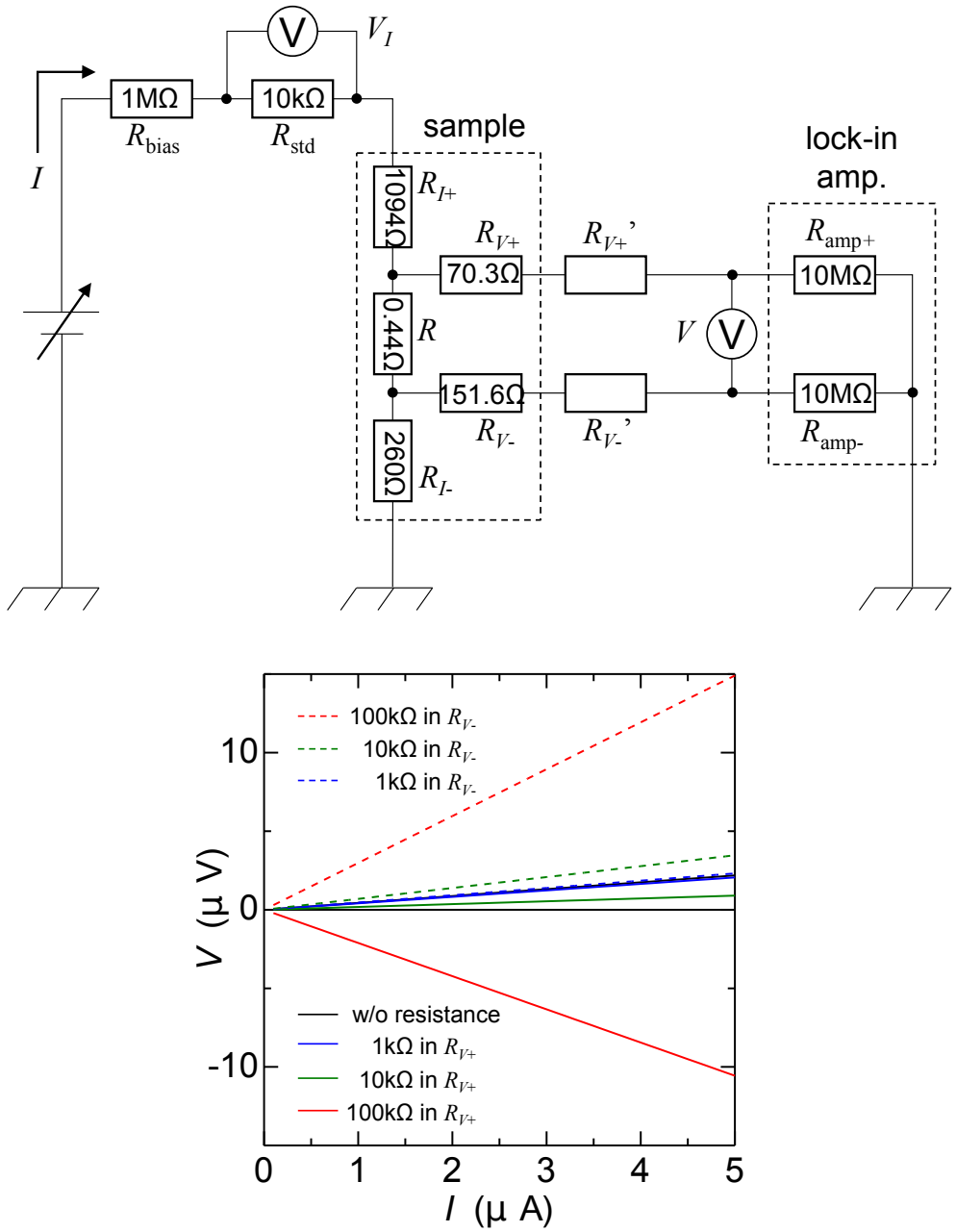

Fig. A2 Simulation of the electric system used in transport measurements including lock-in amplifier. top: Circuit model used in the simulation. bottom: Resulting I-V characteristics for several different contact resistances. Apparently negative voltage appears when contact resistance at V- is large.

internal high impedances, restricting current flow through them very small. However, if the contact resistances (R_{V+}, R_{V-}) are large enough and the sample resistance (R) is small enough, voltage drops at the contact resistances make measured voltages (V) differ from voltage drops across the sample (V_R) which we want to measure. To check this, known

resistances (R'_{V+}, R'_{V-}) are added in series to R_{V+} and R_{V-} as shown in Fig. A2(a), and resulting I-V curves were measured. The results are shown in Fig. A2(b). In the case of $(R_{V+} + R'_{V+}) \gg (R_{V-} + R'_{V-})$, apparently negative resistance is produced.

We also disconnected lock-in amplifier to be isolated from the ground and kept other parts of the measuring system unchanged. The resultant I-V curve is shown in Fig. A3. In

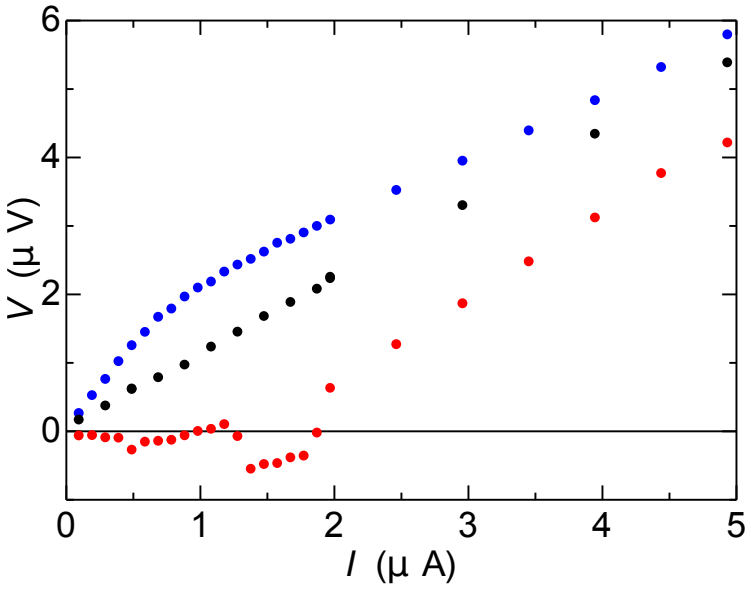

Fig. A3 I-V characteristics measured with three different grounding configurations. With the original configuration (red circles) where the lock-in amplifiers are connected to the ground, apparently negative voltage appeared. When the lock-in amplifier was disconnected and isolated from the ground (black circles), linear I-V characteristics appeared. When some instruments in the system other than lock in amplifier was connected to the ground (blue circles), yet another strange behavior appeared.

this case, linear I-V characteristics appeared. This result confirms that apparently negative resistance was caused by the current through the lock-in amplifier into the ground. Yet another configuration was tried; some instruments in the measurement system other than the lock-in amplifier was connected to the ground. This time the I-V curve became convex upward. This shows that if the sample resistance is small and lead contact resistances are large enough, apparent resistance of the sample can be rather sensitive to the configuration of the measurement system, especially grounding.

The curious resistance drop below 3.4 K may be related to rapid suppression of the thermal conductance of the indium electrodes below T_c. The contact resistances much higher than the sample resistance cause higher Joule heating at the contacts. Above T_c, on the other hand, indium electrodes in the normal state are supposed to work as good thermal links to refrigerant. Accompanied by large T-dependencies of the contact resistances, local Joule heating may enhance imbalance of the contact resistances and produce an erroneous negative voltage. To confirm this explanation, heat exchange gas was introduced into the sample cell. The exchange gas is expected to assist the heat drain and restore the

temperature homogeneity. The result of such an experiment is shown in Fig. A4. As

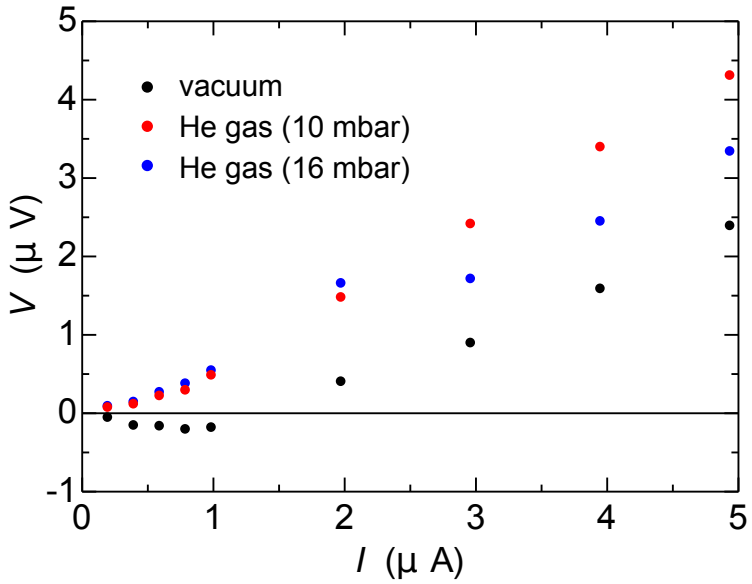

Fig. A4 Suppression of the apparently negative voltage problem by introduction of helium heat exchange gas. The data are taken in vacuum(black), with the exchange gas of 10 mbar (red) and 16 mbar (blue) in pressure.

pressure of the exchange gas is increased, the I-V curve got closer to linear. This result supports the hypothesis that the appearance of the rapid drop and the negative value of resistance is caused by local Joule heating at the contacts.

The same situation happens with the PPMS of Quantum Design, Inc. which has a slightly different measuring circuit from that of our homemade AC resistance bridge as shown in Fig. A5(a). The result of simulation for the PPMS measurement is shown in Fig. A5 on the right [192]. Apparently negative resistance is obtained as the excitation current decreases below 10 μA. While the sample resistance is eventually 1 Ω, the circuit erroneously detects a negative resistance as low as -80 Ω.

In conclusion, to avoid these problems, (1) care must be taken to ground configuration of measurement system even for commercial systems such as PPMS and (2) contact resistances should be as low as possible.

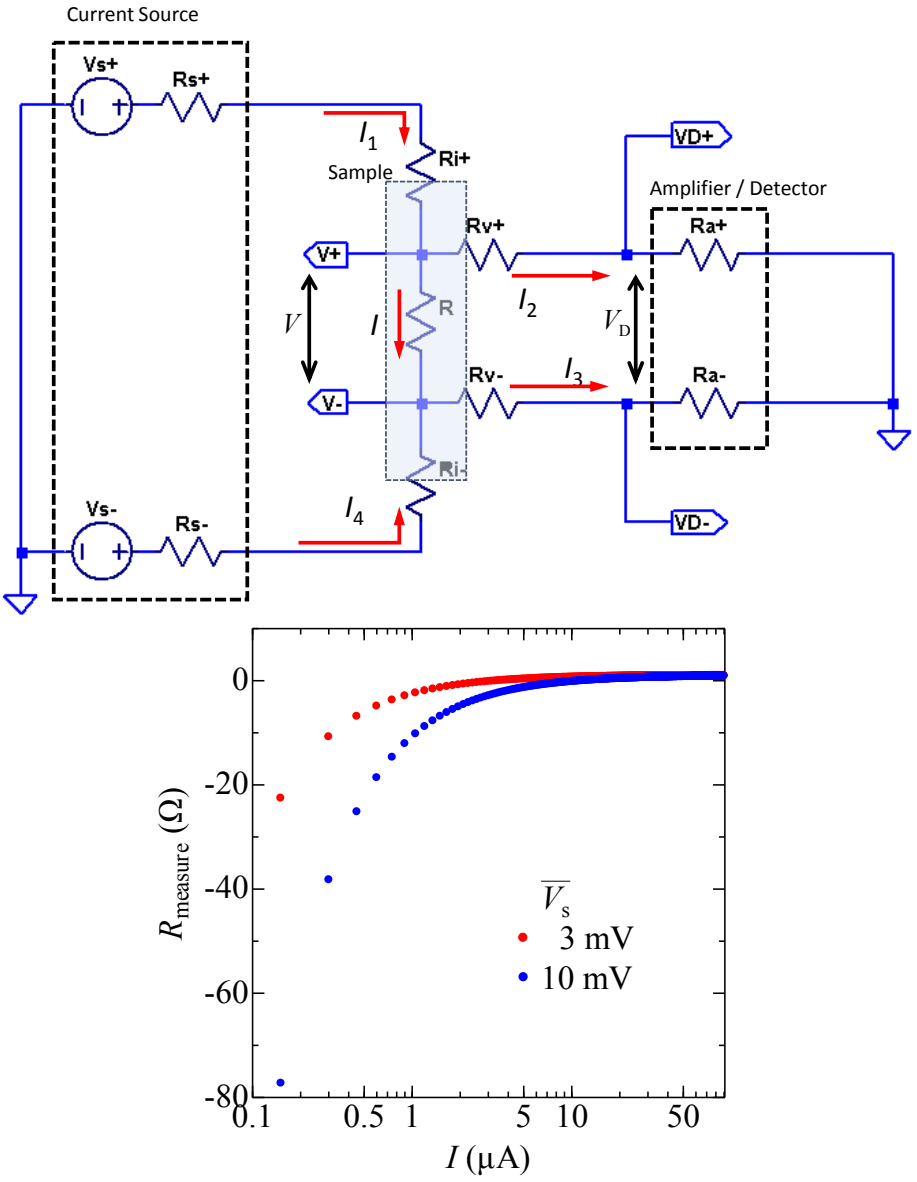

Fig. A5 Simulation of the electric system used in transport measurements with PPMS. top: Circuit model used in the simulation. bottom: Excitation current vs. resistance. An apparently negative resistance below -80Ω develops as the excitation current decreases below 10 μA.

B. Magnetic susceptibility measurement in case magnetizations of sample and sample holder are comparable in magnitude

Figure B1 explains the measuring concept of the magnetic property measurement system (MPMS) [94]. The sample is moved up and down through the pickup coil along the coil axis

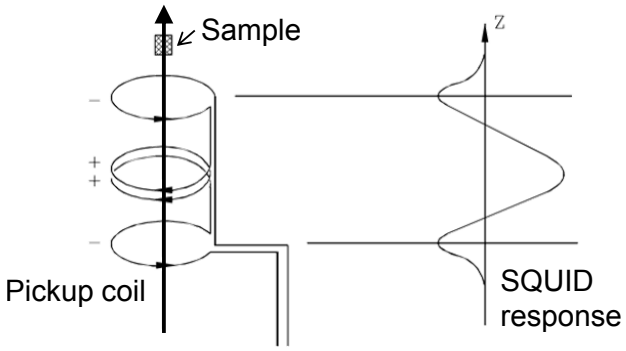

Fig. B1 Measuring concept of MPMS. The sample is transported through the pickup coil, and the position dependence of response is fitted by a function to obtain magnetic susceptibility.

(Z axis), and the resultant induced voltage, the response signal (S), is detected by a superconducting quantum interference device (SQUID). The position dependent response signal $S(Z)$ is fitted by the following function to determine magnetization of the sample [193]:

$$S(Z) = X_1 + X_2 Z + X_3 \left\{ 2\left[R^2 + (Z + X_4)^2\right]^{-3/2} - \left[R^2 + (\Lambda + (Z + X_4))^2\right]^{-3/2} - \left[R^2 + (-\Lambda + (Z + X_4))^2\right]^{-3/2} \right\}, \tag{B1}$$

where X_1,X_2,X_3 and X_4 are fitting parameters and R, Λ are equipment-specific constants. Here, the sample is assumed to be a point magnetic dipole.

Figure B2 shows an actual sample and sample holder setup in this work. A small straw fixing piece was used to hold the buckypaper sample. And the fixing piece with the sample

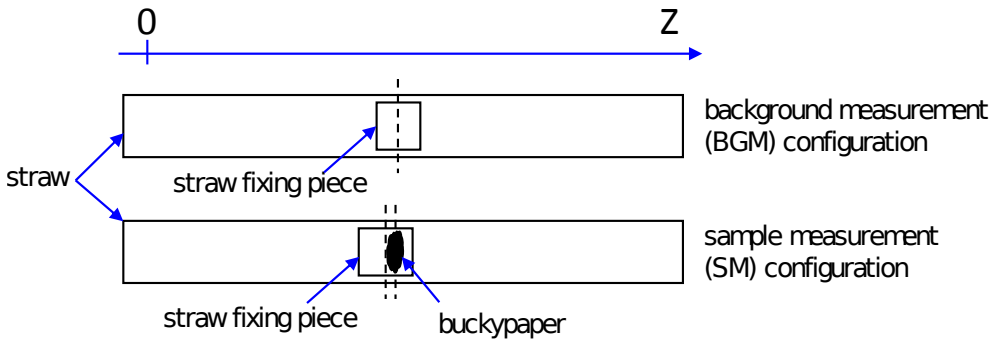

Fig. B2 Positions of the magnetic centers ($Z_{\rm mc}$) indicated by the vertical dashed lines in the two measurement configurations; (upper) the background measurement (BGM) configuration containing only the straw segment, (lower) the sample measurement (SM) configuration containing the same straw segment and the buckypaper sample. The positions of $Z_{\rm mc}$ can be changed measurement to measurement, and in the SM configuration, when the $Z_{\rm mc}$ of straw segment is not aligned to that of buckypaper, the sample has two magnetic centers. The misalignment leads to the failure of fitting of position dependence of response.

is inserted into a long straw which is long enough compared with the moving distance of the sample in the pickup coil. Thus the sample holder consists of the small straw fixing piece and the long straw, both of which are made of polypropylene. The sample holder has a diamagnetic response comparable to that of the buckypaper sample. Therefore, the background contribution from the sample holder must be carefully subtracted from the total response signal to obtain the true magnetization of buckypaper particularly in case magnetizations of the sample holder and sample itself are comparable in magnitude. In principle, the exact location of the fixing piece can be shifted a little in two independent measurements with and without the buckypaper sample, i.e., the misalignment problem. In addition, the location of the magnetic center ($Z_{\rm mc}$) can be different between the fixing piece and the sample, i.e., the multiple magnetic center problem. In the latter case, even fitting the $S(Z)$ data to Eq. (B1) fails.

Figure B3 shows a typical example of response signals $S(Z)$ with those problems. The red solid line is the signal obtained in the background measurement (BGM) configuration without the buckypaper sample (the upper configuration in Fig. B2), while the black solid line is that obtained in the sample measurement (SM) configuration with the sample (the lower configuration in Fig. B2). The software of MPMS simply subtract the former from the latter, without considering the unavoidable misalignment and multiple magnetic center problems, yielding the blue dashed line as the as-measured sample response signal. Then the software yields an erroneous magnetization with jumps near $m \approx 0$ shown in Fig. B4 by fitting the as-measured signal to Eq. (B1).

How can we correct the problems? In our case, fortunately, the signal from the buckypaper can safely be assumed as negligibly small compared to that of the sample holder at room temperature as seen in Fig. B3. Therefore, we could reliably determine the shift of $Z_{\rm mc}$ of the straw fixing piece between the two sequences as -0.08 cm as indicated by the green arrows in Fig. B3. Then the shifted response signal (the black dashed line) is subtracted

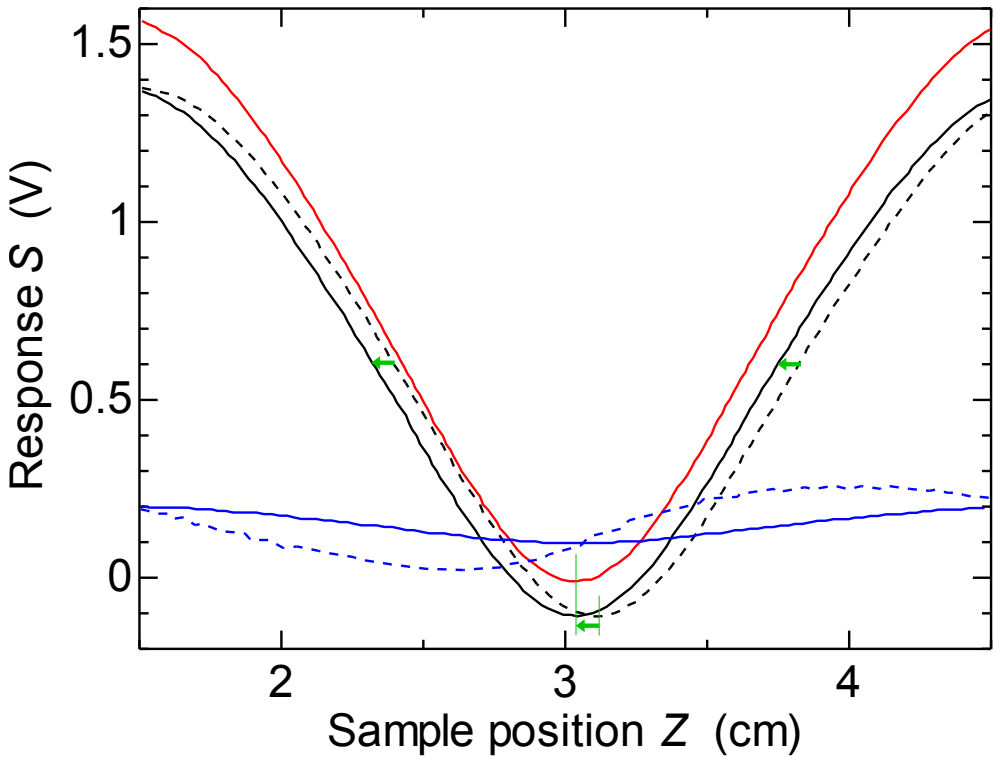

Fig. B3 Procedure to correct for multiple magnetic center problem. The red solid line is the response signal obtained in the SM configuration shown in Fig. B2, and the black solid line is that in the BGM configuration. The PPMS software yields automatically the blue sold line, by subtracting the latter from the former, as as-measured response signal for the buckypaper sample and a wrong magnetization value, by fitting it to Eq. (B1). On the other hand, if we subtract the black dashed line which is obtained by shifting the Z coordinate of the black solid line by -0.08 cm to correct the magnetic center shifting (green arrows) and then subtract it from the red solid line, we obtain the blue dashed line. Such an appropriate correction gives a smooth T variation of m as shown in Fig. B5.

from the data in the SM sequence (red solid line). The resultant signal for the buckypaper sample has a normal variation as a function of Z as indicated by the blue dashed line in Fig. B3. This can properly be fitted to Eq. (B1) giving the corrected magnetization data without the anomalous jumps (see Fig. B5).

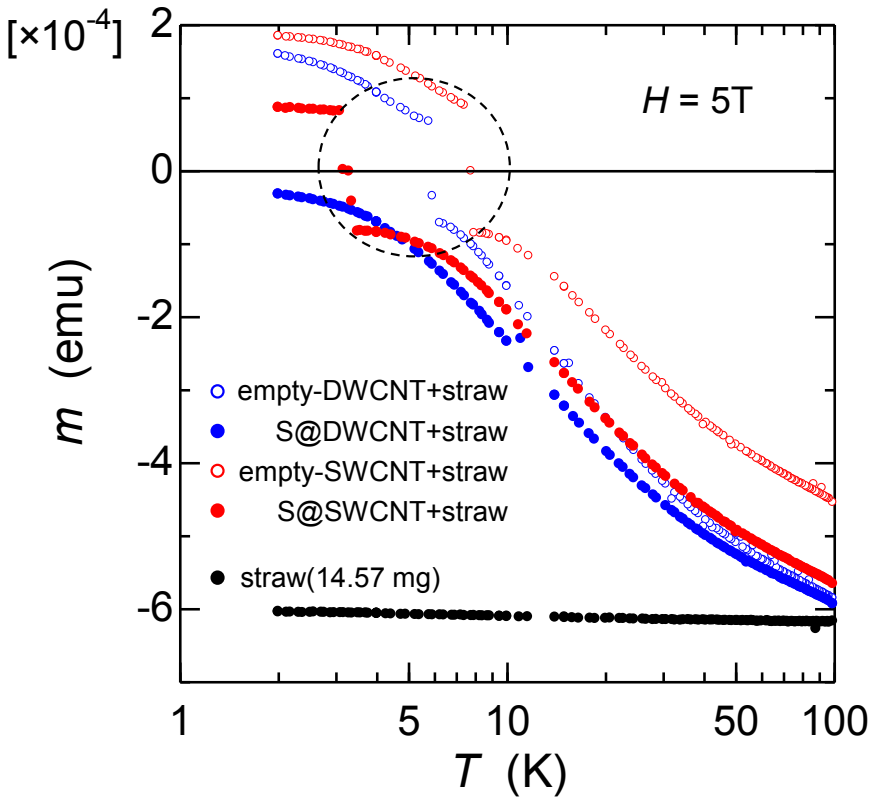

Fig. B4 Strange behavior in magnetization data at $B = 5$ T of buckypaper samples with jumps near $m = 0$ caused by the misalignment and multiple magnetic center problems (see text for more details).

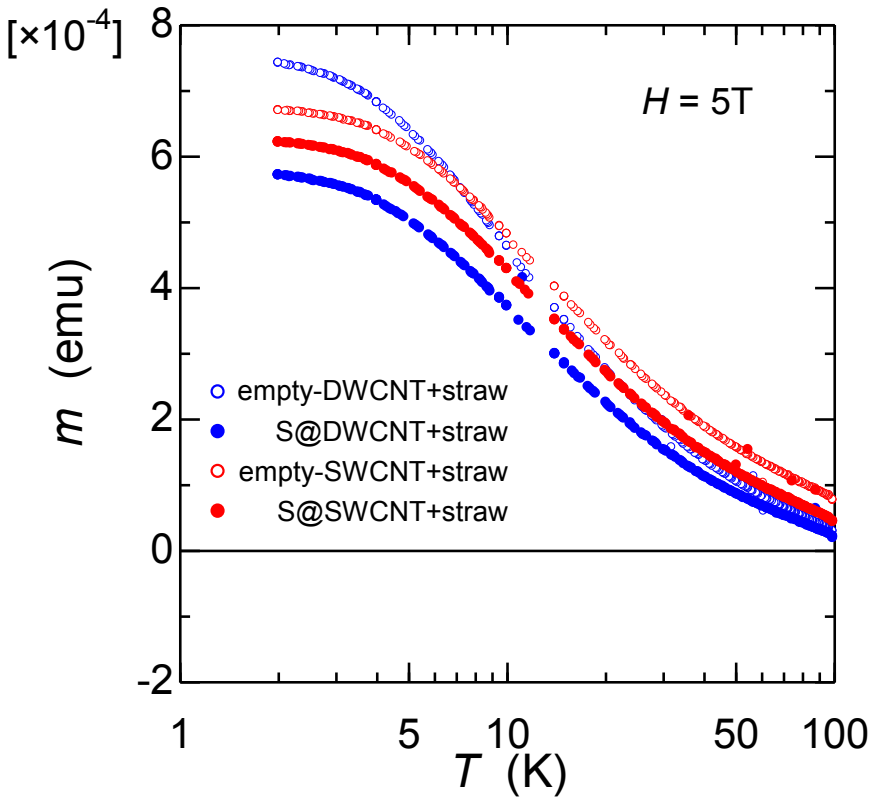

Fig. B5 Magnetization obtained by correcting the as-measured data shown in Fig. B4 with the strange jumps at T = 3-8 K. The correction procedure is described in detail in the main text.

C. Photolithography

Process of photolithography was performed in the clean booth in our laboratory. The procedure is shown below (Fig. C1).

1. Resist coating

   Photoresist S1813 was dropped on sample substrate and the substrate was rotated with a spin coater [194] at 6000 rpm for 40 seconds to form the uniform resist layer. Then, it was baked at 90°C for 5 minutes for curing, followed by natural cooling. Subsequent processes till after development was done under yellow lamp to avoid unwanted exposure.

2. Exposure

   The substrate was aligned with the photomask (Fig. C2) and then firmly contacted. It was then exposed to ultraviolet light from the mercury lamp for 55 seconds to expose the resist layer with the pattern of photomask.

3. Undercut structure formation

   To make the liftoff easier, undercut structure was formed along the edge of unexposed region of the resist. The substrate was immersed in dichlorobenzene for 1 minute and then dried in constant-temperature oven.

4. Development

   The substrate was immersed in 1:5 mixture of developer S351 and distilled water at 20°C for 50 seconds to remove the exposed region of the resist. It was then immersed in distilled water for about 2 minutes to stop the development completely.

5. Vapor deposition

   Metal for electrodes was vapor-deposited on the sample substrate surface in vacuum of 10^{-6}~10^{-7} Torr in high-vacuum deposition apparatus. To obtain good contact, it is common to deposit such metals as chromium, titanium or paradium as underlayment before deposition of gold. In this research, 10 nm of titanium was deposited followed by 50 nm of gold to make the samples. Both titanium and gold were evaporated using electron beam.

6. Liftoff

   The substrate was immersed in acetone for a long time to dissolve the resist and remove the metal on it. Metal in the region exposed to ultraviolet light remains, resulting in the electrode structure.

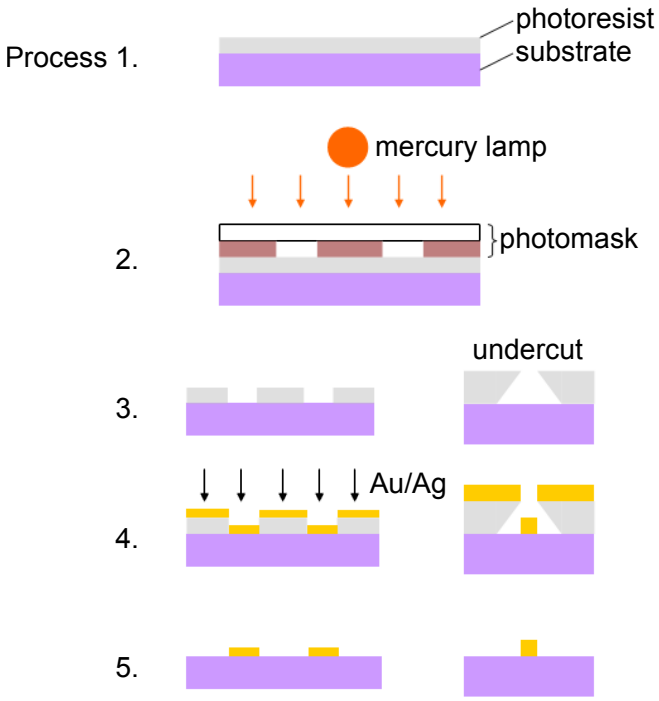

Fig. C1 Procedure of photolithography [119]

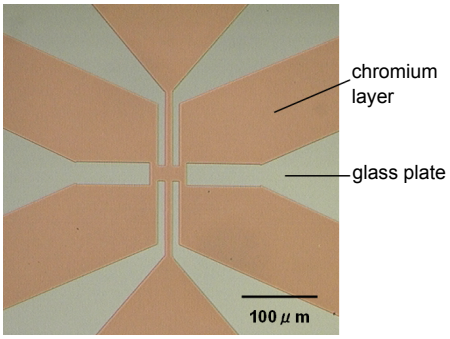

Fig. C2 An example of photomask [119]

Acknowledgments

I would like to express my gratitude to the people who helped me in this research.

Prof. Hiroshi Fukuyama, the thesis adviser, took care of me from the decision of the research theme and gave me guidance on how to proceed my research, with a passion for the quality.

Dr. Tomohiro Matsui, an assistant professor, taught me the technical matters and the knowledge necessary for advancing research kindly all the time.

Prof. Toshihiko Fujimori and Prof. Katsumi Kaneko of Shinshu University, who are collaborators of our research on carbon nanotube, provided me the buckypaper samples. I learned a lot of insights of chemistry of carbon nanotubes, and am grateful of fruitful discussions with them.

I appreciate Dr. Ryo Toda who taught me many experimental techniques of measurements using the PPMS and MPMS, and made many illuminating discussions with me, particularly about the seemingly negative resistance shown in Appendix A.

Sotaro Sugimoto is a collaborator in the early phase of buckypaper study. He helped me with some of the buckypaper measurements and greatly speeded up my research.

The equipment for microsoldering was constructed by Jan Raphael Bindel, who stayed in our laboratory for one year, with Prof. Matsui. Dr. Sachiko Nakamura kindly allowed me to measure the samples with the dry dilution refrigerator which she has been operating. André Amend helped me with some of the buckypaper measurements.

Masahiro Kamada and Youhei Kono helped me with the earlier phase of my research on graphene, and the gas handling system used in this research was constructed by Yuya Kubota and Nobuhiro Shimizu, when they were undergraduate students. Dr. Hiroki Shioya in Tarucha-Yamamoto laboratory taught me tricks and tips for the exfoliation of graphene.

Ryuji Nakamura, Katsuyoshi Ogawa and Kita Kazuma who are the members of this laboratory and Dr. Daisuke Sato, Kouta Matsui, Takayuki Nakajima and Hideki Sato who had already left this laboratory gave me various advices and made the life in the laboratory enjoyable.

Masaki Nishioka in Office for Mental Health Support and Mariko Enomoto in Student Counseling Center greatly helped me keep up my mental stability.

Finally, I would like to express my gratitude to Iwatare Scholarship Association and Oshima Scholarship Association for financially supporting my research activities at the graduate course, and to the Cryogenic Research Center (CRC) of the University of Tokyo for supplying liquid helium and for allowing me to use their PPMS and MPMS for joint-use.

References

[1] M.-F. Yu, O. Lourie, M. J. Dyer, K. Moloni, T. F. Kelly, and R. S. Ruoff, *Strength and breaking mechanism of multiwalled carbon nanotubes under tensile load*, Science **287**, 637–640 (2000).

[2] Л. В. Радушкевич and В. М. Лукьянович, *О структуре углерода, образующегося при термическом разложении окиси углерода на железном контакте*, Журнал Физической химии **26**, 88–95 (1952).

[3] M. Monthioux and V. L. Kuznetsov, *Who should be given the credit for the discovery of carbon nanotubes?*, Carbon **44**, 1621–1623 (2006).

[4] S. Iijima, *Helical microtubules of graphitic carbon*, Nature **354**, 56–58 (1991).

[5] A. Oberlin, M. Endo, and T. Koyama, *Filamentous growth of carbon through benzene decomposition*, Journal of Crystal Growth **32**, 335–349 (1976).

[6] R. Saito, M. Fujita, G. Dresselhaus, and u. M. Dresselhaus, *Electronic structure of chiral graphene tubules*, Applied Physics Letters **60**, 2204–2206 (1992).

[7] L. Van Hove, *The occurrence of singularities in the elastic frequency distribution of a crystal*, Physical Review **89**, 1189 (1953).

[8] H. Kataura, Y. Kumazawa, Y. Maniwa, I. Umezu, S. Suzuki, Y. Ohtsuka, and Y. Achiba, *Optical properties of single-wall carbon nanotubes*, Synthetic Metals **103**, 2555–2558 (1999).

[9] A. Eatemadi, H. Daraee, H. Karimkhanloo, M. Kouhi, N. Zarghami, A. Akbarzadeh, M. Abasi, Y. Hanifehpour, and S. Joo, *Carbon nanotubes: properties, synthesis, purification, and medical applications.*, Nanoscale Research Letters **9**, 393–393 (2013).

[10] S. Iijima and T. Ichihashi, *Single-shell carbon nanotubes of 1-nm diameter*, Nature **363**, 603–605 (1993).

[11] D. Bethune, C. Klang, M. de Vries, G. Gorman, R. Savoy, J. Vazquez, and R. Beyers, *Cobalt-catalysed growth of carbon nanotubes with single-atomic-layer walls*, Nature **363**, 605–607 (1993).

[12] M. José-Yacamán, M. Miki-Yoshida, L. Rendon, and J. Santiesteban, *Catalytic growth of carbon microtubules with fullerene structure*, Applied Physics Letters **62**, 202–204 (1993).

[13] K. Hata, D. N. Futaba, K. Mizuno, T. Namai, M. Yumura, and S. Iijima, *Water-assisted highly efficient synthesis of impurity-free single-walled carbon nanotubes*, Science **306**, 1362–1364 (2004).

[14] A. Meyer-Plath, G. Orts-Gil, S. Petrov, F. Oleszak, H.-E. Maneck, I. Dörfel, O. Haase, S. Richter, and R. Mach, *Plasma-thermal purification and annealing of carbon nanotubes*, Carbon **50**, 3934–3942 (2012).

[15] D. Nishide, Y. Miyata, K. Yanagi, T. Tanaka, and H. Kataura, *Effective separation of carbon nanotubes and metal particles from pristine raw soot by ultracentrifugation*, Japanese Journal of Applied Physics **48**, 015004 (2009).

[16] J. Hutchison, N. Kiselev, E. Krinichnaya, A. Krestinin, R. Loutfy, A. Morawsky, V. Muradyan, E. Obraztsova, J. Sloan, S. Terekhov *et al.*, *Double-walled carbon nanotubes fabricated by a hydrogen arc discharge method*, Carbon **39**, 761–770 (2001).

[17] M. Endo, H. Muramatsu, T. Hayashi, Y. Kim, M. Terrones, and M. Dresselhaus, Nanotechnology: 'Buckypaper' from coaxial nanotubes, Nature **433**, 476–476 (2005).

[18] B. W. Smith, M. Monthioux, and D. E. Luzzi, *Encapsulated C60 in carbon nanotubes*, Nature **396**, 323–324 (1998).

[19] B. W. Smith and D. E. Luzzi, *Formation mechanism of fullerene peapods and coaxial tubes: a path to large scale synthesis*, Chemical Physics Letters **321**, 169–174 (2000).

[20] K. Hirahara, K. Suenaga, S. Bandow, H. Kato, T. Okazaki, H. Shinohara, and S. Iijima, *One-dimensional metallofullerene crystal generated inside single-walled carbon nanotubes*, Physical Review Letters **85**, 5384 (2000).

[21] D. Tománek and R. J. Enbody, *Science and application of nanotubes*, Springer Science & Business Media (2000).

[22] L. Girifalco, M. Hodak, and R. S. Lee, *Carbon nanotubes, buckyballs, ropes, and a universal graphitic potential*, Physical Review B **62**, 13104 (2000).

[23] J. Zhao, Y. Jia, N. Wei, and T. Rabczuk, *Binding energy and mechanical stability of two parallel and crossing carbon nanotubes*, Proceedings of the Royal Society of London Series A **471**, 20150229 (2015).

[24] M. S. Arnold, A. A. Green, J. F. Hulvat, S. I. Stupp, and M. C. Hersam, *Sorting carbon nanotubes by electronic structure using density differentiation*, Nature Nanotechnology **1**, 60–65 (2006).

[25] P. Zhao, E. Einarsson, R. Xiang, Y. Murakami, and S. Maruyama, *Controllable expansion of single-walled carbon nanotube dispersions using density gradient ultracentrifugation*, The Journal of Physical Chemistry C **114**, 4831–4834 (2010).

[26] T. Tanaka, H. Jin, Y. Miyata, S. Fujii, H. Suga, Y. Naitoh, T. Minari, T. Miyadera, K. Tsukagoshi, and H. Kataura, *Simple and scalable gel-based separation of metallic and semiconducting carbon nanotubes*, Nano Letters **9**, 1497–1500 (2009).

[27] G. Duesberg, J. Muster, V. Krstic, M. Burghard, and S. Roth, *Chromatographic size separation of single-wall carbon nanotubes*, Applied Physics A: Materials Science & Processing **67**, 117–119 (1998).

[28] K. Moshammer, F. Hennrich, and M. M. Kappes, *Selective suspension in aqueous sodium dodecyl sulfate according to electronic structure type allows simple separation of metallic from semiconducting single-walled carbon nanotubes*, Nano Research **2**, 599–606 (2009).

[29] M. Zheng and E. D. Semke, *Enrichment of single chirality carbon nanotubes*, Journal of the American Chemical Society **129**, 6084–6085 (2007).

[30] X. Tu, S. Manohar, A. Jagota, and M. Zheng, *DNA sequence motifs for structure-specific recognition and separation of carbon nanotubes*, Nature **460**, 250–253 (2009).

[31] S. Brown, A. Jorio, P. Corio, M. Dresselhaus, G. Dresselhaus, R. Saito, and K. Kneipp, *Origin of the Breit-Wigner-Fano lineshape of the tangential G-band feature of metallic carbon nanotubes*, Physical Review B **63**, 155414 (2001).

[32] P. Wallace, *The band theory of graphite*, Physical Review **71**, 622 (1947).

[33] K. Novoselov, A. Geim, S. Morozov, D. Jiang, Y. Zhang, S. Dubonos, I. Grigorieva, and A. Firsov, *Electric field effect in atomically thin carbon films*, Science **306**, 666 (2004).

[34] N. Tombros, C. Jozsa, M. Popinciuc, H. Jonkman, and B. Van Wees, *Electronic spin transport and spin precession in single graphene layers at room temperature*, Nature **448**, 571–574 (2007).

[35] A. Neto, F. Guinea, N. Peres, K. Novoselov, and A. Geim, *The electronic properties of graphene*, Reviews of Modern Physics **81**, 109 (2009).

[36] K. Nagashio, T. Nishimura, K. Kita, and A. Toriumi, *Systematic Investigation of the Intrinsic Channel Properties and Contact Resistance of Monolayer and Multilayer Graphene Field-Effect Transistor*, Japanese Journal of Applied Physics **49**, 051304 (2010).

[37] S.-i. Tomonaga, *Remarks on Bloch's method of sound waves applied to many-fermion problems*, Progress of Theoretical Physics **5**, 544–569 (1950).

[38] J. Luttinger, *An exactly soluble model of a many-fermion system*, Journal of Mathematical Physics **4**, 1154–1162 (1963).

[39] T. Giamarchi, *Quantum Physics in One Dimension*, International Series of Monographs on Physics, Clarendon Press (2003).

[40] F. Haldane, *'Luttinger liquid theory'of one-dimensional quantum fluids. I. Properties of the Luttinger model and their extension to the general 1D interacting spinless Fermi gas*, Journal of Physics C: Solid State Physics **14**, 2585 (1981).

[41] F. Milliken, C. Umbach, and R. Webb, *Indications of a Luttinger liquid in the fractional quantum Hall regime*, Solid State Communications **97**, 309–313 (1996).

[42] S. Tarucha, T. Honda, and T. Saku, *Reduction of quantized conductance at low temperatures observed in 2 to 10*
mum-long quantum wires, Solid State Communications **94**, 413–418 (1995).

[43] C. Kane, L. Balents, and M. P. Fisher, *Coulomb interactions and mesoscopic effects in carbon nanotubes*, Physical Review Letters **79**, 5086 (1997).

[44] R. Egger and A. O. Gogolin, *Effective low-energy theory for correlated carbon nanotubes*, Physical Review Letters **79**, 5082 (1997).

[45] M. Bockrath, D. H. Cobden, J. Lu, A. G. Rinzler, R. E. Smalley, L. Balents, and P. L. McEuen, *Luttinger-liquid behaviour in carbon nanotubes*, Nature **397**, 598–601 (1999).

[46] M. Bockrath, D. H. Cobden, P. L. McEuen, N. G. Chopra, A. Zettl, A. Thess, and R. E. Smalley, *Single-electron transport in ropes of carbon nanotubes*, Science **275**, 1922–1925 (1997).

[47] S. J. Tans, M. H. Devoret, H. Dai, A. Thess, R. E. Smalley, L. Geerligs, and C. Dekker, *Individual single-wall carbon nanotubes as quantum wires*, Nature **386**, 474–477 (1997).

[48] R. Egger, *Luttinger liquid behavior in multiwall carbon nanotubes*, Physical Review Letters **83**, 5547 (1999).

[49] M. P. Fisher and L. I. Glazman, *Transport in a one-dimensional Luttinger liquid*, *Mesoscopic Electron Transport*, Springer (1997), 331–373.

[50] A. Komnik and R. Egger, *Nonequilibrium transport for crossed Luttinger liquids*, Physical Review Letters **80**, 2881 (1998).

[51] H. W. C. Postma, M. de Jonge, Z. Yao, and C. Dekker, *Electrical transport through carbon nanotube junctions created by mechanical manipulation*, Physical Review B **62**, R10653 (2000).

[52] M. Fuhrer, J. Nygård, L. Shih, M. Forero, Y.-G. Yoon, H. J. Choi, J. Ihm, S. G. Louie, A. Zettl, P. L. McEuen *et al.*, *Crossed nanotube junctions*, Science **288**, 494–497 (2000).

[53] N. Mott, *Conduction in glasses containing transition metal ions*, Journal of Non-Crystalline Solids **1**, 1–17 (1968).

[54] V. Ambegaokar, B. Halperin, and J. Langer, *Hopping conductivity in disordered systems*, Physical review B **4**, 2612 (1971).

[55] A. Skall and B. Shklovsky, *Mott equation for low temperature edge conductivity*, Soviet Physics-Solid State **16**, 1190 (1974).

[56] B. I. Shklovskii and A. L. Efros, *Electronic properties of doped semiconductors*, Springer (1984).

[57] A. Efros and B. Shklovskii, *Coulomb gap and low temperature conductivity of disordered systems*, Journal of Physics C: Solid State Physics **8**, L49 (1975).

[58] A. Frydman and Z. Ovadyahu, *Spin and quantum interference effects in hopping conductivity*, Solid State Communications **94**, 745–749 (1995).

[59] A. Kurobe and H. Kamimura, *Correlation effects on variable range hopping conduction and the magnetoresistance*, Journal of the Physical Society of Japan **51**, 1904–1913 (1982).

[60] 福山秀敏（編） メゾスコピック系の物理, 物性物理の新展開, 丸善株式会社 (1996).

[61] 高山 一長岡 洋介, 局在・量子ホール効果・密度波, 現代物理学叢書, 岩波書店 (2000).

[62] S. Hikami, A. I. Larkin, and Y. Nagaoka, *Spin-orbit interaction and magnetoresistance in the two dimensional random system*, Progress of Theoretical Physics **63**, 707–710 (1980).

[63] A. Kawabata, *Theory of negative magnetoresistance in three-dimensional systems*, Solid State Communications **34**, 431–432 (1980).

[64] A. Kawabata, *Theory of negative magnetoresistance I. Application to heavily doped semiconductors*, Journal of the Physical Society of Japan **49**, 628–637 (1980).

[65] D. V. Baxter, R. Richter, M. Trudeau, R. Cochrane, and J. Strom-Olsen, *Fitting to magnetoresistance under weak localization in three dimensions*, Journal de Physique **50**, 1673–1688 (1989).

[66] D. Wang, P. Song, C. Liu, W. Wu, and S. Fan, *Highly oriented carbon nanotube papers made of aligned carbon nanotubes*, Nanotechnology **19**, 075609 (2008).

[67] R. L. Whitby, T. Fukuda, T. Maekawa, S. L. James, and S. V. Mikhalovsky, *Geometric control and tuneable pore size distribution of buckypaper and buckydiscs*, Carbon **46**, 949–956 (2008).

[68] D. J. Bae, K. S. Kim, Y. S. Park, E. K. Suh, K. H. An, J.-M. Moon, S. C. Lim, S. H. Park, Y. H. Jeong, and Y. H. Lee, *Transport phenomena in an anisotropically aligned single-wall carbon nanotube film*, Physical Review B **64**, 233401 (2001).

[69] K. Yanagi, H. Udoguchi, S. Sagitani, Y. Oshima, T. Takenobu, H. Kataura, T. Ishida, K. Matsuda, and Y. Maniwa, *Transport mechanisms in metallic and semiconducting single-wall carbon nanotube networks*, ACS Nano **4**, 4027–4032 (2010).

[70] T. Fujimori, A. Morelos-Gómez, Z. Zhu, H. Muramatsu, R. Futamura, K. Urita, M. Terrones, T. Hayashi, M. Endo, S. Young Hong *et al.*, *Conducting linear chains of sulphur inside carbon nanotubes*, Nature Communications **4**, 2162 (2013).

[71] A. Jorio, M. Pimenta, A. Souza Filho, R. Saito, G. Dresselhaus, and M. Dresselhaus, *Characterizing carbon nanotube samples with resonance Raman scattering*, New Journal of Physics **5**, 139 (2003).

[72] S. Bandow, A. M. Rao, G. Sumanasekera, P. Eklund, F. Kokai, K. Takahashi, M. Yudasaka, and S. Iijima, *Evidence for anomalously small charge transfer in doped single-wall carbon nanohorn aggregates with Li, K and Br*, Applied Physics A **71**, 561–564 (2000).

[73] P. Eklund and K. Subbaswamy, *Analysis of Breit-Wigner line shapes in the Raman spectra of graphite intercalation compounds*, Physical Review B **20**, 5157 (1979).

[74] H. Luo, S. Desgreniers, Y. K. Vohra, and A. L. Ruoff, *High-pressure optical studies on sulfur to 121 GPa: Optical evidence for metallization*, Physical Review Letters **67**, 2998 (1991).

[75] H. Luo, R. G. Greene, and A. L. Ruoff,
beta-Po phase of sulfur at 162 GPa: X-ray diffraction study to 212 GPa, Physical Review Letters **71**, 2943 (1993).

[76] Y. Akahama, M. Kobayashi, and H. Kawamura, *Pressure-induced structural phase transition in sulfur at 83 GPa*, Physical Review B **48**, 6862 (1993).

[77] V. V. Struzhkin, R. J. Hemley, H.-k. Mao, and Y. A. Timofeev, *Superconductivity at 10–17 K in compressed sulphur*, Nature **390**, 382–384 (1997).

[78] M. Kociak, A. Y. Kasumov, S. Guéron, B. Reulet, I. Khodos, Y. B. Gorbatov, V. Volkov, L. Vaccarini, and H. Bouchiat, *Superconductivity in ropes of single-walled carbon nanotubes*, Physical Review Letters **86**, 2416 (2001).

[79] M. Ferrier, A. Kasumov, R. Deblock, S. Guéron, and H. Bouchiat, *Induced and intrinsic superconductivity in carbon nanotubes*, Journal of Physics D: Applied Physics **43**, 374003 (2010).

[80] W. Shi, Z. Wang, Q. Zhang, Y. Zheng, C. Ieong, M. He, R. Lortz, Y. Cai, N. Wang, T. Zhang *et al.*, *Superconductivity in bundles of double-wall carbon nanotubes*, Scientific Reports **2**, 625 (2012).

[81] Metallic carbon nanotube BlueMetal, Meijo Nano Carbon Co., Ltd.

[82] EPO-TEK H74, Epoxy Technology Inc.

[83] MILA 5000, ULVAC Technologies, Inc.

[84] JSM-7000F, JEOL Ltd.

[85] EPO-TEK H20E, Epoxy Technology Inc.

[86] ARZERITE VL-10, TAMURA CORPORATION ELECTRONIC CHEMICALS.

[87] PPMS, Quantum Design, Inc.

[88] Apiezon N Grease, Apiezon Products Ltd.

[89] DEPAINT KX, SAN-EI KAGAKU CO.,LTD.

[90] SR830, Stanford Research Systems.

[91] USF340, Caddock Electronics, Inc.

[92] DR200, Oxford Instruments plc.

[93] 370S, Lake Shore Cryotronics, Inc.

[94] MPMS-5S, Quantum Design, Inc.

[95] F. Morales, M. Monteverde, and M. Núñez Regueiro, *Pressure variation of Luttinger liquid parameters in single wall carbon nanotubes networks*, The European Physical Journal B-Condensed Matter and Complex Systems **65**, 511–514 (2008).

[96] G. Kim, E. Choi, D. Kim, D. Suh, Y. Park, K. Liu, G. Duesberg, and S. Roth, *Magnetoresistance of an entangled single-wall carbon-nanotube network*, Physical Review B **58**, 16064 (1998).

[97] Y. Nakai, R. Tsukada, Y. Miyata, T. Saito, K. Hata, and Y. Maniwa, *Observation of the intrinsic magnetic susceptibility of highly purified single-wall carbon nanotubes*, Physical Review B **92**, 041402 (2015).

[98] A. Ramirez, R. Haddon, O. Zhou, R. Fleming, J. Zhang, S. McClure, and R. Smalley, *Magnetic susceptibility of molecular carbon: nanotubes and fullerite*, Science **265**, 84–86 (1994).

[99] Y. Kim, O. N. Torrens, J. Kikkawa, E. Abou-Hamad, C. Goze-Bac, and D. E. Luzzi, *High-purity diamagnetic single-wall carbon nanotube buckypaper*, Chemistry of Materials **19**, 2982–2986 (2007).

[100] C. Wu, J. Li, G. Dong, and L. Guan, *Removal of ferromagnetic metals for the large-scale purification of single-walled carbon nanotubes*, The Journal of Physical Chemistry C **113**, 3612–3616 (2009).

[101] F. Schedin, A. Geim, S. Morozov, E. Hill, P. Blake, M. Katsnelson, and K. Novoselov, *Detection of individual gas molecules adsorbed on graphene*, Nature Materials **6**, 652–655 (2007).

[102] J. Sun, M. Muruganathan, and H. Mizuta, *Room temperature detection of individual molecular physisorption using suspended bilayer graphene*, Science Advances **2**, e1501518 (2016).

[103] S. J. Sque, R. Jones, and P. R. Briddon, *The transfer doping of graphite and graphene*, Physica Status Solidi Applied Research **204**, 3078–3084 (2007).

[104] C. Chen, S. Hung, M. Yang, C. Yeh, C. Wu, G. Chi, F. Ren, and S. Pearton, *Oxygen sensors made by monolayer graphene under room temperature*, Applied Physics Letters **99**, 243502–243502 (2011).

[105] Y. Yang and R. Murali, *Binding mechanisms of molecular oxygen and moisture to graphene*, Applied Physics Letters **98**, 093116–093116 (2011).

[106] J. Ristein, *Surface transfer doping of diamond*, Journal of Physics D: Applied Physics **39**, R71 (2006).

[107] Y. Dan, Y. Lu, N. Kybert, Z. Luo, and A. Johnson, *Intrinsic response of graphene vapor sensors*, Nano Letters **9**, 1472–1475 (2009).

[108] H. Pinto, R. Jones, J. Goss, and P. Briddon, *Mechanisms of doping graphene*, Physica Status Solidi Applied Research **207**, 2131–2136 (2010).

[109] A. Kaverzin, S. Strawbridge, A. Price, F. Withers, A. Savchenko, and D. Horsell, *Electrochemical doping of graphene with toluene*, Carbon **49**, 3829–3834 (2011).

[110] Y. Sato, K. Takai, and T. Enoki, *Electrically Controlled Adsorption of Oxygen in Bilayer Graphene Devices*, Nano Letters **11**, 3468–3475 (2011).

[111] R. Jaaniso, T. Kahro, J. Kozlova, J. Aarik, L. Aarik, H. Alles, A. Floren, A. Gerst, A. Kasikov, A. Niilisk *et al.*, *Temperature induced inversion of oxygen response in CVD graphene on SiO 2*, Sensors and Actuators B: Chemical **190**, 1006–1013 (2014).

[112] M. Toney and S. Fain Jr, *Low-energy electron diffraction study of molecular oxygen physisorbed on graphite*, Physical Review B **36**, 1248 (1987).

[113] Y. Jiang, Y. Zhang, J. Cao, R. Wu, and W. Ho, *Real-Space Imaging of Kondo Screening in a Two-Dimensional O2 Lattice*, Science **333**, 324–328 (2011).

[114] AP70 PV KISH GRAPHITE TYPE B, Covalent Materials Corporation.

[115] SC-100, Musashino Denshi, Inc.

[116] USK-2R, AS ONE Corporation.

[117] AWC-3, Asahi Rika Seisakusho K.K.

[118] VD-8, Nitto Denko Corporation.

[119] K. Kawabata, 超伝導超薄膜の輸送特性測定, Master's thesis, Department of Physics, Graduate School of Science, The University of Tokyo (2009).

[120] VH-Z450, KEYENCE CORPORATION.

[121] H. E. Romero, N. Shen, P. Joshi, H. R. Gutierrez, S. A. Tadigadapa, J. O. Sofo, and P. C. Eklund, *n-type behavior of graphene supported on Si/SiO2 substrates*, ACS Nano **2**, 2037–2044 (2008).

[122] J. Moser, A. Barreiro, and A. Bachtold, *Current-induced cleaning of graphene*, Applied Physics Letters **91**, 163513–163513 (2007).

[123] Z. Ni, H. Wang, Z. Luo, Y. Wang, T. Yu, Y. Wu, and Z. Shen, *The effect of vacuum annealing on graphene*, Journal of Raman Spectroscopy **41**, 479–483 (2009).

[124] Z. Cheng, Q. Zhou, C. Wang, Q. Li, C. Wang, and Y. Fang, *Toward intrinsic graphene surfaces: a systematic study on thermal annealing and wet-chemical treatment of SiO2-supported graphene devices*, Nano Letters **11**, 767–771 (2011).

[125] R. Nair, P. Blake, A. Grigorenko, K. Novoselov, T. Booth, T. Stauber, N. Peres, and A. Geim, *Fine structure constant defines visual transparency of graphene*, Science **320**, 1308–1308 (2008).

[126] P. Blake, E. Hill, A. Neto, K. Novoselov, D. Jiang, R. Yang, T. Booth, and A. Geim, *Making graphene visible*, Applied Physics Letters **91**, 063124 (2007).

[127] Z. Ni, H. Wang, J. Kasim, H. Fan, T. Yu, Y. Wu, Y. Feng, and Z. Shen, *Graphene thickness determination using reflection and contrast spectroscopy*, Nano Letters **7**, 2758–2763 (2007).

[128] H. Kojima, Graphene 試料の作成とその物性評価, Master's thesis, Department of Physics, Graduate School of Science, The University of Tokyo (2008).

[129] RAMAN-11, Nanophoton Corporation.

[130] D. Graf, F. Molitor, K. Ensslin, C. Stampfer, A. Jungen, C. Hierold, and L. Wirtz, *Spatially resolved Raman spectroscopy of single-and few-layer graphene*, Nano Letters **7**, 238–242 (2007).

[131] A. Nakayama, S. Hoshino, Y. Yamada, A. Ohmura, and F. Ishikawa, *Counting graphene layers based on the light-shielding effect of Raman scattering from a substrate*, Applied Physics Letters **107**, 231604 (2015).

[132] A. Ferrari and J. Robertson, *Interpretation of Raman spectra of disordered and amorphous carbon*, Physical Review B **61**, 14095 (2000).

[133] A. Das, S. Pisana, B. Chakraborty, S. Piscanec, S. Saha, U. Waghmare, K. Novoselov, H. Krishnamurthy, A. Geim, A. Ferrari *et al.*, *Monitoring dopants by Raman scattering in an electrochemically top-gated graphene transistor*, Nature Nanotechnology **3**, 210–215 (2008).

[134] S. Berciaud, S. Ryu, L. E. Brus, and T. F. Heinz, *Probing the intrinsic properties of exfoliated graphene: Raman spectroscopy of free-standing monolayers*, Nano Letters **9**, 346–352 (2008).

[135] c. O. Girit, J. C. Meyer, R. Erni, M. D. Rossell, C. Kisielowski, L. Yang, C.-H. Park, M. Crommie, M. L. Cohen, S. G. Louie, and A. Zettl, *Graphene at the Edge: Stability and Dynamics*, Science **323**, 1705 (2009).

[136] Ç. Ö. Girit and A. Zettl, *Soldering to a single atomic layer*, Applied Physics Letters **91**, 193512 (2007).

[137] J. Kim, H. Schoeller, J. Cho, and S. Park, *Effect of Oxidation on Indium Solderability*, Journal of Electronic Materials **37**, 483–489 (2008).

[138] B. Predel, *In-N (Indium-Nitrogen)*, SpringerMaterials - The Landolt-BÃűrnstein Database.

[139] 99.99% indium wire from FURUYA METAL Co., Ltd. or The Nilaco Corporation.

[140] D-550, FUJIKURA KASEI CO., LTD.

[141] 特別実験I　最終レポート, unpublished (2012/2/11).

[142] 特別実験　レポート, unpublished (2012).

[143] TR-71Ui, T&D Corporation.

[144] PAA-35XEi, KELLER.

[145] 2400, Keithley Instruments Inc.

[146] S. Ryu, L. Liu, S. Berciaud, Y.-J. Yu, H. Liu, P. Kim, G. W. Flynn, and L. E. Brus, *Atmospheric oxygen binding and hole doping in deformed graphene on a SiO2 substrate*, Nano Letters **10**, 4944–4951 (2010).

[147] A. Allouche and Y. Ferro, *Dissociative adsorption of small molecules at vacancies on the graphite (0001) surface*, Carbon **44**, 3320–3327 (2006).

[148] F. Mehmood, R. Pachter, W. Lu, and J. J. Boeckl, *Adsorption and diffusion of oxygen on single-layer graphene with topological defects*, The Journal of Physical Chemistry C **117**, 10366–10374 (2013).

[149] A. Kolmakov, D. Klenov, Y. Lilach, S. Stemmer, and M. Moskovits, *Enhanced gas sensing by individual SnO2 nanowires and nanobelts functionalized with Pd catalyst particles*, Nano Letters **5**, 667–673 (2005).

[150] L. Liu, S. Ryu, M. Tomasik, E. Stolyarova, N. Jung, M. Hybertsen, M. Steigerwald, L. Brus, and G. Flynn, *Graphene oxidation: thickness-dependent etching and strong chemical doping*, Nano Letters **8**, 1965–1970 (2008).

[151] J. Jones, C. Morris, G. Verbeck, and J. Perez, *Oxidative pit formation in pristine, hydrogenated and dehydrogenated graphene*, Applied Surface Science **264**, 853–863 (2013).

[152] C. Wong and R. T. Yang, *Cooperative effects in reactivity of carbon*, Carbon **20**, 253–254 (1982).

[153] F. Stevens, L. A. Kolodny, and T. P. Beebe, *Kinetics of graphite oxidation: monolayer and multilayer etch pits in HOPG studied by STM*, The Journal of Physical Chemistry B **102**, 10799–10804 (1998).

[154] H. Goto, E. Uesugi, R. Eguchi, A. Fujiwara, and Y. Kubozono, *Edge-dependent transport properties in graphene*, Nano Letters **13**, 1126–1130 (2013).

[155] U. Chandni, E. A. Henriksen, and J. Eisenstein, *Transport in indium-decorated graphene*, Physical Review B **91**, 245402 (2015).

[156] A. Fukuda, D. Terasawa, Y. Ohno, and K. Matsumoto, *Effect of the Inert Gas Adsorption on the Bilayer Graphene to the Localized Electron Magnetotransport*, Journal of Physics: Conference Series **568**, 52009–52015 (2014).

[157] D. Terasawa, A. Fukuda, A. Fujimoto, Y. Ohno, and K. Matsumoto, *Relationship between the resistance fluctuation and the weak localization effect in graphene*, The Physical Society of Japan 70th annual meeting (2015).

[158] H. B. Heersche, P. Jarillo-Herrero, J. B. Oostinga, L. M. Vandersypen, and A. F. Morpurgo, *Induced superconductivity in graphene*, Solid State Communications **143**, 72–76 (2007).

[159] G. Semenoff, *Condensed-matter simulation of a three-dimensional anomaly*, Physical Review Letters **53**, 2449–2452 (1984).

[160] J. Oostinga, H. Heersche, X. Liu, A. Morpurgo, and L. Vandersypen, *Gate-induced insulating state in bilayer graphene devices*, Nature Materials **7**, 151–157 (2007).

[161] B. Trauzettel, D. Bulaev, D. Loss, and G. Burkard, *Spin qubits in graphene quantum dots*, Nature Physics **3**, 192–196 (2007).

[162] K. Nakada, M. Fujita, G. Dresselhaus, and M. Dresselhaus, *Edge state in graphene ribbons: Nanometer size effect and edge shape dependence*, Physical Review B **54**, 17954 (1996).

[163] L. Brey and H. Fertig, *Electronic states of graphene nanoribbons studied with the Dirac equation*, Physical Review B **73**, 235411 (2006).

[164] S. Zhou, G. Gweon, A. Fedorov, P. First, W. De Heer, D. Lee, F. Guinea, A. Neto, and A. Lanzara, *Substrate-induced bandgap opening in epitaxial graphene*, Nature Materials **6**, 770–775 (2007).

[165] K. Novoselov, *Graphene: Mind the gap*, Nature Materials **6**, 720–721 (2007).

[166] E. McCann, *Asymmetry gap in the electronic band structure of bilayer graphene*, Physical Review B **74**, 161403 (2006).

[167] A. Bostwick, T. Ohta, J. McChesney, K. Emtsev, T. Seyller, K. Horn, and E. Rotenberg, *Symmetry breaking in few layer graphene films*, New Journal of Physics **9**, 385 (2007).

[168] E. McCann, Vladimir IFal ' ko, *Landau-level degeneracy and quantum Hall effect in a graphite bilayer*, Physical Review Letters **96**, 086805 (2006).

[169] M. Farjam and H. Rafii-Tabar, *Energy gap opening in submonolayer lithium on graphene: Local density functional and tight-binding calculations*, Physical Review B **79**, 045417 (2009).

[170] N. Mori, C. Bäuerle, T. Kumakura, M. Morishita, and H. Fukuyama, *STM Observations of Helium Atoms Adsorbed on Graphite Surfaces*, Journal of Low Temperature Physics **110**, 641–646 (1998).

[171] T. Matsui, H. Kambara, and H. Fukuyama, *STM observations of 2D Kr and Xe adsorbed on graphite*, Journal of Low Temperature Physics **126**, 373–378 (2002).

[172] N. Kitamura, A. Oshiyama, and O. Sugino, *Atomic and electronic structures of deformed graphite sheets*, Journal of the Physical Society of Japan **67**, 3976–3984 (1998).

[173] K. Gomes, W. Mar, W. Ko, F. Guinea, and H. Manoharan, *Designer Dirac fermions and topological phases in molecular graphene*, Nature **483**, 306–310 (2012).

[174] J. Sabio, C. Seoanez, S. Fratini, F. Guinea, A. C. Neto, and F. Sols, *Electrostatic interactions between graphene layers and their environment*, Physical Review B **77**, 195409 (2008).

[175] W. Zhang, C. Lin, K. Liu, T. Tite, C. Su, C. Chang, Y. Lee, C. Chu, K. Wei, J. Kuo *et al.*, *Opening an Electrical Band Gap of Bilayer Graphene with Molecular Doping*, ACS Nano **5**, 7517–7524 (2011).

[176] I. Langmuir, *THE CONSTITUTION AND FUNDAMENTAL PROPERTIES OF SOLIDS AND LIQUIDS. PART I. SOLIDS.*, Journal of the American Chemical Society **38**, 2221–2295 (1916).

[177] O. Sinanoğlu and K. Pitzer, *Interactions between molecules adsorbed on a surface*, The Journal of Chemical Physics **32**, 1279 (1960).

[178] A. Thomy, X. Duval, and J. Regnier, *Two-dimensional phase transitions as displayed by adsorption isotherms on graphite and other lamellar solids*, Surface Science Reports **1**, 1–38 (1981).

[179] B. Choi, H. Nham, and H. Youn, *Phase Diagram of a Physisorbed Krypton Monolayer on Graphite Using an Ellipsometric Technique*, Journal of the Korean Physical Society **53**, 3262–3266 (2008).

[180] D. Butler, J. Litzinger, and G. Stewart, *Completion of the Phase Diagram for the Monolayer Regime of the Krypton-Graphite Adsorption System*, Physical Review Letters **44**, 466–468 (1980).

[181] Y. Matsumoto, グラファイト上に吸着した 2 次元固体ヘリウム 3 の核磁性の研究, Master's thesis, Department of Physics, Graduate School of Science, The University of Tokyo (2001).

[182] A. Ambrosetti and P. Silvestrelli, *Adsorption of Rare-Gas Atoms and Water on Graphite and Graphene by van der Waals-Corrected Density Functional Theory*, The Journal of Physical Chemistry C **115**, 3695–3702 (2011).

[183] L. Bruch, R. Diehl, and J. Venables, *Progress in the measurement and modeling of physisorbed layers*, Reviews of Modern Physics **79**, 1381 (2007).

[184] M. Bartolomei, E. Carmona-Novillo, M. I. Hernández, J. Campos-Martínez, and F. Pirani, *Global Potentials for the Interaction Between Rare Gases and Graphene-based Surfaces: An Atom-bond Pairwise Additive Representation*, The Journal of Physical Chemistry C (2013).

[185] VLSI Design and Education Center, University of Tokyo. Collaborated with associate professor Yoshio Mita, and actual process was done by research associate Eric Lebrasser.

[186] J. Henrie, S. Kellis, S. Schultz, and A. Hawkins, *Electronic color charts for dielectric films on silicon*, Optics Express **12**, 1464–1469 (2004).

[187] K. Bolotin, K. Sikes, Z. Jiang, M. Klima, G. Fudenberg, J. Hone, P. Kim, and H. Stormer, *Ultrahigh electron mobility in suspended graphene*, Solid State Communications **146**, 351–355 (2008).

[188] S. Ravi, A. B. Kaiser, and C. W. Bumby, *Improved conduction in transparent single walled carbon nanotube networks drop-cast from volatile amine dispersions*, Chemical Physics Letters **496**, 80–85 (2010).

[189] K. Fujisawa, K. Komiyama, H. Muramatsu, D. Shimamoto, T. Tojo, Y. A. Kim, T. Hayashi, M. Endo, K. Oshida, M. Terrones *et al.*, *Chirality-dependent transport in double-walled carbon nanotube assemblies: The role of inner tubes*, ACS Nano **5**, 7547–7554 (2011).

[190] S. Luo, T. Liu, S. M. Benjamin, and J. S. Brooks, *Variable Range Hopping in Single-Wall Carbon Nanotube Thin Films: A Processing–Structure–Property Relationship Study*, Langmuir **29**, 8694–8702 (2013).

[191] S. Ravi, A. B. Kaiser, and C. W. Bumby, *Charge transport in surfactant-free single walled carbon nanotube networks*, Physica Status Solidi B Basic Research **250**, 1463–1467 (2013).

[192] The simulation for PPMS was perforemed by Dr. Ryo Toda.

[193] MPMS Application Note 1014-213 Subtracting the Sample Holder Background from Dilute Samples, Quantum Design, Inc.

[194] MS-A100, MIKASA CO., LTD.